IDENTIFYING RR LYRAE STARS IN THE DARK ENERGY SURVEY

A Dissertation

by

KATELYN MEREDITH STRINGER

Submitted to the Office of Graduate and Professional Studies of
Texas A&M University
in partial fulfillment of the requirements for the degree of

DOCTOR OF PHILOSOPHY

Chair of Committee,	Lucas Macri
Committee Members,	Jianhua Huang
	Jennifer Marshall
	Louis Strigari
Head of Department,	Grigory Rogachev

May 2020

Major Subject: Astronomy

ABSTRACT

RR Lyrae are evolved variable stars which act as powerful stellar tracers of Galactic halo structure and satellite galaxies. The Dark Energy Survey (DES), with its deep and wide coverage ($g \sim 24.3$ mag in a single exposure; over 5000 deg^2) provides a rich opportunity to search for substructures out to the edge of the Milky Way halo. However, the sparse and unevenly sampled multiband light curves from the DES wide-field survey pose a challenge for traditional techniques used to detect RRL. We present an empirically motivated and computationally efficient template fitting method to identify these variable stars in sparsely sampled multiband data. We apply this technique to light curves from two DES data releases and identify thousands of RRL. We then search the RRL catalog for groups of spatially nearby RRL in our catalog and recover multiple previously-identified stellar overdensities, demonstrating the efficacy of this method to trace Galactic substructures. We make the resultant RRL catalogs and the template fitting methods available for use in other sparse multiband data sets.

DEDICATION

Thank you, Lucas, for training me, for challenging me to do my best work, and for encouraging me to keep going, even when the finish line seemed out of reach. I have learned so much from you and I will always be grateful for it.

To Jen, thank you for giving me a chance in your REU program almost six years ago. You've opened so many doors for me and I can never say thank you enough. James Long, thank you for making all of this analysis possible. Working with you was a delight. Louie, thank you for all of your pep talks, your helpful input on my work, and for making meetings fun with your jokes. Jianhua, thank you for always encouraging me and helping me get the most out of the statistics program here. I always walk away feeling excited about my research and confident as a scientist after talking to you.

Alex Drlica-Wagner, thank you for sponsoring me to come to Fermilab and for helping me finish this PhD. I am a much better scientist because of you.

To my brother Chris, thank you for being the best friend anyone could ever have. To Mom, thank you for always being there for me when I really needed it, for always encouraging me, and for conquering Toontown with me. To Dad, thank you for sharing the joys of science with me and for never doubting I could do it, even when I didn't believe it myself. To my grandparents, thank you for always making me feel loved. Papa, thank you for never letting me forget that there's a tree in my future. Granddaddy, I wish I could show you all that I've learned about the Universe. I will never stop missing you. To Aunt Karen, thank you for all the unexpected care packages and cheery messages– they really helped! For everyone in my family, I can never express enough gratitude for how much all of you have supported me throughout these years. I am here today because of you.

To Hossein Zahed, thank you for taking a chance on me and helping see my own strengths as a data scientist. The confidence I gained while working on your team has made all the difference.

To the Klumpes, thank you for always believing in me, celebrating with me, and for treating me like family. I would never have made it to grad school if not for you.

To my fellow grads and postdoc friends: Mike, Jimmy, Ting, Brett, Steven, Ben, Wenlong, Yi, Nancy, Andrew Quick, Alanna, Leo, Peter Chi, Vince, Emily, Jonathan Perry, Sarah, Taylor, Peter Ferguson, Andrew Pace, YuanYuan, Nora, Rob, Peter Brown, Zhenfeng, Jonathan Cohn, Sijie, Tarini, Jiawen, Alex, Jacqueline, Ryan Quadri, Claire, Yaswant, Matt, Addy, Silvana, Gesa, and Mica, thank you for encouraging me, for laughing with me, for cheering me up when the going got tough. Ryan Oelkers, thank you for showing me the research ropes so many years ago. Your pep talks and sarcastic jokes keep me smiling. To my friends back home: Julia, Austin, Caitlin, Alexander, Bradley, and Bob Nuu, thank you for your enduring friendship and for reminding me there's life outside of school.

Thank you Anakin for always greeting me at the door when I come home. My life is better in every way with you around.

To Dan, thank you for filling my time here with such joy. I can't wait to see what's next.

For all those who have supported me who I did not specifically mention, thank you for everything!

CONTRIBUTORS AND FUNDING SOURCES

Contributors

This work was supported by a dissertation committee consisting of advisor Professor Lucas Macri and Professors Jennifer Marshall and Louis Strigari of the Department of Physics and Astronomy and Professor Jianhua Huang of the Department of Statistics.

The data used in Sections 3 and 4 was processed by the Dark Energy Survey Collaboration. The template presented in Section 2 was developed by Professor James P. Long at Texas A&M, who now conducts research at the M.D. Anderson Cancer Center. A combination of Sections 2 & 3 was published in 2019 in the Astronomical Journal. This research has made use of the SIMBAD database, operated at CDS, Strasbourg, France.

All other work conducted for the thesis (or) dissertation was completed by the student independently.

Funding Sources

Graduate study was supported by a Diversity fellowship from Texas A&M University, funding from the Universities Research Association Visiting Scholar Program, and a research fellowship from the George P. and Cynthia Woods Mitchell Institute for Physics and Astronomy.

Funding for the DES Projects has been provided by the U.S. Department of Energy, the U.S. National Science Foundation, the Ministry of Science and Education of Spain, the Science and Technology Facilities Council of the United Kingdom, the Higher Education Funding Council for England, the National Center for Supercomputing Applications at the University of Illinois at Urbana-Champaign, the Kavli Institute of Cosmological Physics at the University of Chicago, the Center for Cosmology and Astro-Particle Physics at the Ohio State University, the Mitchell Institute for Fundamental Physics and Astronomy at Texas A&M University, Financiadora de Estudos e Projetos, Fundação Carlos Chagas Filho de Amparo à Pesquisa do Estado do Rio de Janeiro, Conselho Nacional de Desenvolvimento Científico e Tecnológico and the Ministério da Ciência,

Tecnologia e Inovação, the Deutsche Forschungsgemeinschaft and the Collaborating Institutions in the Dark Energy Survey.

The Collaborating Institutions are Argonne National Laboratory, the University of California at Santa Cruz, the University of Cambridge, Centro de Investigaciones Energéticas, Medioambientales y Tecnológicas-Madrid, the University of Chicago, University College London, the DES-Brazil Consortium, the University of Edinburgh, the Eidgenössische Technische Hochschule (ETH) Zürich, Fermi National Accelerator Laboratory, the University of Illinois at Urbana-Champaign, the Institut de Ciències de l'Espai (IEEC/CSIC), the Institut de Física d'Altes Energies, Lawrence Berkeley National Laboratory, the Ludwig-Maximilians Universität München and the associated Excellence Cluster Universe, the University of Michigan, the National Optical Astronomy Observatory, the University of Nottingham, The Ohio State University, the University of Pennsylvania, the University of Portsmouth, SLAC National Accelerator Laboratory, Stanford University, the University of Sussex, Texas A&M University, and the OzDES Membership Consortium.

Based in part on observations at Cerro Tololo Inter-American Observatory, National Optical Astronomy Observatory, which is operated by the Association of Universities for Research in Astronomy (AURA) under a cooperative agreement with the National Science Foundation.

The DES data management system is supported by the National Science Foundation under Grant Numbers AST-1138766 and AST-1536171. The DES participants from Spanish institutions are partially supported by MINECO under grants AYA2015-71825, ESP2015-66861, FPA2015-68048, SEV-2016-0588, SEV-2016-0597, and MDM-2015-0509, some of which include ERDF funds from the European Union. IFAE is partially funded by the CERCA program of the Generalitat de Catalunya. Research leading to these results has received funding from the European Research Council under the European Union's Seventh Framework Program (FP7/2007-2013) including ERC grant agreements 240672, 291329, and 306478. We acknowledge support from the Australian Research Council Centre of Excellence for All-sky Astrophysics (CAASTRO), through project number CE110001020, and the Brazilian Instituto Nacional de Ciência e Tecnologia (INCT) e-Universe (CNPq grant 465376/2014-2).

NOMENCLATURE

α	Right Ascension
A_g	light curve amplitude in the g band
AGB	Asymptotic Giant Branch
AGN	Active Galactic Nuclei
ATLAS	Asteroid Terrestrial-impact Last Alert System
CCD	charge-coupled device
CSDR2	Second data release from the Catalina Sky Surveys
δ	Declination
d	day
DECam	Dark Energy Camera mounted on the 4-m Blanco telescope at CTIO
DES	Dark Energy Survey
dSph	dwarf spheroidal galaxy
[Fe/H]	metallicity, or the Iron-to-Hydrogen ratio of a star. This value for the Sun is defined to be zero.
Gaia DR2	Second data release from the Global Astrometric Interferometer for Astrophysics telescope
HB	Horizontal Branch
IS	Instability Strip
kpc	kiloparsec
light curve	time-stamped observations for an astronomical object
LSST	Legacy Survey of Space and Time
mag	magnitude

M_b	absolute magnitude in a band b
μ	distance modulus
MSTO	Main Sequence Turnoff
P	period of an RRL pulsation cycle
Pan-STARRS	Panoramic Survey Telescope and Rapid Response System
pc	parsec
ϕ	phase of maximum light
photometry	measurement of a source's incoming flux
P-L	Period-Luminosity relation
P-L-Z	Period-Luminosity-Metallicity relation
QSO	Quasi-Stellar Object, also called a quasar
$r_{1/2}$	half-light radius
RF	Random Forest Classifier
RGB	Red Giant Branch
RMS	root-mean-square
RRL	RR Lyrae Stars, including all subtypes
RRab	RR Lyrae stars which pulsate in the fundamental mode
RRc	RR Lyrae stars which pulsate in the first overtone mode
RRd	RR Lyrae stars which simultaneously pulsate in both the fundamental and first overtone modes
s	second
S82	Stripe 82
sec	second
SDSS	Sloan Digital Sky Survey
S/N	Signal-to-noise ratio
ω	frequency, $1/P$

Y3	DES data release containing the first three years of observations
Y6	DES data release containing all six years of observations

TABLE OF CONTENTS

Page

LIST OF FIGURES

FIGURE Page

LIST OF TABLES

TABLE Page

1. INTRODUCTION*

1.1 RR Lyrae Stars

Over the past century, RR Lyrae variable stars (RRL) have become one of the most widely used stellar tracers in near-field cosmology, especially within the Milky Way. Thanks to the discovery of RR Lyrae itself (Pickering et al., 1901) and the subsequent studies of their pulsation (see King and Cox, 1968 and Catelan and Smith, 2015 for a review of the pioneering and current works in this field), these stars have well-understood period-luminosity-metallicity (*P-L-Z*) relations, making them excellent distance indicators (e.g., Cáceres and Catelan, 2008; Marconi et al., 2015). Their efficacy in tracing the old stellar populations in the Milky Way is directly related to their physical and evolutionary properties.

1.1.1 Evolution

RR Lyrae begin as subsolar mass stars which evolve off the Main Sequence and the Red Giant Branch onto the Horizontal Branch, where they intersect with the Instability Strip (IS) (e.g., Salaris and Cassisi, 2005; Marconi et al., 2015). Like other types of variable stars inhabiting the IS, these stars display periodic variations in magnitude due to radial (spherically symmetric) pulsations driven by the changing opacity of partially ionized layers of hydrogen and helium in their atmospheres, dubbed the "κ mechanism" by Baker and Kippenhahn (1962) (see King and Cox 1968 for an excellent overview of these atmospheric processes). As they evolve off the Zero-Age Horizontal Branch, RRL experience changes in their pulsation modes and periods (van Albada and Baker, 1973; Le Borgne et al., 2007; Kunder et al., 2011). Eventually, they will completely deplete their helium cores and evolve out of the IS onto the Asymptotic Giant Branch toward their eventual deaths. The evolutionary tracks that these stars follow, as well as the boundaries of the IS, are highly dependent on the star's luminosity, temperature, mass, metallicity, and helium content

*Part of this section is reprinted with permission from Identification of RR Lyrae stars in multiband, sparsely-sampled data from the Dark Energy Survey using template fitting and Random Forest classification by Stringer, et al. 2019. *The Astronomical Journal*, 158, 1. Copyright 2019 by The American Astronomical Society.

(Szabó et al., 2004). We show where RRL reside in an example color-magnitude diagram from the Sculptor dwarf spheroidal galaxy in Figure 1.1.

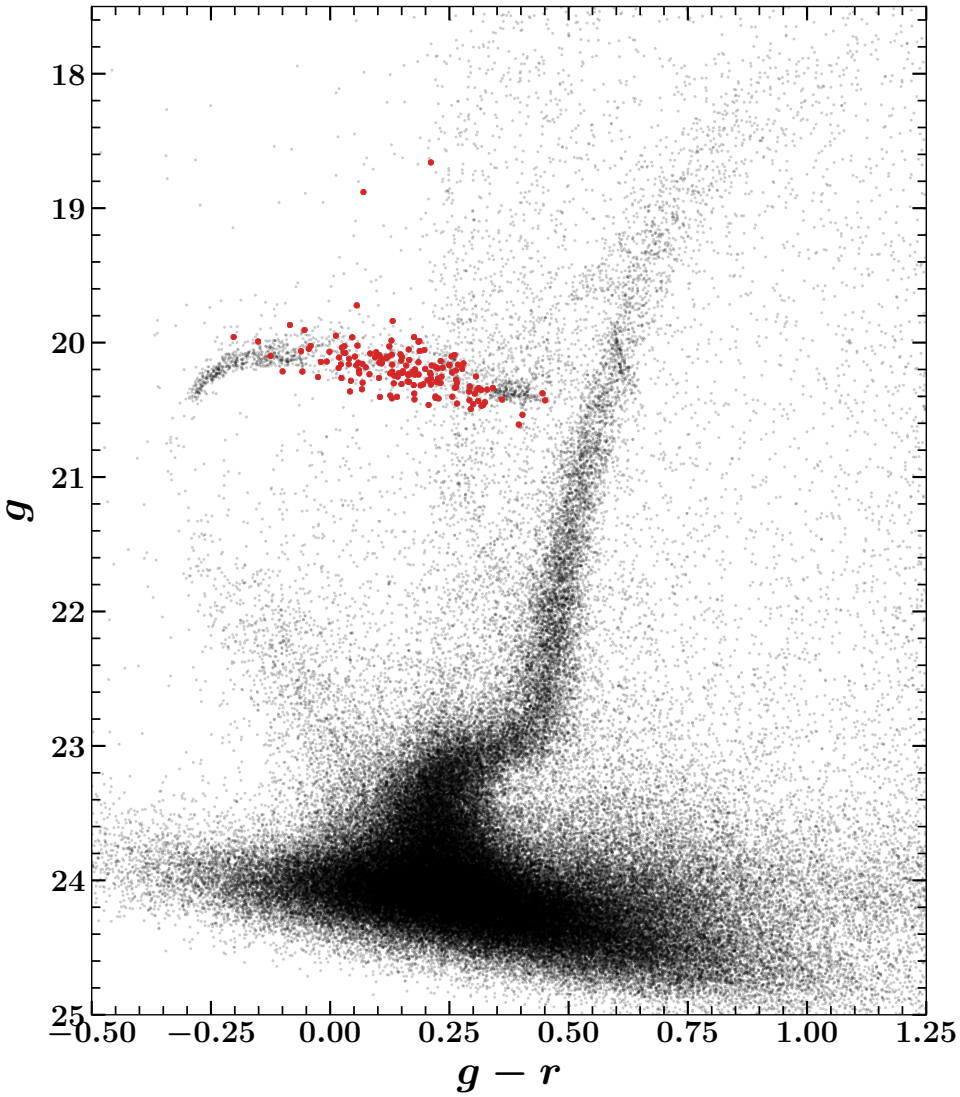

Figure 1.1: Color magnitude diagram of the stars in the Sculptor dwarf spheroidal galaxy in DES Y6 data. The locations of identified RRL are overplotted in red, while other stellar objects are plotted in black. As members of the horizontal branch, they have close to constant magnitude regardless of their color.

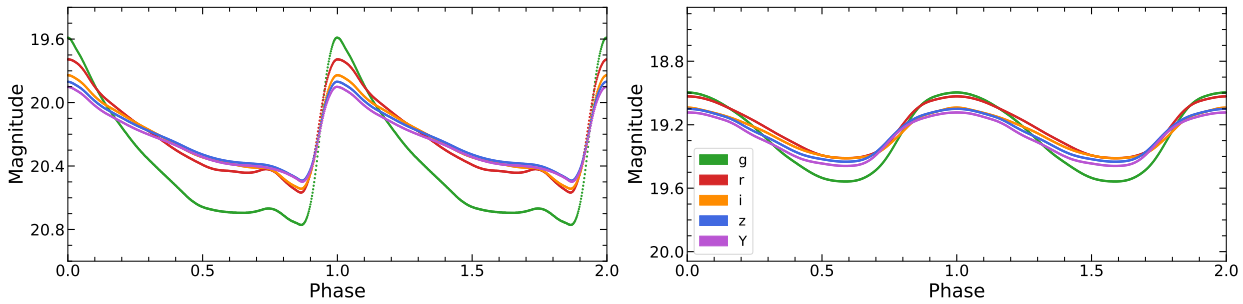

Figure 1.2: Example RRL light curve shapes derived by Sesar et al.(2010) for RRab (left) and RRc (right). Light curves have been shifted into the DES filter system. The vertical axes span the same range in magnitudes to demonstrate the smaller amplitude of the RRc.

1.1.2 Sub-types

The two most common sub-types of RRL are those pulsating in the fundamental mode, RRab, and those pulsating in the first overtone, RRc. When their light curves are adequately sampled, RRab are easily identified by their short periods ($0.4 \lesssim P \lesssim 1$ d), relatively large pulsation amplitudes ($0.5 \lesssim A_g \lesssim 1.5$ mag), and a characteristic sawtooth shape. RRc have shorter periods ($0.2 \lesssim P \lesssim 0.45$ d), smaller amplitudes ($0.2 \lesssim A_g \lesssim 0.8$ mag), more sinusoidal-shaped light curves, and are generally less numerous than RRab. Because of their more sinusoidal light curve shapes and smaller amplitudes, RRc are often difficult to distinguish from other types of variables, especially eclipsing binaries. Double-mode RRL (RRd), another sub-type of RRL which pulsate in both the fundamental and overtone modes simultaneously, also occur, but are not discussed in depth in this document. Example light curve shapes for both RRab and RRc are shown in Figure 1.2.

The fraction of RRab to RRc and the average periods of each are highly dependent on the metallicity and evolution of the stellar population in which they formed and is still not fully understood (see Catelan 2009; Lee et al. 2014; Fabrizio et al. 2019; Prudil et al. 2020 and references therein.) Most populations of RRL in the Milky Way are commonly subdivided into Oosterhoff I, II, and intermediate groups based on these observational properties (named after the first dichotomy applied to globular clusters by Oosterhoff 1939. We refer the interested reader to Table 6

in Martínez-Vázquez et al. (2017) for a summary of these properties for a selection of Local Group dwarf galaxies.

1.1.3 *P-L-Z* relation

Like their well-known Cepheid cousins, RRL follow a *P–L* relation, or a strong dependence between their luminosities and their pulsation periods. However, determining accurate RRL distances is hampered by a significant amount of scatter in this *P–L* relation, due in part to the differing boundaries of the IS for various progenitor masses and metallicities (Marconi et al., 2015). This scatter decreases significantly in the near-infrared bands where metallicity effects on temperature are less pronounced (see (Bono et al., 2016) for a review). However, for optical observations of RRL, an additional metallicity dependence must be introduced to the *P–L* relation to improve the precision of the distance estimates (see Figure 14 of Marconi et al. 2015 for a demonstration of the magnitude offsets introduced by a range of metallicity values). As metallicity strongly affects the effective temperature, and hence the color of a star, these *P-L-Z* relations are sometimes written as *P-L-C* relations (e.g., Cáceres and Catelan, 2008). RRc periods must be “fundamentalized" when calculating their distances with the *P-L-Z* relation (Catelan, 2009).

Currently, optical *P-L-Z* relations have been derived for RRL in the Johnson-Cousins (Catelan et al., 2004; Marconi et al., 2015), SDSS (Cáceres and Catelan, 2008), Pan-STARRS (Sesar et al., 2017), and Gaia filter systems (Muraveva et al., 2018). Such a relation is not yet available in the DES filter system, but is currently in development (Vivas, et al., in prep).

1.1.4 Usefulness as Tracers

In recent years, RRL have become one of the most widely used tracers of old stellar populations in Galactic science. Since RRL evolve from subsolar mass stars, the host stellar populations where they formed must be $\gtrsim 10$ Gyr old (Bono et al., 2011; Marconi, 2012). This property, along with their *P-L-Z* relation and relatively bright luminosities ($M_V \approx 0.59$ at $[\mathrm{Fe/H}] \approx -1.5$; Cacciari and Clementini, 2003), makes RRL well-suited to trace discrete stellar populations (satellite galaxies, star clusters, and streams) within the Milky Way halo (e.g., Catelan et al., 2004; Vivas et al., 2004;

Cáceres and Catelan, 2008; Sesar et al., 2010; Stetson et al., 2014; Fiorentino et al., 2015).

Locating these stellar populations is crucial for testing the leading ΛCDM hierarchical cosmological model, which predicts that the haloes of large galaxies like the Milky Way are formed through the accretion and disruption of lower mass haloes (Bullock and Johnston, 2005). Recent re-examinations of these simulations predict that the outer reaches of the stellar halo ($d \geq 100$ kpc) are primarily composed of the most recently accreted satellites and that thousands of RRL should be present in them (Sanderson et al., 2017). Once satellite galaxies and their disrupted remains are found, their distribution and properties can reveal valuable clues about the formation history, dark matter density profile, and mass of the Milky Way. While these objects are interesting in their own right, the statistical information about this sample is vital to place the Milky Way in a broader cosmological context.

Numerous Milky Way substructures have already been discovered. Eleven "classical" dwarf galaxies were known to orbit the Milky Way before 2005 (McConnachie, 2012)[1]. Thanks to the advent of wide-field surveys such as the Sloan Digital Sky Survey (SDSS, York et al., 2000), the Panoramic Survey Telescope and Rapid Response System (Pan-STARRS, Chambers et al., 2016), the Dark Energy Survey (DES, Dark Energy Survey Collaboration et al., 2016), and the Gaia mission (Gaia Collaboration et al., 2016), over 40 new dwarf satellite candidates have been discovered (Willman et al., 2005a,b; Zucker et al., 2006b,a; Belokurov et al., 2006b, 2007b, 2008, 2009, 2010; Grillmair, 2006, 2009; Sakamoto and Hasegawa, 2006; Irwin et al., 2007; Walsh et al., 2007; Kim et al., 2015; Bechtol et al., 2015; Koposov et al., 2015; Drlica-Wagner et al., 2015; Laevens et al., 2015b,a; Luque et al., 2016; Torrealba et al., 2016a; Luque et al., 2017; Torrealba et al., 2016b; Koposov et al., 2018; Torrealba et al., 2019). In addition to galaxies that are still intact, tidal streams, the disrupted remains of satellite galaxies and globular clusters, have been discovered to be prevalent within the Milky Way halo (e.g., Odenkirchen et al., 2001; Newberg et al., 2002; Belokurov et al., 2006a; Bernard et al., 2014; Koposov et al., 2014; Grillmair and Carlin, 2016; Bernard et al., 2016; Balbinot et al., 2016; Shipp et al., 2018; Mateu et al., 2018).

[1]The nature of the Canis Major Overdensity as a satellite galaxy is in doubt due to a lack of an RRL excess and a potential warp in the Milky Way disk (Mateu et al., 2009).

Besides these, additional large stellar overdensities populate the MW stellar halo with origins still unknown (e.g., Vivas et al., 2001; Newberg et al., 2002; Majewski et al., 2004; Rocha-Pinto et al., 2004; Sesar et al., 2007; Belokurov et al., 2007a; Sharma et al., 2010; Deason et al., 2014; Li et al., 2016; Pieres et al., 2017; Bergemann et al., 2018; Prudil et al., 2018; Belokurov et al., 2018a,b; Myeong et al., 2018).

Most of these satellites and streams were discovered as stellar overdensities in photometric catalogs (Willman, 2010, and references therein). However, this detection method is biased against diffuse objects with low surface brightness ($\mu_{V,0} \gtrsim 29\ \mathrm{mag/arcsec^2}$; Baker and Willman 2015), so an alternative method is needed to locate other faint structures that may have evaded detection. RRL are sufficiently rare so as to not randomly form in pairs outside of stellar structures, so searching for groups of spatially close RRL provides an independent method to detect new structures (Ivezić et al., 2004; Sesar et al., 2014; Baker and Willman, 2015; Medina et al., 2017, 2018). Indeed, at least one RRL has been found in all but three satellite galaxies with available time series data[2]. (Boettcher et al., 2013; Vivas et al., 2016; Martínez-Vázquez et al., 2017, 2019, and references therein). Thus, identifying RRL in the Galactic halo can increase the census of old, metal poor satellite galaxies, streams, and overdensities, and improve our understanding of the Milky Way.

1.1.5 Typical Identification Methods

RR Lyrae are typically identified through examination of their light curves, although certain properties of the stars (such as their metallicities) can only be determined with high precision through spectroscopy. To identify an RRL from its time series data, or its "unfolded" light curve, one needs to first estimate the period of its variation. At the beginning of the 20th century, these calculations were done by hand using visual magnitudes measured from photographic plates (e.g. Bailey, 1902). In later years, the increased availability of the modern electronic computer allowed for the implementation of more automated methods of period estimation (e.g. Lafler and Kinman,

[2]Kim 2, Willman I and Carina III have no detected RRL in their vicinities (Siegel et al., 2008; Torrealba et al., 2018; Martínez-Vázquez et al., 2019).

1965; Lomb, 1976; Scargle, 1982; Reimann, 1994). Overall, the most widespread methods used in RRL period estimation are variants of Fourier analysis and least-squares fitting (see VanderPlas 2018, and the sources within, for an overview of these methods). After the light curves have been "phase-folded" using their determined periods, the identification of the RRL and its subtype can be determined through visual inspection and from statistical properties of the light curve.

With the dramatic increases in the quantity of available data from large scale surveys in recent years, the need for automated detection algorithms has grown significantly. Stetson (1996) made great strides in this regard when he introduced an automated method to identify Cepheid variables using template light curves to estimate their periods and a scoring system based on calculated variability indices. Similar templates for RRL were created (Layden, 1998) and applied to single band light curves, leading to the identification of thousands of these variables (Vivas and Zinn, 2006; Sesar et al., 2010; Torrealba et al., 2015, etc.). A notable example is the work of Sesar et al. (2010), who used the well-sampled SDSS data in stripe 82 to identify 483 RRL and create ~ 20 template RRL light curve shapes in SDSS $griz$ and 12 in u. These single-band templates have proven to be very effective at recovering RRL periods when fit to well-sampled light curves in each filter separately.

Recent studies have extended this period-finding technique to multiple filters (Mateu et al., 2012; VanderPlas and Ivezić, 2015; Mondrik et al., 2015; Saha and Vivas, 2017). However, these algorithms suffer in performance when applied to extremely sparsely-sampled data. Hernitschek et al. (2016) and Sesar et al. (2017) developed separate techniques to identify RRL in the sparsely-sampled multiband Pan-STARRS data (Chambers et al., 2016) and found thousands of such variables. However, their methods of fitting a damped random walk model or an ensemble of templates can be very computationally expensive, imposing limits on their application to very large data sets like that of the Dark Energy Survey.

1.2 The Dark Energy Survey

The Dark Energy Survey (hereafter DES) is a five-year multiband (*grizY*) imaging survey using the Dark Energy Camera (Flaugher et al., 2015) on the 4-m Blanco Telescope at Cerro Tololo

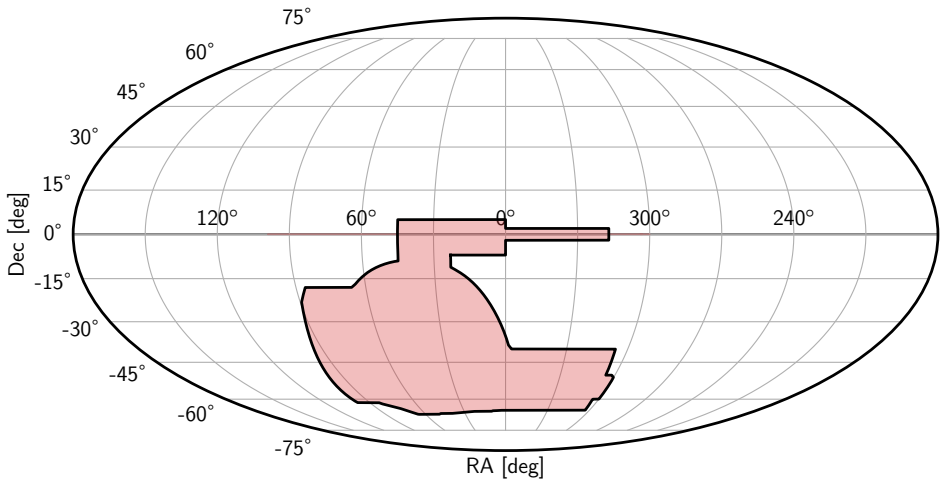

Figure 1.3: DES footprint projected in equatorial coordinates. The area covered by the 5000 deg^2 wide-field survey is shaded in red.

Inter-American Observatory (CTIO). DES is comprised of a main wide-field survey which spans ($\sim 5000\,\mathrm{deg}^2$) near the Southern Galactic cap (The Dark Energy Survey Collaboration, 2005; Diehl et al., 2016) and a smaller-scale supernova survey comprised of ten ~ 3 deg^2 fields (Diehl et al., 2014; Kessler et al., 2015). The area covered by the wide field survey is shown in Figure 1.3, which has been adapted from Figure 2 in Morganson et al. (2018). The main science goal of DES is to better understand the nature of dark energy, driving the accelerated expansion of the Universe, with complementary probes: weak gravitational lensing, galaxy clusters, and distances to type Ia supernovae (Abbott et al., 2018). The targeted survey has discovered hundreds of supernovae (e.g. Smith et al., 2020) while the six-year wide-field survey, with uniform depth ($g \sim 25$ mag) in the coadded images, enables high precision cosmology on large scales. As this work aims to discover RRL over a large area to complement other existing data sets, we focus solely on the DES wide-field survey in the rest of this document.

These specific science goals drove the observing strategy of the survey, which sought to image the entire wide-field footprint ten times in each of $grizY$. As DES images were collected, the filter to be used and the location to be imaged were prioritized according to the time of the year, the sky conditions (Moon phase, seeing, weather), and how many times that particular area had already

been imaged (Neilsen and Annis, 2014) (see Fig. 3 in Diehl et al., 2016). While this strategy ensured uniform depth and the best use of the observing time, objects in the wide-field survey are sampled with a highly unpredictable cadence.

With its depth, uniformity, and location in the Southern sky, the DES wide-field survey data set provides an excellent test bed for probing Milky Way substructure with RRL in a region previously untouched by other large scale surveys. However, the DES light curves from this data set are multiband and poorly sampled, causing problems for previously-developed light curve identification techniques. In this dissertation, we detail how we overcome these challenges by creating a empirically derived light curve template and a computationally efficient fitting algorithm to determine periods and other light curve parameters. We then present the results of our application of this method on the DES wide-field data sets from the first three years of observations and after the conclusion of the full survey.

2. TEMPLATE FITTING FOR IDENTIFICATION IN SPARSE MULTIBAND DATA SETS*

In this section, we introduce an empirically derived template and fitting method[1] to identify and characterize RRL light curves in sparsely sampled multiband data. Its construction and usage is summarized below. In this section, we use the words “model" and “template" interchangeably.

2.1 Template Derivation

As RRab are the most numerous subtype of RRL present in the Milky Way, we tailored this model towards their readily identifiable asymmetric light curves. We define the form for the RRab model as:

$$m_b(t) = \mu + M_b(\omega) + R_b E(B-V) + a\gamma_b(\omega t + \phi) \tag{2.1}$$

In this formalism we assume that there are population parameters common to all RRab:

$$\begin{aligned} M_b(\omega) &= \text{absolute magnitude in band } b \text{ for an RRL with frequency } \omega \\ R_b &= \text{total-to-selective extinction coefficient for band } b \\ \gamma_b &= \text{shape of the RRL light curve in band } b \end{aligned} \tag{2.2}$$

the derivation of which we discuss further in this section. We also define several object specific parameters, which are unique for each RRab:

$$\begin{aligned} \mu &= \text{distance modulus} \\ E(B-V) &= \text{reddening} \\ a &= \text{amplitude} \\ \omega &= \text{frequency } (1/P) \\ \phi &= \text{ phase of maximum light.} \end{aligned} \tag{2.3}$$

*Part of this section is reprinted with permission from Identification of RR Lyrae stars in multiband, sparsely-sampled data from the Dark Energy Survey using template fitting and Random Forest classification by Stringer, et al. 2019. *The Astronomical Journal*, 158, 1. Copyright 2019 by The American Astronomical Society.

[1]This model and fitting method was developed by Professor James P. Long of the M.D. Anderson Cancer Center.

For one RRab, the time-series photometry can be written as $\{\{t_{bi}, m_{bi}, \sigma_{bi}\}_{i=1}^{n_b}\}_{b=1}^{B}$ where m_{bi} is the observed magnitude at time t_{bi} in filter b measured with (known) uncertainty σ_{bi}. The bands are indexed $1, \ldots, B$ instead of typical letters (e.g., *ugriz*). The model and data are related by

$$m_{bi} = m_b(t_{bi}) + \epsilon_{bi}$$

where $\epsilon_{bi} \sim N(0, \sigma_{bi}^2)$, meaning the noise parameter ϵ_{bi} can be viewed as a random normal variable with mean=0 and $Var(\epsilon_{bi}) = \sigma_{bi}^2$.

This model assumes that all RRab light curves share a common shape in each band and that RRab are strictly singly periodic functions. While reasonable, these assumptions are an approximation. For example, our model does not account for the amplitude and phase modulations which vary according to an additional period caused by the Blažhko effect (Blažko, 1907), or long-term changes in the fundamental period as the star evolves (van Albada and Baker, 1973; Le Borgne et al., 2007; Kunder et al., 2011). Rather than construct a perfectly accurate model, the goal is to construct a model with few free parameters that provides a better approximation to RRab variation than existing methods. For example, a simple sinusoid model fit to 5 filters has a total of 16 free parameters (5 means, 5 amplitudes, 5 phases, and 1 frequency) while providing only a very rough approximation to the steep rise and slow decline in brightness observed in RRab light curves. In contrast, this model provides a significantly better approximation while fitting for just 5 free parameters (or 4 if light curves are corrected for extinction prior to fitting).

2.2 Determining Template Population Values

In this section, we discuss the derivation of the population parameters common to all RRab which we defined in Equation 2.2. We estimated these parameters $M_b(P)$, R_b, and γ_b using a combination of theory and existing data sets. To develop the *P–L* relation for the RRab template, we determined the values of $M_b(P)$ for *ugriz* using version 3.2 of the `BaSTI` synthetic horizontal branch generator[2], based on the evolutionary tracks of Pietrinferni et al. (2004, 2006). We gener-

[2]Available at `albione.oa-teramo.inaf.it/BASTI/WEB_TOOLS/HB_SYNT/`

Band b	$c_{\rm SDSS}$	$p_{1,\rm SDSS}$	$p_{2,\rm SDSS}$	$c_{\rm DES}$	$p_{1,\rm DES}$	$p_{2,\rm DES}$
u	1.889	-0.049	-0.319	—	—	—
g	0.767	0.167	-0.595	0.730	-0.020	-0.065
r	0.550	-0.637	-0.353	0.542	-0.739	0.997
i	0.505	-1.065	-0.202	0.522	-1.136	-0.057
z	0.510	-1.308	-0.231	0.520	-1.292	-0.535
Y	—	—	—	0.558	-1.392	0.657

Table 2.1: Template *P–L* coefficients.

ated synthetic absolute magnitudes for RRL spanning $-0.48 \leq \log P \leq 0.08$ with a metallicity of $[Fe/H] = -2.85$ to use as our starting values for $M_b(P)$. Then, we shifted the template curve in each filter to match the filter-dependent magnitude offsets shown in real SDSS and DES light curves. We parametrized these empirical $M_b(P)$ by using a quadratic period-absolute magnitude *P–L* relation at an unknown fixed metallicity. However, we determined empirically with the DES Y3 data that this value is $[\mathrm{Fe/H}] \approx -1.5$ (see §3.5.4 for an extended discussion of the template metallicity). The form of the RRab template's *P–L* relation is as follows:

$$M_b(P) = c_{0b} + p_{1b}(log_{10}(P) + 0.2) + p_{2b}(log_{10}(P) + 0.2)^2 \tag{2.4}$$

where the c, p_1 and p_2 values for the SDSS and DES filters are shown in Table 2.1. The final template *P–L* relations are shown in Figure 2.1.

The filter-dependent extinction coefficients R_b quantify the amount of incoming light attenuated by interstellar dust in a given filter. We computed these coefficients by adopting the Fitzpatrick (1999) extinction law with $R_V = 3.1$. The values for both SDSS and DES filters are summarized in Table 2.2. Note that these values are only used if the templates are fit with light curves uncorrected for extinction. In general, it is better to fit with dust-corrected light curves because the model has one fewer free parameter and the uncertainty on distance is greatly reduced.

γ_b, the light curve shape in filter b, is a function of phase that covers one pulsation period. We use RRab found by Sesar et al. (2010) to estimate γ_b for the SDSS filters. We assume the same

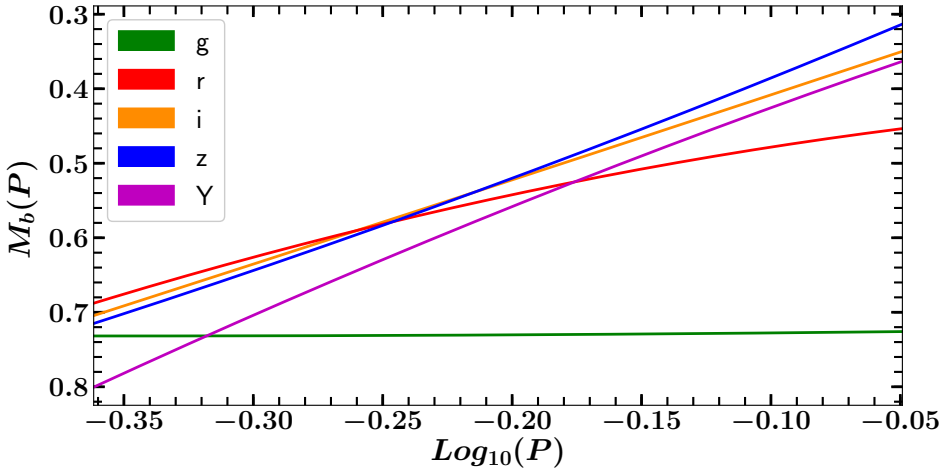

Figure 2.1: *P–L* relations used in our template fitting procedure. RRL have nearly constant absolute magnitudes in g regardless of period.

Band	SDSS R_b	DES R_b
u	4.799	—
g	3.737	3.665
r	2.587	2.464
i	1.922	1.804
z	1.430	1.380
Y	—	1.196

Table 2.2: Template extinction coefficients based on Fitzpatrick (1999). Note that these model dust coefficients differ from those listed in Schlegel et al. (1998) and Abbott et al. (2018).

shapes for DES *griz* and set the Y-band template equal to the z-band one. To infer the light curve shape, we first “fold" the well-sampled S82 RRab light curves from Sesar et al. (2010) into phase coordinates by taking the modulus of the Modified Julian Dates of the observations with respect to the pulsation period of each individual RRab. We “phase-align" the light curves by shifting them so that they all reach their maximum brightness at phase$= 0$. We smooth the light curves by removing observations with photometric errors ≥ 0.2 and linearly interpolating them in equally-spaced phase bins. Then, we shift all of the light curves so that the curves in each filter $ugriz$ have an average magnitude of $m_b = 0$. We sample each light curve on a grid in phase space so that a

single RRL is denoted by $X_{\varphi b}$ for $\varphi = (1, \ldots, \Phi)$ and $b = (1, \ldots, B)$ where φ indexes the phase (the grid has $\Phi = 100$ equally spaced phases) and b indexes the filter (total B filters).

To solve for the template shape which is most representative of the S82 RRab data, we define the following optimization problem. Let $X_{i\varphi b}$ be the magnitude for the i^{th} RRab, at phase φ in band b. Let $\gamma_b \in \mathbb{R}^{\Phi}$ be the template in filter b. The template matrix of all five bands is thus defined as $\Gamma = (\gamma_1, \ldots, \gamma_B) \in \mathbb{R}^{\Phi \times B}$. Let $a \in \mathbb{R}^n$ be the amplitudes for the n RRab in the SDSS S82 sample.

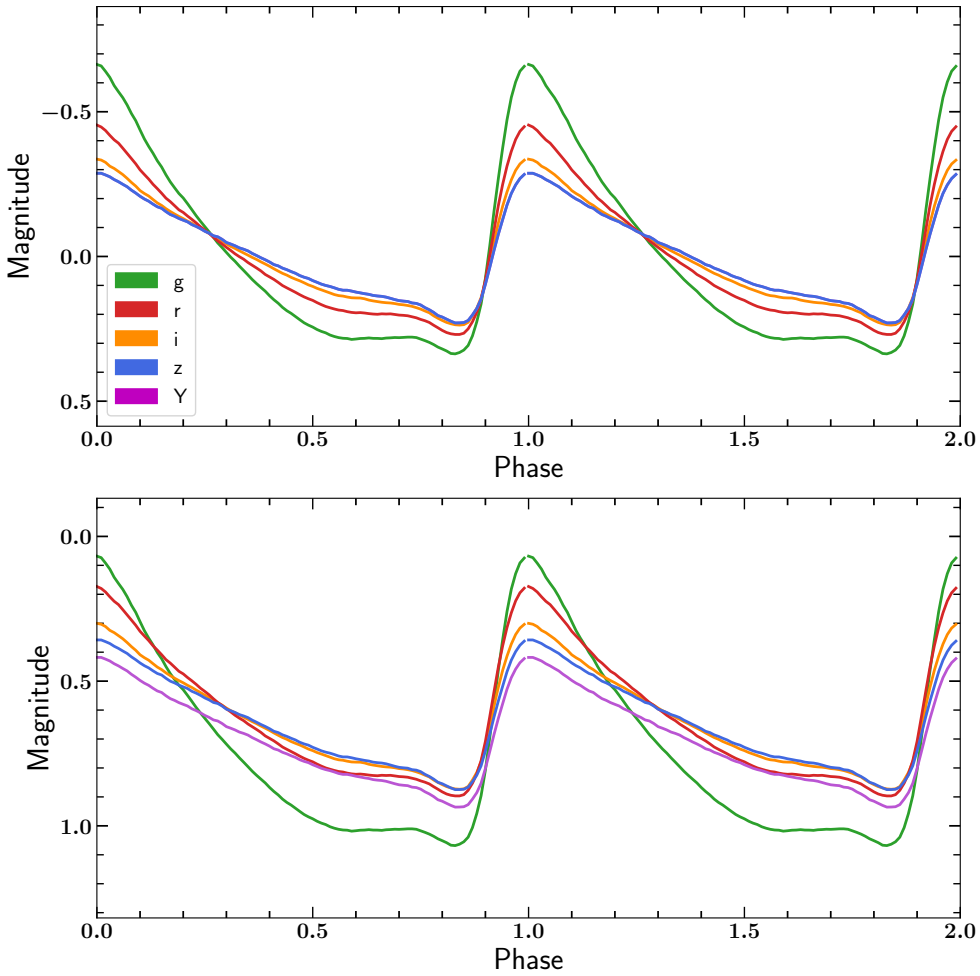

Figure 2.2: RRab template light curves in $grizY$. *Top:* Templates set to a mean magnitude of zero in each band, which highlights the decrease in amplitude as a function of wavelength. Note that the Y-band curve is not visible because it is defined to have the same shape as z. *Bottom:* Templates offset to the mean magnitudes of an RRL with P = 0.5 d.

Let $X_{i\cdot\cdot} \in \mathbb{R}^{\Phi \times B}$ represent the phase-folded, shifted, and normalized photometry described in the previous paragraph for the i^{th} RRab. To determine the Γ matrix of the template shapes, we solve the following optimization problem:

$$\min_{\Gamma, a} \sum_{i=1}^{n} ||X_{i\cdot\cdot} - a_i \Gamma||_F^2 \tag{2.5}$$

where $||a||_2 = 1$ (the Euclidean norm) for identifiability and F denotes the Frobenius norm, or the square root of the absolute squares of its elements. The resulting Γ matrix are the template shapes in each filter. To reflect the dependence of the RRab amplitudes on the filter in which they were observed, we rescaled the templates so the peak–to–peak g-band amplitude is 1 and the amplitudes of the other filter shapes are fractions of the g-band amplitude. These shapes and population parameter values form the set of templates that we use for fitting in our analysis. The base template shapes are shown with and without offsets between the bands introduced by the *P–L* relation in Figure 2.2.

2.3 Fitting the Model

The model is fit to a light curve by minimizing a weighted sum of squares (also known as "χ^2 minimization") with at most five free parameters μ, $E(B-V)$, a, ω, ϕ, or just four if the dust extinction parameter $E(B-V)$ is set to 0. The objective function is highly multimodal, so we perform a grid search across the frequency to avoid stopping prematurely at a local minimum.

At each frequency ω in the grid, we solve for the parameters μ, a, ϕ, and optionally E(B-V), using:

$$\min_{\mu, E(B-V), a, \phi} \sum_{b,i} \frac{\left[m_{bi} - M_b(1/\omega) - \mu - R_b \times E(B-V) - a\gamma_b(\omega t_{bi} + \phi)\right]^2}{\sigma_{bi}^2 + \sigma_{me}^2} \tag{2.6}$$

where b is the filter index, i is the epoch index, and $M_b(1/\omega)$ is calculated for that frequency gridpoint using Equation 2.4.

Long (2017) showed that using only the inverse of the observation uncertainties as weights

during the least-squares fitting is suboptimal when the templates are an approximation, so we weight the residuals by an additional model error term σ_{me}. To compute σ_{me}, we fit the template to all well-sampled SDSS RRab light curves and computed the difference between the squared residuals and the squared photometric errors σ_{bi}^2. σ_{me} is the square root of the average of these differences. The value across all of the SDSS bands $ugriz$ is 0.0547. We adopt this value for the DES data as well.

At each frequency gridpoint, we estimate the remaining parameters by using a block-relaxation method in which we alternate between minimizing across the $(\mu, E(B-V), a)$ parameters and minimizing across the ϕ parameter. This number of iterations can also be specified.

When minimizing across $(\mu, E(B-V), a)$ at fixed ϕ, the model is linear in $(\mu, E[B-V], a)$, so we find the closed-form weighted least squares solution. If the solution returns a non-negative amplitude, we then update the phase via the Gauss–Newton method described below; otherwise, we draw the phase randomly from a uniform distribution with interval [0,1].

When minimizing across ϕ, with fixed $(\mu, E[B-V], a)$, we cannot analytically solve for ϕ. Instead we use a Gauss–Newton method. In this process, we seek to minimize the objective function

$$g(\phi) = \sum_{b,i} \frac{(m_{bi}^* - \gamma_{bi}(\phi))^2}{\sigma_{bi}^2 + \sigma_{me}^2}. \tag{2.7}$$

where m_{bi}^* and $\gamma_{bi}(\phi)$ are defined as:

$$\begin{aligned} m_{bi}^* &\equiv m_{bi} - M_b(\omega) - \mu - E(B-V)R_b \\ \gamma_{bi}(\phi) &\equiv a\gamma_b(\omega t_{bi} + \phi) \end{aligned} \tag{2.8}$$

With $\phi^{(m)}$ as our current phase estimate, the Newton update has the form:

$$\phi^{(m+1)} = \phi^{(m)} - H(g)^{-1}(\phi^{(m)})\nabla(g)(\phi^{(m)}) \tag{2.9}$$

where $\nabla(g)$ and $H(g)$ are the first and second derivatives of g. We have

$$\nabla(g) = \frac{\partial g}{\partial \phi} = -2 \sum_{b,i} \frac{(m^*_{bi} - \gamma_{bi}(\phi))\gamma'_{bi}(\phi)}{\sigma^2_{bi} + \sigma^2_{me}}. \tag{2.10}$$

and

$$H(g) = \frac{\partial^2 g}{\partial \phi^2} = 2 \sum_{b,i} \frac{(\gamma'_{bi}(\phi)^2 - (m^*_{ib} - \gamma_{bi}(\phi))\gamma''_{bi}(\phi))}{\sigma^2_{bi} + \sigma^2_{me}}. \tag{2.11}$$

The Gauss–Newton update approximates $H(g)$ with

$$H^*(g) = 2 \sum_{b,i} \gamma'_{bi}(\phi)^2. \tag{2.12}$$

where we substitute H^* for H in Equation 2.9, rather than using $H(g)$ in Equation 2.11. This is a standard approach in non–linear regression which avoids computation of γ''_{bi} and ensures that the second derivative is positive (see Section 14.4 in Lange 2010). We approximate γ'_{bi} by storing numerical derivatives of the γ_b templates within the associated data files. At each new ω in the grid of frequency we obtain a warm start for the $\mu, E[B-V], a, \phi$ parameters by using estimates from the last frequency.

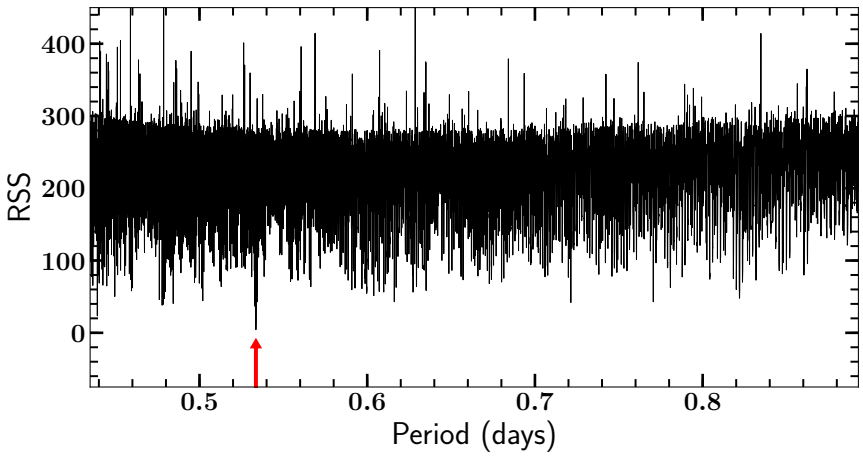

Figure 2.3: Residual sum of squares (RSS) curve for an RRab originally discovered by Sesar et al. (2010). The red arrow denotes the global minimum of the RSS which corresponds to the true period of 0.5336 days.

The best-fitting template parameters are chosen at the frequency gridpoint at which the RSS is minimized. Figure 2.3 shows the RSS as a function of period for a real RRab in DES Y3 data, with a red arrow denoting the location of the best-fitting template parameters. Figure 2.4 shows the results of fitting this template to the raw unfolded light curve of the same RRab (top) and its phased light curve with its best fitting template (bottom).

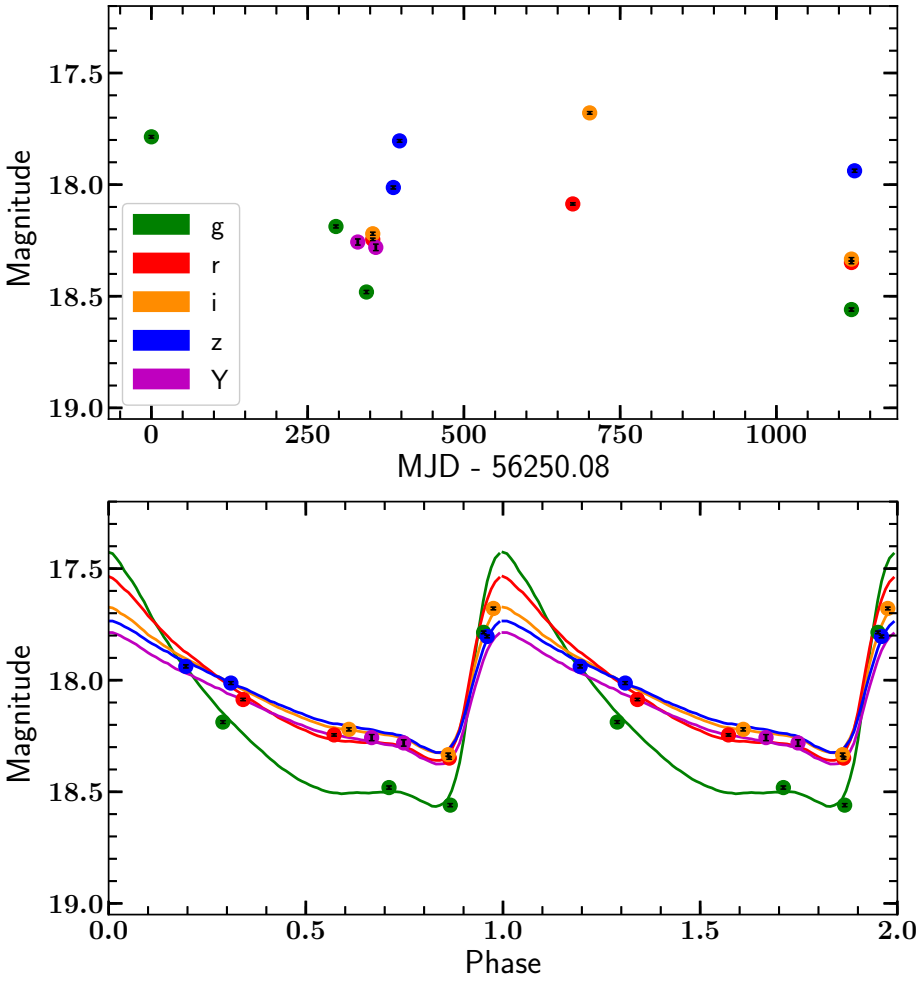

Figure 2.4: *Top:* Poorly sampled DES light curve of an RRab originally discovered by Sesar et al. (2010) (same star as Figure 2.3). *Bottom:* Phased light curve of the same source with the period correctly estimated by our algorithm. *Note:* Photometric uncertainties are smaller than the plotting symbols.

A major strength of this algorithm is that the template shape is fit simultaneously to the light curve data in all five bands combined. Since there are only four free parameters that must be fit for the entire light curve, unique solutions can be found for sparse light curves with very few measurements in any single band. There are several other well-documented methods available in the literature for identifying RRL in multiband data (e.g., VanderPlas and Ivezić 2015, Hernitschek et al. 2016 and Sesar et al. 2017), which yield excellent results for data sets with an average of 35 or more observations per light curve. We present this algorithm as an alternative to these other methods for especially sparse multiband data sets. The template and the associated fitting code are available at `https://github.com/longjp/rr-templates`. The template performance is examined further in the following sections in its application to real data sets from the Dark Energy Survey.

3. APPLICATION TO THE FIRST THREE YEARS OF DES*

In this section, we describe the application of the template described in the previous section to real sparsely sampled time series data from the first three years of the Dark Energy Survey.

3.1 Data

3.1.1 Y3 Quick Catalog

This work is based on the DES internal Year 3 Quick Release catalog (hereafter Y3Q2), which contains all the single epoch data from years 1-3 that formed the basis for the coadded DES first public data release[1] (Abbott et al., 2018, hereafter DR1). The “Quick" releases, so named because they typically precede the annual releases of the coadded data products, consist of a preliminary catalog of all sources detected in the data, along with their individual observations, from each exposure passing quality cuts. The full details of the DES image processing pipeline are discussed in full in Morganson et al. (2018); however, we provide a brief overview here.

After the DES images are acquired by DECam, they undergo “preprocessing", or basic corrections for instrumental effects. These include: bias subtraction, bad pixel masking, flat fielding, and removal of contaminant signals caused by the CCDs themselves. The pipeline then applies the “First Cut" calibrations, which include a basic astrometric solution and the removal of oversaturated pixels, cosmic rays, terrestrial satellites, and the sky background. Afterwards, the initial photometry is performed with SExtractor (Bertin and Arnouts, 1996), producing catalogs of measurements for all sources in each exposure. Once all the images from an observing season have been processed, the “Final Cut" calibrations are applied, which correct the photometry with a zeropoint offset derived using the entire season of data (Morganson et al., 2018). In the Year 3 data, this zeropoint correction used the Forward Global Calibration Module (FGCM; Burke et al., 2018).

Y3Q2 contains the single epoch catalogs generated from the reduced “Final Cut" DES images

*This section is reprinted with permission from Identification of RR Lyrae stars in multiband, sparsely-sampled data from the Dark Energy Survey using template fitting and Random Forest classification by Stringer, et al. 2019. *The Astronomical Journal*, 158, 1. Copyright 2019 by The American Astronomical Society.

[1] https://des.ncsa.illinois.edu/releases/dr1

(Morganson et al., 2018) and a cross-matched "coadded" catalog generated from these single epoch measurements. This catalog does not contain information from exposures in which an object was not detected at approximately a 5σ level. The DES Y3Q2 coadded catalog contains nearly 2.9×10^8 unique objects and spans the entire survey footprint with $S/N \sim 10$ at a median depth of 23.5, 23.3, 22.8, 22.1, and 20.7 mag in *grizY*, respectively (Abbott et al., 2018).

In the Y3Q2 data set, individual objects can have from 2 to over 50 observations depending on their location. We ensure that each light curve only contains observations taken in photometric conditions by requiring that each observation has a SExtractor warning value $\mathrm{FLAG} \leq 4$, is sufficiently far away from masked regions in the images ($\mathrm{IMAFLAG\_ISO} \leq 4$), and has a zeropoint correction available ($\mathrm{FGCM\_FLAG} \leq 4$). After these cuts, the median number of total observations for a given object is 10, while the median number of observations in each band across the survey region is 4. The effects of the survey coverage and these cuts are discussed more in §3.6.1.

3.1.2 Object Selection

We selected our objects using the Y3Q2 coadded catalog before examining the time series data, since the former contained most of the information needed to identify candidates (such as the number of times each object was imaged in each band and the star-galaxy classification). We further restricted the sample to stellar-like objects by following a prescription similar to Bechtol et al. (2015), based on the SExtractor (Bertin and Arnouts, 1996) SPREAD_MODEL parameter which selects stars well down to $r \sim 23$ (Drlica-Wagner et al., 2015). Lastly, we required at least five total observations to be able to search for variability.

We selected objects that are bright enough to be detected in multiple images by requiring the coadded PSF (WAVG_MAG_PSF) or the elliptical aperture magnitudes in the exposure with the best seeing in that band (MAG_AUTO) to be brighter than the median depth of the Y3Q2 single-epoch exposures across the entire survey region (see §3.1.1). We excluded all objects for which the coadded photometry errors exceed 0.3 mag in each of *griz* to reduce the number of spurious detections.

To ensure that we did not discard stars with missing data in a single band, we considered

these quantities separately for each of *griz*. We did not use the *Y* data for these initial selections because those exposures are generally taken under worse seeing conditions than the other bands (Diehl et al., 2016) and are thus a poor choice to use for star-galaxy separation. The star-galaxy separation we used performs best in riz due to the better seeing conditions for those observations, as discussed in §1.2. Including objects which passed this cut in g likely allowed some extended sources into our sample, which we discuss further in §3.5.1.

Although RRL have well-characterized colors, we did not employ a color cut in this early stage of the analysis because we did not want to exclude any potential RRL with poor coverage across filters or pulsation phase. Simultaneous colors were not available for some objects in the DES footprint, so we would have to use coadded magnitudes or magnitudes from arbitrary phases in the star's variation to calculate colors, which would expand the range of possible values for RRL in our data. The RRL template we describe in §3.4 provides the color information we need to identify RRL candidates. In the future, when more epochs of DES data are available, color cuts will be a more reliable RRL indicator prior to the template fitting.

In summary, our combined selection criteria were:

- ≥ 2 observations in *g,r,i,* or z
- $|\text{SPREAD\_MODEL}| \leq (0.003 + \text{SPREADERR\_MODEL})$ in *g,r,i,* or z
- $(16 \leq \text{WAVG\_MAG\_PSF} \leq \text{median depth})$ or $(16 \leq \text{MAG\_AUTO} \leq \text{median depth})$ in *g,r,i,* or z
- $(\text{WAVG\_MAGERR\_PSF} < 0.3)$ or $(\text{MAGERR\_AUTO} < 0.3)$ in *g,r,i,* or z

A sample of $\sim 1.5 \times 10^8$ objects passed all of these combined selection criteria. We used their time series data instead of their coadded values for the remainder of our analysis.

3.2 Variability Analysis

3.2.1 Error Rescaling

Photometric uncertainties can have a large impact on the success of our variability classification. We first account for both the photometric uncertainties reported by the DES pipeline and the uncertainties in the FGCM zeropoint solution[2] for each exposure by adding them in quadrature. Since photometric uncertainties can be over- or under-estimated for different magnitude ranges (Kaluzny et al., 1998), we calculated the reduced chi-squared statistic, $\chi^2_{\nu,b}$, from the median magnitude $\overline{m_b}$ in a given band b for each light curve:

$$\chi^2_{\nu,b} = \frac{1}{N_b - 1} \sum_{1}^{N_b} \frac{(m_{i,b} - \overline{m_b})^2}{\sigma^2_{i,b}}. \tag{3.1}$$

where N_b is the number of observations for a unique object in band b, $m_{i,b}$ is the i^{th} observation in that band, and $\sigma_{i,b}$ is the photometric uncertainty combined with the zeropoint uncertainty for that observation. As this statistic measures the goodness-of-fit to a constant value of $\overline{m_b}$, one would expect $\chi^2_{\nu,b} \approx 1$ for a non-variable source and $\chi^2_{\nu,b} > 1$ for variable sources.

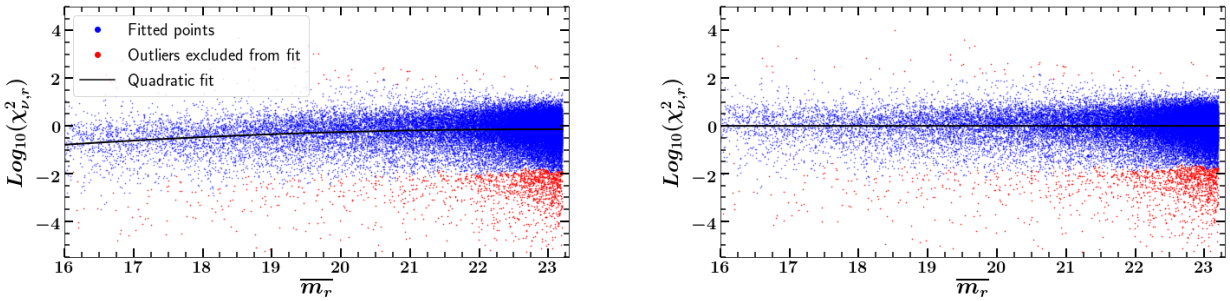

Figure 3.1: *Left:* Variation of $\mathrm{Log}_{10}(\chi^2_{\nu,r})$ vs. median r magnitude, $\overline{m_r}$, demonstrating that photometric errors are slightly overestimated for brighter objects in the DES pipeline. Red points were excluded using an iterative 3-σ clipping procedure. The black curve shows the quadratic fit that was used to rescale the errors. *Right:* Distribution after the photometric errors were rescaled.

[2]At the time of this analysis, only a pre-release version of the FGCM zeropoints was available. A later version of these zeropoints was used for other DES Year 3 analyses.

Since the majority of objects within a given field will have constant (non-varying) light curves, any overall trend of $\chi^2_{\nu,b}$ vs. magnitude will be indicative of incorrect estimations of photometric uncertainty. For ease of calculations, we subdivided the single epoch data by HEALPix (nside=32) (Górski et al., 2005)[3] and filter. This resulted in 1772 unique DES HEALPix regions. We fit a quadratic function:

$$\log_{10}(\chi^2_{\nu,b}) = c_{0,b} + c_{1,b}(\overline{m_b} - 20) + c_{2,b}(\overline{m_b} - 20)^2 \tag{3.2}$$

for each filter b in each of these regions, excluding variables and outliers by applying an iterative 3-σ clip from the median value using the `sigma_clip` function in `astropy.stats` (Astropy Collaboration et al., 2018). We show the initial trend in $\chi^2_{\nu,r}$ for the objects in HEALPix 11678 in the *r* band in the left portion of Figure 3.1. We multiplied the reported photometric uncertainties of each object by scaling factors based on the best-fit value of $\chi^2_{\nu,b}$ for each of its magnitudes in a given band. Once the uncertainties were suitably rescaled, we repeated the calculation to verify that no trends remained. The right portion of Figure 3.1 shows the resulting lack of trend in $\chi^2_{\nu,r}$ after the rescaling procedure. Table 3.1 lists the coefficients used to rescale the errors in each band for this example region (the full version is available online). Figure 3.2 shows the final rescaled photometric uncertainties for the entire survey region as a function of magnitude for the *r* band.

HEALPix	Band b	$c_{0,b}$	$c_{1,b}$	$c_{2,b}$
	g	-0.2672	0.0816	-0.0152
	r	-0.2572	0.0793	-0.0134
11678	i	-0.1180	0.0395	-0.0156
	z	-0.2160	0.0827	-0.0198
	Y	-0.1942	0.0505	-0.0250

Table 3.1: Error rescaling coefficients for Equation 4.2 for the HEALPix region 11678. The full version of this table is available at `https://des.ncsa.illinois.edu/releases/other/y3-rrl`.

[3]These HEALPix indices are also provided in the DES DR1 products (Abbott et al., 2018).

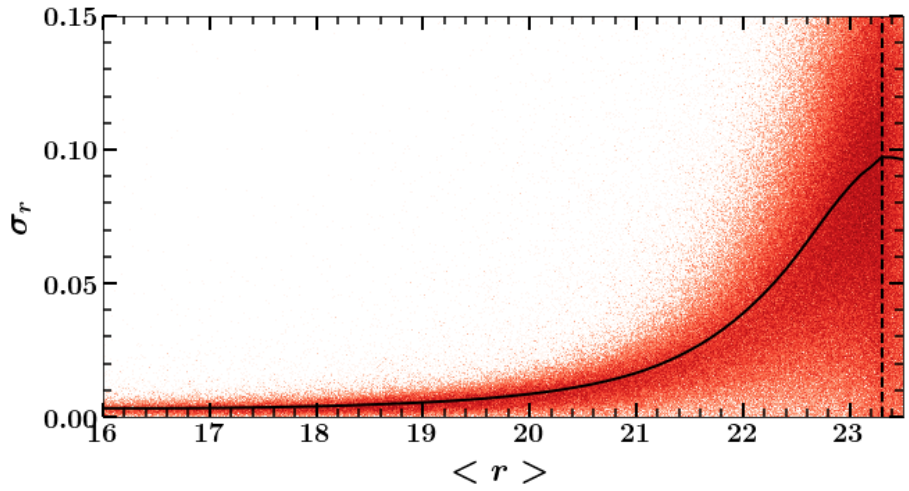

Figure 3.2: Uncertainties in the r-band magnitudes for the entire survey region after the error rescaling described in §4.1.1. The dashed black line denotes the median survey depth in this band and the solid black line shows the 3rd degree polynomial fit to the uncertainties.

3.2.2 Variability Cuts

Once photometric uncertainties were rescaled, we assessed the variability of each light curve using two simple metrics. The first was $\chi^2_{\nu,b}$ described in §3.2.1. The second was a metric we called "significance", consisting of a weighted range of the magnitudes in one band that acts as a proxy for light curve amplitude[4].

$$\text{significance}_b = \frac{(m_{\text{max},b} - m_{\text{min},b})}{\sqrt{\sigma^2_{\text{max},b} + \sigma^2_{\text{min},b}}} \tag{3.3}$$

To test the effectiveness of these metrics and determine the threshold values to separate variables from constant stars, we assembled a labeled training set of previously classified objects in SDSS stripe 82 region (hereafter, "S82"). S82 is a $\sim 300\,\text{deg}^2$ area spanning $300^\circ \lesssim \alpha \lesssim 60^\circ$ and $|\delta| \lesssim 1.25^\circ$ that was observed 70-90 times by SDSS in *ugriz* over a period of 10 years. Numerous authors used the resultant well-sampled multiband light curves to identify thousands of variable

[4]While other metrics such as the Welch-Stetson I (Welch and Stetson, 1993) and Stetson J (Stetson, 1996) indices are widely used and very effective at detecting variability, due to the sparsity of our observations, we chose to use metrics that were agnostic of observation time.

SDSS Label	Present in DES	Passed Cuts
RRab	238	234
RRc	58	57
Variables	16,752	5196
Standards	641,710	3004

Table 3.2: Training set of cross-matched S82 objects originally identified in Ivezić et al. (2007); Sesar et al. (2010); Süveges et al. (2012).

stars in the region with high confidence (Ivezić et al., 2007; Sesar et al., 2010; Süveges et al., 2012). These labeled objects are extremely useful for studies of variables from both hemispheres thanks to their equatorial location. Although the magnitude range of DES is deeper than that of SDSS, there is sufficient overlap to create a well-populated training set for our study. Using the calibration and variable catalogs from Ivezić et al. (2007), we cross-matched 641,710 "standard" (i.e., constant) stars and 16,752 variables in common between SDSS and DES objects. We also identified 296 RRL in common between DES and either Sesar et al. (2010) or Süveges et al. (2012), consisting of 238 and 58 objects of subtype RRab and RRc, respectively.

As an example, we show the cumulative distributions of $\chi^2_{\nu,b}$ values and "significance" values for the cross-matched objects in the *r* band in Figure 3.3. For both metrics, the threshold values were chosen to minimize the number of non-variable stars that would be subject to subsequent analysis. Any objects that showed $\log_{10}(\chi^2_{\nu,b}) \geq 0.5$ and significance ≥ 1 in any one of *grizY*[5] were kept for subsequent analysis. When these cuts were applied across all five filter bands, 234 ($\sim 98\%$) RRab, 57 ($\sim 98\%$) RRc, 5196 ($\sim 31\%$) variable, and 3004 ($\lesssim 0.05\%$) standard light curves from S82 met these criteria. These results for our training set are summarized in Table 3.2. Over the entire survey region, approximately $\sim 7 \times 10^5$ light curves passed these variability cuts. We caution that passing this criterion is simply an initial cut and does not imply that these sources are truly variable.

Despite these cuts, a small but non-negligible fraction of the objects identified as "standard"

[5]Unlike the initial cuts we applied to the coadded catalog, we included the *Y* band in these variability cuts because the *Y* band values were weighted by the photometric uncertainties.

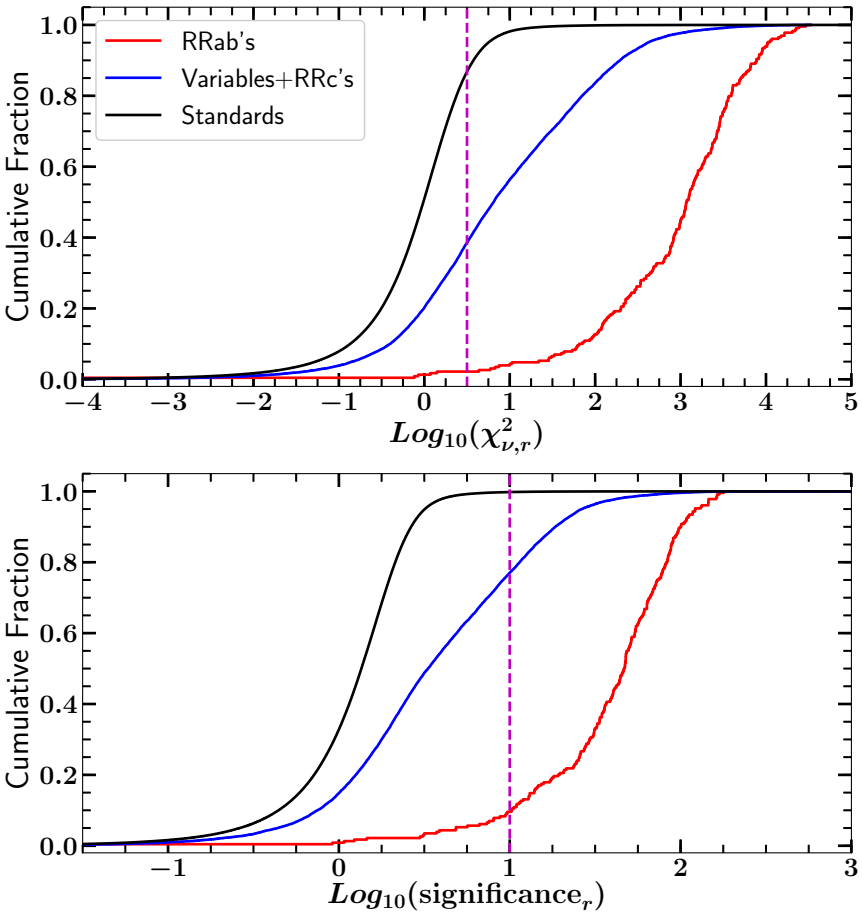

Figure 3.3: Initial variability metric values for previously identified objects in S82. *Top:* Cumulative distribution of $\log_{10}(\chi^2_{\nu,r})$. The magenta dashed line denotes the chosen threshold value of 0.5; objects with larger values in any band are considered variable. *Bottom:* Histogram of $\log_{10}(\text{significance}_r)$. The vertical magenta dashed line denotes the chosen threshold value of 1.0; objects with larger values in any band are considered variable. Note that although some real RRab are excluded by this cut, most of the non-RRab variables are also excluded.

by Ivezić et al. (2007) were still selected. It is possible that some of these objects are truly variable sources that did not display significant changes in the previous studies. Another possibility is erroneous photometry that, while rare, occurs sometimes in the Y3Q2 dataset due to incorrectly attributing observations from separate sources to one object or imperfect masking of observations obtained in very poor weather conditions. While these objects may have passed the initial variability cuts, their light curves fit the RRL template poorly, and most of them were rejected later in our

analysis.

All of the selected light curves were corrected for extinction using reddening values from the maps of Schlegel et al. (1998) multiplied by filter coefficients derived from the Fitzpatrick (1999) reddening law (for $R_V = 3.1$) and the adjustments to the Schlegel et al. (1998) map presented by Schlafly and Finkbeiner (2011) (see §4.2 in Abbott et al. (2018) for more details). We then used the extinction-corrected light curves as the input for our template fitting algorithm.

3.3 Fitting the Template

Given the large number of light curves showing variability, it was necessary to apply some restrictions to the template fitting prior to its application to keep the computation time at a reasonable level. Following the period-amplitude relation shown for RRab in Figure 16 of Sesar et al. (2010), we restricted the frequency grid search to values typical for most RRL ($0.44 \leq P \leq 0.9$ d) while excluding commonly-aliased periods introduced by the diurnal rotation of the Earth. Using the same reasoning as Sesar et al. (2017), we chose to exclude RRc from our study because: a) their sinusoidal light curves are difficult to distinguish from those of other variable objects such as eclipsing binaries, b) their small amplitudes would make them difficult to identify in our sparse data, and c) searching over a larger period range to recover their short periods ($\sim$ 0.3d) would introduce additional commonly-aliased periods into our sample. While excluding RRc weakens our sample size for tracing substructure, it is not prohibitive since RRc are usually less numerous than RRab. Furthermore, this approach allowed us to use only one generalized RRab shape for our template instead of an ensemble of shapes as in Sesar et al. (2017). While they were able to recover a more diverse group of RRL by fitting multiple shapes, our approach makes our algorithm more computationally efficient. We also fit the template with only four free parameters (μ, a, P, ϕ) since our light curves were corrected for extinction prior to the template fitting.

After fitting the template to our light curves selected in §3.2.2, we examined the offsets between the template parameter estimates and the previously estimated periods and distance moduli for the RRab in our training sample. At the best fit parameter estimates, the template fitting algorithm correctly estimated $\sim 89\%$ of the periods to within 1% of their previously estimated values. It

Parameter	% of RRab within 1%	% of RRab within 3%	$\sigma_{\rm parameter}$
$\Delta P/P_{\rm prev}$	88.89	89.74	6.81%
$\Delta D/D_{\rm prev}$	44.64	81.11	2.83%

Table 3.3: Template period and distance estimation accuracy in stripe 82 RRab in DES Y3 data. $P_{\rm prev}$ and $D_{\rm prev}$ are the values reported in Sesar et al. (2010) and Süveges et al. (2012).

also estimated ∼81% of the S82 RRL distances to within 3% of the values obtained by Sesar et al. (2010) and Süveges et al. (2012), if available, with an overall standard deviation of 2.8% (see §3.5.4 for an extended discussion of the uncertainties in distance modulus). The accuracy of the template estimates of both the period and the distance for the training set of RRab light curves is summarized in Table 3.3).

Our algorithm is computationally efficient and only takes $\sim 3-5$ minutes per light curve on an Intel Xeon E5420 processor. The template fitting code returned the estimated parameters of the top three best-fitting templates as well as the features used in the random forest classification detailed in §3.4.2 and Table 3.4. The computation time for fitting the template and calculating features for $\sim 7\times10^5$ light curves was ~ 44K CPU hours. For comparison to a similar analysis, our algorithm is $> 9\times$ faster than the template fitting methods used by Sesar et al. (2017), which required ~ 30 minutes per star.

3.4 Candidate Identification

3.4.1 Feature Selection

While it is possible to identify RRL by visually inspecting their phase-folded light curves, the sheer volume of light curves in our data set makes this classification method unfeasible. Instead, we computed numerical features to describe the behavior of the light curves. To assess the specific parameter space occupied by RRab, we compiled a training set consisting of all the cross-matched labeled objects from S82 which passed the initial variability cuts (discussed in §3.2.2). This left us with a training set of 234 RRab, 57 RRc, 5196 other variable objects, and 3004 "standard" sources. Since we only aimed to identify RRab, we chose a simple identification scheme with two classes:

RRab and non-RRab. This resulted in an RRab class with 234 objects and a non-RRab class with 8257 objects.

With the goal of identifying RRab, we chose features which were motivated by how well the light curves fit the RRab template and other observed properties of RRab. As demonstrated in Figure 3.3, RRab have relatively large $\log_{10}(\chi^2_{\nu,b})$ compared to most of the other objects in our sample. So, to quantify the base variability of the light curve while ignoring spurious signals or missing observations in any particular band, we included the median of this value calculated across all five filters as a feature. Additionally, most true RRab should fit the template with small residuals, so we quantified the quality of the best template fits using the RSS per degree of freedom, $\mathrm{RSS}_{\mathrm{dof}} = \mathrm{RSS}/(N_{obs} - 4)$. Then, to amplify the separation provided by these two characteristics, we divided the $\mathrm{RSS}_{\mathrm{dof}}$ by the median $\log_{10}(\chi^2_{\nu,b})$ to form another feature.

To take advantage of the distinctive amplitude ranges of RRab, we also selected the amplitude of the best-fitting template as a feature. We then created a new feature by dividing this amplitude by the $\mathrm{RSS}_{\mathrm{dof}}$, expecting that the large amplitudes and excellent template fits of RRab would clearly distinguish them from other objects. We can take advantage of these amplitudes again by evaluating how closely each object matches the observational trends shown by RRab in the first two Oosterhoff groups (see the introduction for a brief description). To measure how closely the objects' estimated template parameters matched these trends for RRab, we calculated the distance of the object in period-amplitude space from the Oosterhoff I relation measured in Sesar et al. (2010) and their shifted curve which separates the Oosterhoff I and II populations (see their Figure 16 and our Figure 3.9.)

Our last feature attempted to quantify the phase distribution of the observations in each light curve. Period-finding algorithms often recover periods at common aliases, sometimes resulting in light curves with many of their observations clustered near a particular phase. Because light curve phases are periodic, the two-dimensional case of the von Mises-Fisher distribution (Fisher, 1953; Jupp and Mardia, 1979) is a good approximation. This distribution can be written as:

Feature Name	Description	Importance
lchi_med	median $\log_{10}(\chi^2_{\nu,b})$ value across all bands	0.2232
amp_rss_0	Best-fitting Amplitude divided by the best-fitting RSS/dof	0.1942
f_dist1_0	Closest distance of best-fitting period/amplitude to Oosterhoff I relation from S10*	0.1591
rss_dof_0	RSS of the best-fitting template per degree of freedom	0.1571
f_dist2_0	Closest distance of best-fit period/amplitude to S10* curve dividing the Oosterhoff I and II groups	0.1025
amp_0	Best-fitting amplitude	0.0792
rss_lchi_med	RSS of the best-fitting template divided by the median $\log_{10}(\chi^2_{\nu,b})$ value across all bands	0.0502
κ_0	Best-fitting von Mises-Fisher concentration parameter of phases in the folded light curve	0.0345

Table 3.4: Random forest features. All of these feature values for each candidate are included in the electronic table at `https://des.ncsa.illinois.edu/releases/other/y3-rrl`. *Here, “S10" refers to Sesar et al. (2010).

$$f(x) = \frac{e^{\kappa cos(x-\mu)}}{2\pi I_0(\kappa)} \tag{3.4}$$

where κ is the concentration parameter, μ is the mean, and $I_0(\kappa)$ is the modified Bessel function of the first kind at order 0. The von-Mises Fisher distribution is akin to a Gaussian distribution wrapped around a circle, where the κ parameter is analogous to the inverse of the variance (see §2.2 in Sra 2016 for a more detailed description). We calculated this concentration parameter κ for each light curve folded over the best-fitting template period. Light curves with observations highly clustered in phase will have very large values of κ, aiding in the rejection of objects with aliased periods.

Although our choice of classifier is generally robust against non-informative features, we limited our features to these to make the classifier results easier to interpret. The features are summarized and ranked by their importance, or how much they contributed to splitting the data across all the decision trees in our classifier[6], in Table 3.4. These features are shown in Figure 3.4. The development of additional features to further separate the classes will be explored in future work.

3.4.2 Random Forest Classifier

To identify likely RRab automatedly and consistently, we trained a random forest classifier (Amit and Geman, 1997; Breiman, 2001) using these features. The random forest is a machine learning algorithm that predicts classes for data by combining results from a "forest" of decision trees. Each decision tree consists of a series of nodes where the data is split into subgroups based on the values of a random subset of their features, or characteristics. Before the random forest can make accurate predictions, it must be trained to recognize the trends in features that correspond to different classes. Thus, one needs a labeled training set to build the random forest. Each decision tree uses the labels to build a series of boundaries in feature space that divide the data into their correct classes. Once trained, the random forest algorithm assigns a score to unlabeled data based on the proportion of trees that identify them as a particular class. Random forest classifiers have

[6]See §1.11.2.5 in the `scikit-learn` documentation for more details.

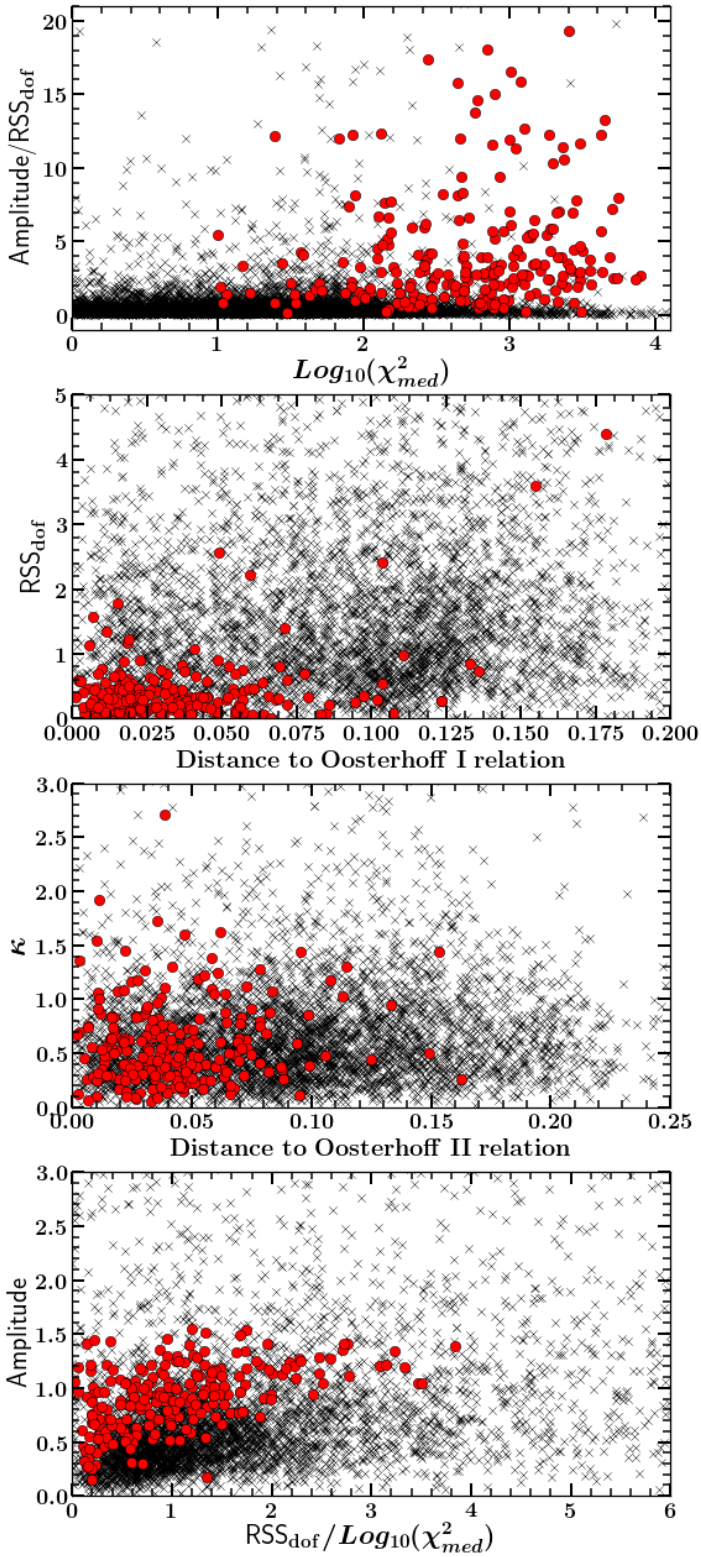

Figure 3.4: Features used to identify RRab plotted for the training set. Red points denote previously identified RRab while black X's are non-RRab. While the RRab clearly occupy a specific region in this feature space, they are not linearly separable.

Score Threshold	Purity	Completeness
0.00	0.043	0.983
0.05	0.402	0.928
0.10	0.567	0.886
0.15	0.661	0.852
0.20	0.727	0.840
0.25	0.773	0.819
0.30	0.815	0.798
0.35	0.845	0.756
0.40	0.877	0.722
0.45	0.896	0.693
0.50	0.922	0.651
0.55	0.955	0.630
0.60	0.953	0.596
0.65	0.956	0.554
0.70	0.968	0.525
0.75	0.973	0.470
0.80	0.971	0.432
0.85	0.988	0.348
0.90	0.982	0.231
0.95	1.000	0.071

Table 3.5: Purity and completeness of the training set as a function of classifier score. The full version of this table is available in the online data products.

been extremely successful in variable star classification (see Richards et al. 2011 for a comparison with other machine learning techniques), even in the case of sparsely sampled Pan-STARRS PS1 light curves (Hernitschek et al., 2016). Thus, the random forest was a natural choice of classifier for this study.

We created the classifier using the `RandomForest` package available in `scikit-learn` (Pedregosa et al., 2012). To prevent overfitting to our small training set and ensure repeatability, the classifier contained 500 trees with a maximum depth of 5, and used a random seed of 10.

We assessed the performance of our classifier by estimating the purity (the percentage of objects classified as RRab that were truly so) and the completeness (the percentage of real RRab that were identified as such) as a function of the class score reported by the random forest. The purity and completeness were estimated using a five-fold cross validation technique, where the data were

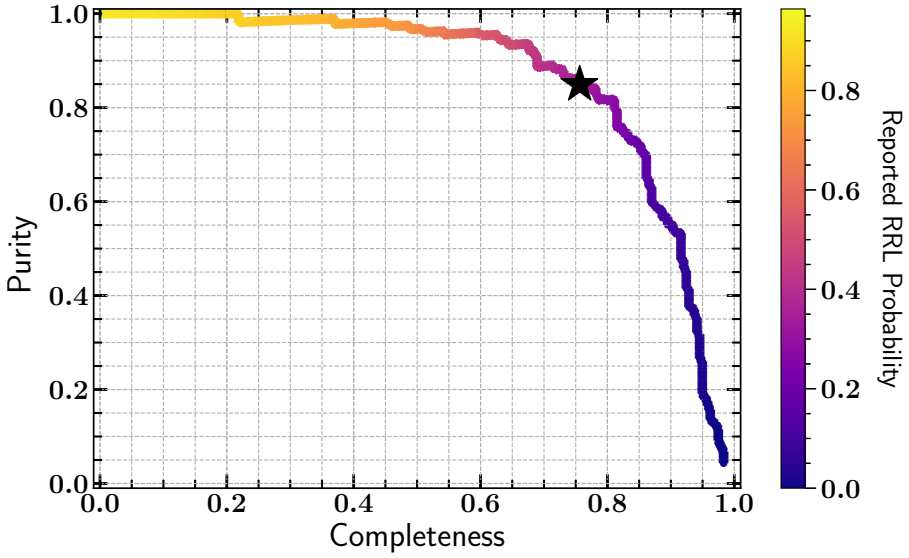

Figure 3.5: Purity/completeness curve for the random forest classifier trained on cross-matched objects in S82. The black star denotes a classifier-reported score of 0.35, where the purity is $\sim$ 85% and the completeness is $\sim$ 76%. The area under the curve is 0.864.

divided into five test groups and scored using a classifier trained on the other four groups. The classifier correctly identified 190 of the 234 RRab used to train the random forest as such with a score threshold of ≥ 0.35. As shown in Figure 3.5, defining RRab as objects with a score ≥ 0.35 yields a purity of 85% and a completeness of 76%. A common metric used to assess the performance of a classifier is the area under the curve (AUC) shown in Figure 3.5, which we find to be 0.864. The purity and completeness calculated at other score thresholds are listed in Table 3.5. We include all other objects with lower scores in our catalog so that other score thresholds can be specified by interested readers. Although an incorrect period estimate led to a worse RSS value for the fit, some RRab with incorrect period estimates were still correctly identified as such by the classifier.

Since our training set was mostly composed of nearby RRab confined to a small region in the survey footprint, it is imperative to assess our classifier performance using other samples of RRL. To this end, we cross-matched our sample with external surveys in §3.5.2 and applied our method to simulated RRab light curves at fainter magnitudes in §3.5.3.

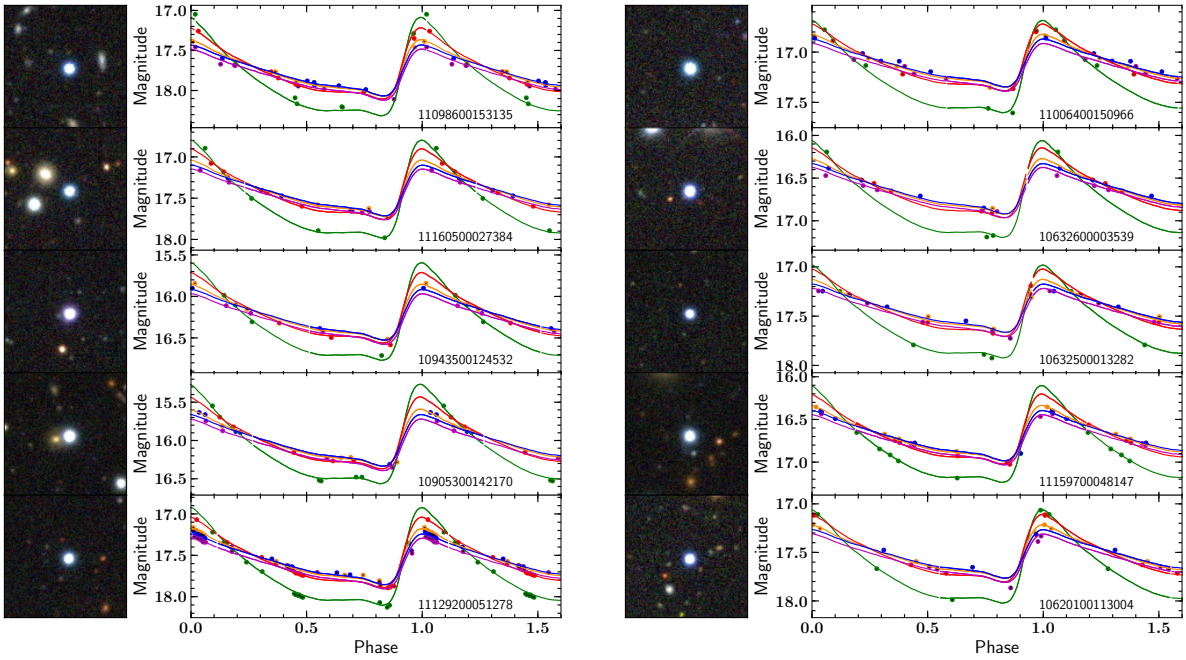

Figure 3.6: Sample of DES coadded images and representative light curves of visually accepted RRL candidates with classifier scores exceeding 0.94, labeled with their Y3Q2 ID number. The observations and templates are colored by filter using the same convention as Figure 2.4.

3.5 Catalog Description

3.5.1 Visual Validation

We applied the classifier to the $\sim 7 \times 10^5$ objects with template fits and found 8026 RRL candidates with a score ≥ 0.35. Although most of our candidates were indeed RRL found in other surveys, there were still some non-stellar interlopers in the sample due to the lenient initial cuts on the shape of the photometric point-spread function (§4.2). Thus, we visually inspected all RRab candidate light curves and their DR1 coadded images. After visually validating the candidates and removing any objects with non-RRL classifications in the Simbad database (Wenger et al., 2000), 1786 objects were discarded and 5783 RRL candidates remained in the catalog, with the rest too ambiguous to confirm. A sample of visually verified candidates with high ($p > 0.94$) and low ($p < 0.36$) classifier scores are shown in Figures 3.6 and 3.7, respectively. The most typical contaminants in the sample were extended sources. Given our lenient selection criteria described

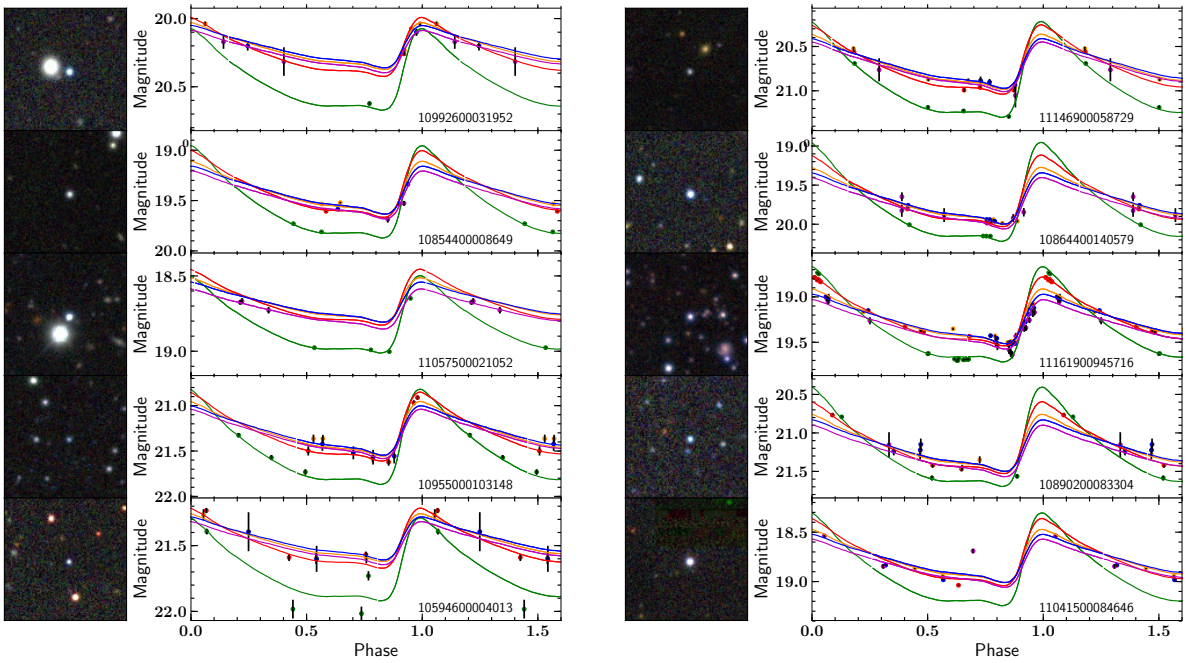

Figure 3.7: Sample of DES coadded images and representative light curves of visually accepted RRL candidates with classifier scores below 0.36, labeled with their Y3Q2 ID number. The observations and templates are colored by filter using the same convention as Figure 2.4.

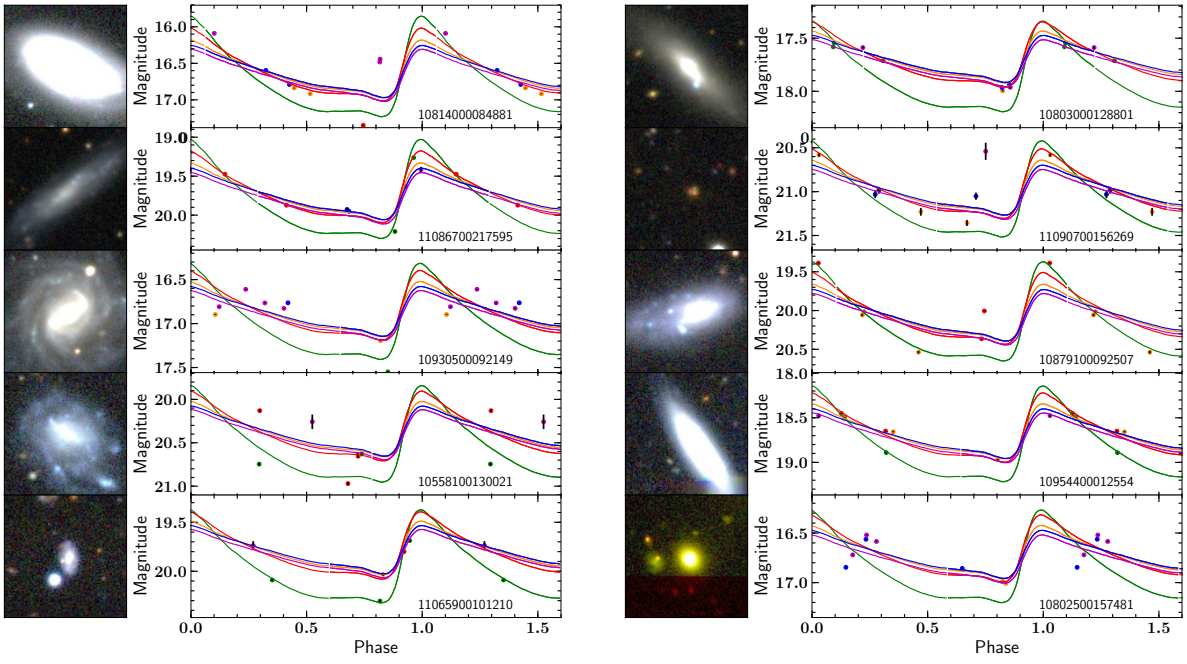

Figure 3.8: Sample of DES coadded images and representative light curves of visually-rejected candidates (extended sources or possible supernova) that passed the classifier score threshold, labeled with their Y3Q2 ID number. The observations and templates are colored by filter using the same convention as Figure 2.4.

in §4.2, it is not surprising that some of these objects made it into our final sample. Examples of candidates that were rejected by visual inspection as being extended sources are shown in Figure 3.8. The full catalog of candidates, their best-fit parameters, and their features are available at `https://des.ncsa.illinois.edu/releases/other/y3-rrl`.

Although the light curves have been visually inspected, further photometric observations of some extremely poorly sampled candidate light curves would be useful to confirm their classification. One may wish to remove these more uncertain candidates from their analysis by only considering objects with a larger minimum number of observations. Some of these candidates have gaps in observations near their maximum and minimum brightness, providing poor constraints on their estimated amplitudes and mean magnitudes. Therefore, we assigned a flag to each object based on how its phase-folded light curve is sampled. An object with fewer than two observations near its minimum brightness ($0.55 \leq \mathrm{phase} < 0.87$, which we chose to encompass both the near-constant portion of the light curve where other authors chose their minimum phase (e.g., Vivas et al., 2017) and the 10% quantile of template magnitudes) will receive a "flag_minmax" value of 1, while an object with < 2 observations near its maximum brightness ($0.96 \leq \mathrm{phase} < 1$ or $0 \leq \mathrm{phase} < 0.05$ corresponding to the 90% quantile in template magnitudes) receives a "flag_minmax" value of 2. Objects missing observations near both of these receive a flag value of 3.

Figure 3.9 shows a Bailey (period-amplitude) diagram of the candidates rejected by the classifier or our visual checks plotted in black, visually accepted candidates shown in red, and ambiguous candidates in blue. We plot the Oosterhoff I (Oosterhoff, 1939) relation and the curve dividing groups I and II from (Sesar et al., 2010) which we used in the calculation of our features in solid and dashed black lines. Many of these ambiguous candidates are likely RRab, but cannot be classified as such with high confidence in this work. Due to the sparse nature of our observations, we cannot detect amplitude modulations such as those arising from the Blažko effect (Blažko, 1907), although we did recover five out of twelve Blažko RRL previously identified in the Catalina Surveys (Drake et al., 2014, 2017).

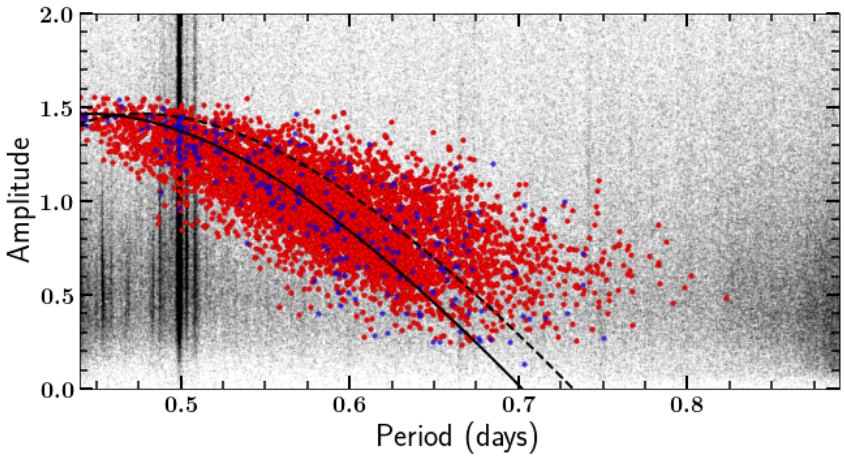

Figure 3.9: Bailey diagram of template-estimated amplitudes and periods for objects that passed the initial variability cuts in black and visually accepted RRab identified by our classifier in red. Ambiguous candidates that could not be visually accepted are plotted in blue. We overplot the Oosterhoff I relation and the curve dividing the Oosterhoff I and II populations from Sesar et al. (2010) in black solid and dashed lines, respectively. The abundance of objects with periods of $P = 0.5$ day denotes a common alias of the daily rotation of the Earth.

3.5.2 Comparison with Overlapping Catalogs

The DES footprint has significant overlap with other surveys, such as *Gaia* (Gaia Collaboration et al., 2016), Pan-STARRS (Chambers et al., 2016), the Catalina Surveys (Drake et al., 2009), and the Asteroid Terrestrial-impact Last Alert System (ATLAS: Tonry et al., 2018). We used our cross-matches with these external RRab catalogs to independently assess the performance of our algorithm at the different magnitude ranges probed by these surveys. We used the `SkyCoord` package in `astropy` (Astropy Collaboration et al., 2018) to select matches within 1arcsec of DES objects while removing duplicates. Details for each individual survey are presented in the following paragraphs and summarized in Table 3.6, while Figure 3.10 shows the respective overlaps with DES.

Clementini et al. (2019) found over 1.4×10^5 RRL in *Gaia* DR2, including $\sim 5 \times 10^4$ that were previously unknown. These variables were identified from multiband (G, G_{BP}, G_{RP}) light curves that had at least 12 observations in *G* (see Figure 10 in Holl et al., 2018). While the *Gaia* temporal coverage is very uneven, their RRL catalog spans the entire sky (see Figure 26 in Clementini et al.,

Survey	Area [deg^2]	Filters	Depth	Observational cadence	$N_{\rm obs}$	$N_{\rm RRab}$	$N_{\rm RRab}$ in DES	% found
SDSS stripe 82	$\sim$300	$ugriz$	$g\leq$21	most observed every 2 days	70-90	447	238	75
Gaia DR2	all sky	G_{BP}, G, G_{RP}	$G\sim$21	uneven, follows Gaia scanning law	12-240	140,000	4609	70
Pan-STARRS PS1	$\sim$30000	$grizY$	$r\leq$21.5	2 same-band obs. sep. by 25 min	$\sim$67	35,000	1021	79
Catalina Surveys	$\sim$9000	unfiltered	$V\leq$19-20	4 obs. within 30 min	$\gtrsim$200	32,775	1463	81
ATLAS	$\sim$13000	c, o	$r\sim$20	4$\times$ per night	$\sim$200	21061	484	81
DES single epoch	$\sim$5000	$grizY$	$g\sim$23.5	irregular	$\sim 50^*$	5783	5783	–

Table 3.6: Description of selected external RRL catalogs and their overlap with DES. The details of DES are listed for comparison. (*): by the end of the survey (Y6).

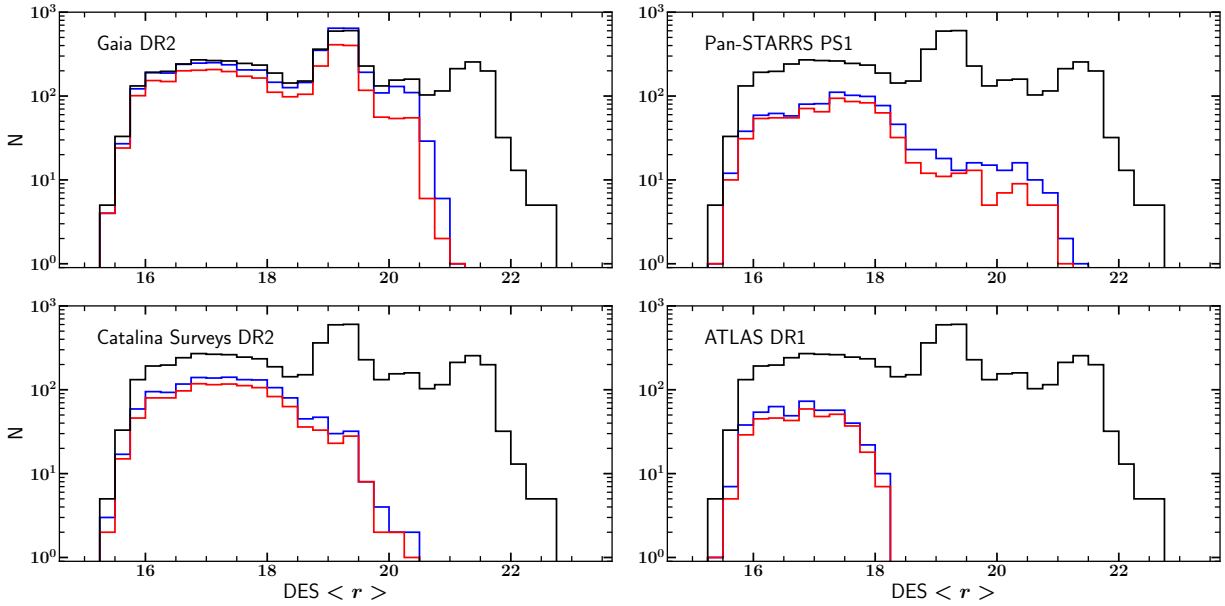

Figure 3.10: Histograms of magnitudes of RRab stars from external catalogs cross-matched with our DES initial stellar catalog, as a function of the extinction-corrected weighted average coadded DES r magnitude. *Top left: Gaia* DR2. *Top right*: Pan-STARRS PS1. *Bottom left*: Catalina Surveys DR2. *Bottom right:* ATLAS. Blue curves show the RRab from each catalog that were present in our sample before applying any cuts, while red curves show those that were identified as RRab in our analysis. Black curves show the distribution of DES RRab candidates and are the same in all panels. The overdensities at $r \approx 18.8$ and $r \approx 21.2$ correspond to the LMC outskirts and the Fornax dSph. Our catalog is deeper than the others by $\sim 1, 1, 2$ and 4.5 mag, respectively.

2019) and has high purity ($\sim 91\%$), making it an excellent independent check of our method at brighter magnitudes. 4609 of the *Gaia* DR2 RRabs were present in our initial stellar catalog (§4.2) and 3227 ($\sim$70%) were identified as such. To assess this recovery another way, if we create a purity vs. completeness curve from these cross-matches like the one shown in Figure 3.5, we find an AUC of 0.727. As we have significantly fewer single-band observations than *Gaia* DR2, it is not surprising that we do not recover all of their RRab.

We also searched for RRab discovered in Pan-STARRS PS1 by Sesar et al. (2017). Like DES, Pan-STARRS has sparsely-sampled multiband light curves and Sesar et al. (2017) employed a similar template fitting method to identify these variables. However, Sesar et al. (2017) used the final data release of PS1 with an average of 67 observations per object (compared to our median

of 18). We adopted their suggested *ab_score* cut of 0.8 to select only RRab from their catalog. As Pan-STARRS primarily surveyed the Northern hemisphere, we found just 1021 RRab in our initial stellar catalog, but we identified 805 ($\sim$79%) as such, with an AUC of 0.681. As the Pan-STARRS light curves are the most similar to the DES Y3 ones out of all the external catalogs under consideration, our similar classification results show that our approach is similarly effective as the methods used by Sesar et al. (2017).

The Catalina Surveys RRL catalog (Drake et al., 2013a,b, 2014; Torrealba et al., 2015; Drake et al., 2017) is based on a wide-field (26,000 deg^2) time series survey that probes the variable sky to a depth of $V \sim 19 - 20$ mag. The observations are unfiltered and collected in sequences of four images equally spaced over 30 minutes in each pointing (Drake et al., 2009). After several years of operation, the Catalina Surveys have over 200 observations for most of their variables (Drake et al., 2014), which makes the catalog largely complete. Given the limited magnitude overlap between the Catalina Surveys and DES, we only found 1463 of their 32775 RRab in our initial stellar catalog, but we identified 1185 ($\sim$81%) as such, with an AUC of 0.733.

ATLAS, a planetary defense initiative with a high cadence well suited for variability studies, recently released its first catalog of variable stars (Heinze et al., 2018). Thus far, ATLAS has at least 200 observations across two filters (c, o) over one-fourth of the sky. We select RRab stars from the ATLAS DR1 variable star catalog using the suggested CasJobs query in Appendix 10.2 of Heinze et al. (2018). As ATLAS is based in the Northern hemisphere and quite shallow compared to DES ($r \approx 20$ mag), we only have 484 of their 21061 RRab in our initial stellar catalog but identify 391 ($\sim$ 81%) as such, with an AUC of 0.635. This recovery rate is quite similar to the ones for Pan-STARRS and the Catalina Surveys.

In addition to searching for RRab candidates with previous identifications from the aforementioned wide-field surveys, we also checked for overlaps near the Magellanic Clouds (Soszyński et al., 2016), the Fornax dSph (Bersier and Wood, 2002), the Sculptor dSph (Martínez-Vázquez et al., 2016), in the General Catalogue of Variable Stars (Samus' et al., 2017), and in the SIMBAD database (Wenger et al., 2000). To the best of our knowledge, and based on publicly available

catalogs, 1795 (nearly 31% of our sample) are newly-discovered RRab candidates. Although the external catalogs under consideration are not complete, the fraction of their RRab recovered by our analysis is consistent with our estimate of $\sim 75\%$ completeness. Our method is just as effective (if not more so) at recovering RRL from sub-optimally sampled data than the methods used in comparable surveys.

Although we recover most of the RRab in the aforementioned overlapping catalogs, we can see from the AUC of each of these that there is a marked degradation in our algorithm's performance when applied to light curves outside our S82 training set. Thus, we use their AUC values to construct a confidence interval for the performance of our classifier. With the AUC of the training set and all four of these external cross-matches, we find a mean AUC of 0.728 with a standard deviation of 0.077. From this, we can determine that our classification methods have a lower effiency for fainter RRab. Unfortunately, we do not have well-characterized training data in a comparable filter system for fainter RRab, so we tested this with simulated light curves.

3.5.3 Estimated Recovery Rates and Uncertainties from Simulated Data

To estimate the robustness of our results for the noisier photometry at fainter magnitudes, we followed a method similar to Medina et al. (2018) and applied our method to simulated light curves with known light curve parameters in the DES filter system. We created the simulated light curves by sampling the smoothed templates of Sesar et al. (2010) in `gatspy` (VanderPlas and Ivezić, 2015) with the DES cadence from different areas of the survey. We shifted these light curves to various distances by adding the appropriate distance modulus and inserting scatter in the observations based on the magnitude-dependent uncertainty relations we found in §3.2.1 (shown in Figure 3.2).

Figure 3.11 shows the recovery rates of both the classifier and the period as a function of magnitude and total number of observations. As expected, the recovery rate of our algorithm decreases significantly with increasing distance modulus. This is mostly due to the larger photometric uncertainties and fewer observations due to the brighter limiting magnitudes for the redder bands (see §3.1.1). We see that the accuracy of the period estimation decreases following the trend of

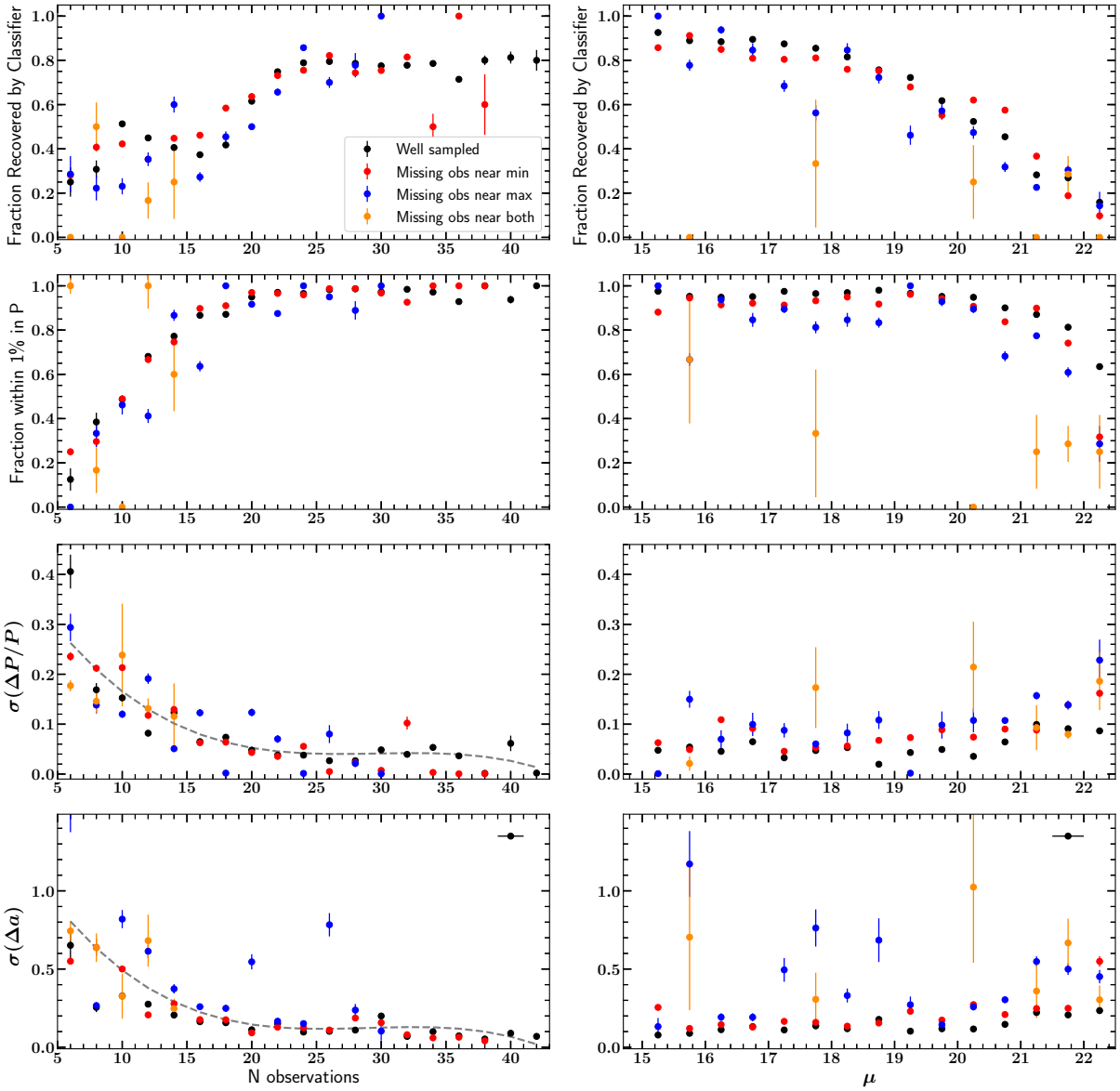

Figure 3.11: Recovery rates and parameter uncertainties as a function of the number of observations in the light curves and distance modulus μ. Colored points denote the behavior of the recovery fractions or parameter offsets for light curves with the phase sampling flags described in §3.5.1. Uncertainties on these values were estimated using jackknife resampling. The black points in the upper right corner of the bottom panels show the representative width of the bins in each column. Dashed grey lines show the best fitting 3rd degree polynomial to the trends shown by the combined simulated data used to assign uncertainties in the RRab catalog. The coefficients for these fits are listed in Table 3.7. *First row:* Fraction of simulated RRab light curves which received a classifier score ≥ 0.35. *Second row:* Fraction of estimated periods within 1% of the true input values. *Third row:* Standard deviation of the percent difference in period. *Bottom row:* Standard deviation of the offset in amplitude. *Note:* If not visible, uncertainties are smaller than the plotting symbols.

increasing photometric errors shown in Figure 3.11, and dramatically improves with increasing total number of observations up to $N \sim 20$. As expected, the RRab classification accuracy follows a similar trend. We find that our template fitting recovers the true period to within 1% for 95% of the simulated light curves with N=20 observations.

Beyond assessing our classifier performance with these simulated light curves, we can also use them to estimate the uncertainties of the best fitting template parameters. To make sure we treat light curves with especially poor phase coverage separately, we divided the simulated light curves into groups based on their "flag_minmax" values (described in §3.5.1). Then, we subdivided those into bins of two observations and 0.5 magnitude wide in N and μ, respectively. In each of these bins, we calculate the fraction of light curves with period estimates within 1% of their input values for each phase sampling group. To quantify the uncertainty of the period estimates, we calculated the standard deviation of $\Delta P/P = P_{est} - P_{true}/P_{true}$, where the "est" subscript represents the parameter estimate from the template fitting and "true" represents the input value of the simulated light curve. Likewise, we calculated $\Delta a = a_{est} - a_{true}$ to quantify the uncertainty of the amplitude estimates. The number of light curves included in each bin differs widely, so we estimate the spread of these uncertainty values within each subgroup with jackknife resampling. These results are shown in Figure 3.11.

Other than fluctuations due to the small sample sizes in some of the bins, these values follow expected trends. When there are fewer observations to constrain the parameter values during the template fitting, both the period and the amplitude are more uncertain, with these values beginning to stabilize around N=20 observations. In distance space, the parameter estimates are generally low until $\mu \approx 20$, where the brighter detection limits of the redder filters decrease the number of observations in the light curves. We have very few simulated light curves that are missing observations near their maximum only or both their maximum and minimum (the blue and orange points in Figure 3.11), so we cannot draw any definitive conclusions about the effect of phase sampling on the estimation of these parameters. We assign these parameter uncertainties to the real RRab candidates based on the best fitting 3rd degree polynomial to the trends in N observations

Value	p_0	p_1	p_2	p_3
$\sigma(\Delta P/P)$	4.8585$\times10^{-1}$	-4.5912$\times10^{-2}$	1.5636$\times10^{-3}$	-1.7574$\times10^{-5}$
$\sigma(\Delta a)$	1.5333	-1.5101$\times10^{-1}$	5.3006$\times10^{-3}$	-6.1034$\times10^{-5}$

Table 3.7: Coefficients for parameter uncertainties. The best fit 3rd degree polynomial is of the form $\sigma(\mathrm{Value}) = p_0 + p_1 N + p_2 N^2 + p_3 N^3$.

for all simulated light curves. We do not assign uncertainties to objects with $N > 43$ observations due to a lack of simulated data with that sampling. We also do not report these uncertainties for objects not identified as RRab by the classifier since these simulated light curves do not accurately represent the behavior of non-RRab. The coefficients of the best fitting polynomials are included in Table 3.7 and the uncertainties are included in the full catalog available at `https://des.ncsa.illinois.edu/releases/other/y3-rrl`.

The uncertainty of the remaining parameter ϕ is significantly more difficult to constrain. Phases for individual observations in the folded light curves are calculated using $\mathrm{phase} = (\mathrm{MJD}/P) \mod 1$. Any small offset in the period will compound over successive pulsations and result in a phase offset that varies over time. Even simulated light curves with $\Delta P/P < 0.0005$ (a difference < 1 minute) can yield $\Delta\phi \approx 0.5$ after three years when compared to the phases calculated using the input period. Thus, we do not report these uncertainties in ϕ as they require a level of period precision we do not attain even in light curves with $N > 20$. We caution against using the phases reported here for purposes other than plotting the template curves.

3.5.4 Uncertainties in the Distance Moduli

Since the absolute magnitudes of RRL depend on their metallicities (see Figure 14 in Marconi et al. 2015), the fixed [Fe/H] of our RRL model contributes systematic uncertainty to our distance estimates. Although the abundances of the individual RRL in our catalog are unknown, we can approximate the size and direction of this effect by comparing our results to those from an external catalog with metallicity measurements. The Catalina Surveys catalog of Torrealba et al. (2015) (hereafter T15) is convenient for this purpose because it has photometric estimates of [Fe/H] and a significant overlap with the DES survey footprint (although it has a brighter magnitude limit, see

§3.5.2. We calculated the difference in distance moduli for 521 RRL in common between both catalogs, $\Delta\mu = \mu_{DES} - \mu_{T15}$, which we plot as a function of [Fe/H] in in Figure 3.12.

We split the sample into bins of 0.1 dex in metallicity and perform an iterative 3-σ clip from the median value using the `sigma_clip` function in `astropy.stats`. We fit a linear relation between $\Delta\mu$ and [Fe/H]:

$$\Delta\mu(\mathrm{DES} - \mathrm{T15}) = (-0.058 \pm 0.003) + (0.168 \pm 0.009)\,([\mathrm{Fe/H}] + 1.5). \tag{3.5}$$

The root-mean-square error (RMSE) of the fit is 0.06 mag, consistent with the standard deviation of $\Delta D/D$ between this work and Sesar et al. (2010) listed in Table 3.3. Thus, we estimate our statistical uncertainty in distance moduli to be $\sigma_{\mathrm{stat}} = 0.06$ mag.

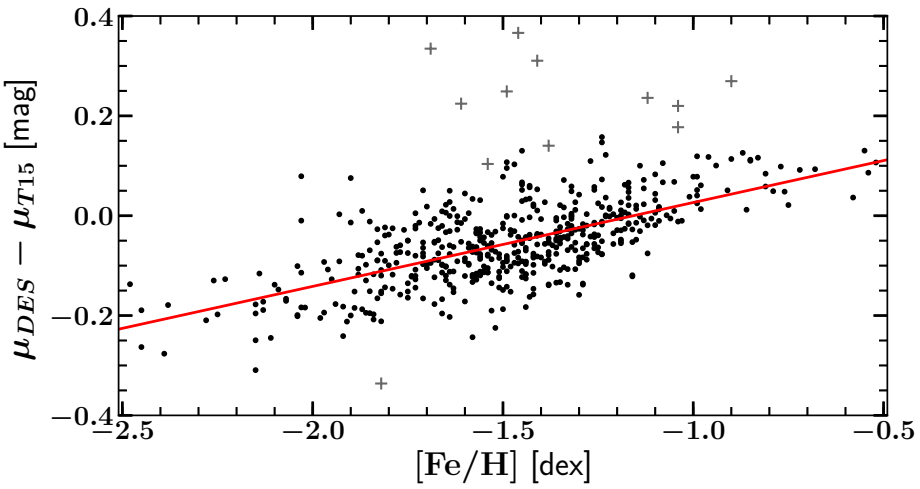

Figure 3.12: Difference in distance moduli between our work and Torrealba et al. (2015, T15) plotted against their photometric metallicity estimates. Stars that passed the 3-σ clip are plotted as black points, while the points that were removed are plotted as grey crosses. The best-fit linear relation fit to the clipped data is plotted in red. The RMSE of the fit is 0.06.

As is evident from Figure 3.12, our algorithm systematically underestimates distances for very metal-poor RRL and overestimates distances for more metal-rich RRL. While this cross-matched sample illustrates how much of an effect an RRab's metallicity has on the accuracy of our distance

estimates, we caution against using this sample to derive a metallicity correction to our distance estimates. The T15 RRL cover most of the spatial DES footprint, but our RRab catalog extends to fainter magnitudes than the magnitude limit probed by the T15 sample, which means we cannot assume the metallicity distribution of this sample accurately reflects that of the entire catalog. However, if we use this subsample and assume that the stellar halo metallicity distribution function is represented by a Gaussian with a mean of $[\mathrm{Fe/H}] = -1.5$ dex and standard deviation of $\sigma = 0.3$ dex (Ivezić et al., 2008) as in Sesar et al. (2017), we find a 1-σ systematic uncertainty of $\sigma_{[\mathrm{Fe/H}]} \approx 0.05$ mag in distance modulus. If we follow Medina et al. (2018) and estimate distance offsets for a metallicity shift of ± 0.5 dex and ± 1.0 dex in this subsample, we find a change in distance modulus of 0.08 mag and 0.17 mag, respectively. Again, we caution that the true distribution of metallicities in our full catalog is unknown, so these values are merely representative of the systematic uncertainty that would apply to particular stellar populations in the Milky Way halo. However, given our lack of metallicity information, we cannot quantify these systematic offsets without making such assumptions.

Another contribution to the systematic uncertainty we have not previously considered is the RRL evolution off the horizontal branch. We adopt the value $\sigma_{<V>} = 0.08$ mag, which Vivas and Zinn (2006) estimated from RRL in globular clusters (see their §4 and Figure 4). Adopting the halo metallicity distribution from Sesar et al. (2017), we add both sources of uncertainty in quadrature to arrive at $\sigma_{\mathrm{sys}} = (\sigma^2_{[\mathrm{Fe/H}]} + \sigma^2_{<V>})^{1/2} \approx 0.09$ mag.

We verify this estimate of systematic uncertainty by comparing our estimated distance moduli for various MW satellites with previously-published results. For the Fornax dSph, which has a horizontal branch [Fe/H] ≈ -1.8 dex (Rizzi et al., 2007), our median distance modulus is 0.05 ± 0.04 mag closer than the values of $\mu = 20.72 \pm 0.04$ and $\mu = 20.72 \pm 0.06$ mag found by Greco et al. (2005) and Rizzi et al. (2007), respectively. In the case of the Sculptor dSph, we find a median distance modulus 0.13 ± 0.04 mag closer than the value of $\mu = 19.62 \pm 0.04$ mag from Martínez-Vázquez et al. (2016). This larger difference is likely due to the large spread in metallicity exhibited by Sculptor's stellar populations, $-2.3 \lesssim [Fe/H] \lesssim -1.5$ dex (Martínez-Vázquez et al., 2016).

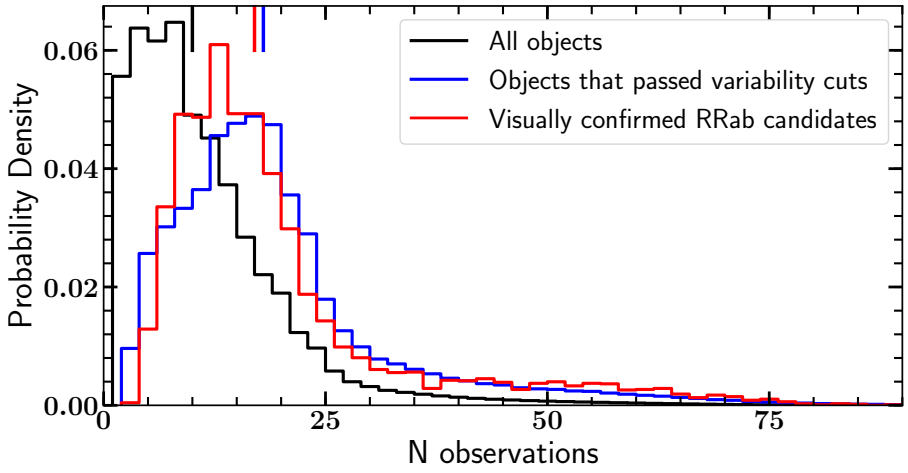

Figure 3.13: Histograms of the total number of observations across all bands for objects in the stellar sample (see §4.2) (black), objects which passed the variability cuts (blue), and the objects identified as RRab (red). Short line segments denote the median number of observations for each group (10, 18, and 17, respectively). Note that many of the RRab candidates have very few observations and would benefit from follow-up observations to confirm their nature.

Our distance estimate to the LMC, based on the RRL we found in its outskirts, is 0.12 ± 0.09 mag closer than the $\mu = 18.52 \pm 0.09$ mag found by Clementini et al. (2003). The LMC also has a spread of metallicities for HB stars, centered on [Fe/H] ≈ -1.5 dex with a dispersion of 0.4 dex (Clementini et al., 2003; Gratton et al., 2003). We expect that replacing the template's $M_b(P)$ relation with a calibrated *P-L-Z* or *P-L-C* relation in the DECam filters (K. Vivas et al., in prep.) will significantly reduce these offsets.

In summary, our distance moduli have 1-σ statistical and systematic uncertainties of 0.06 and 0.09 mag, respectively. The equivalent distance uncertainties are $\sim$2.8% (stat) and $\sim$4.2% (sys).

3.6 Discussion

3.6.1 Detection Biases

The strength of DES lies in its wide-field coverage and depth, but the results presented here are limited by the low number of multiband observations. Figure 3.13 displays histograms of the total number of observations for all objects in the stellar sample (black), all objects passing variability cuts (blue), and all RRab candidates (red). The median number of total observations

for each group, marked by a short colored line segment, is 10, 18, and 17, respectively. Note that most of our RRab have fewer observations than the N$\sim$20 observation threshold we saw from the simulation results in Figure 3.11. As future DES data releases will have an increased number of observations, we expect to find more RRL and have a more robust classification of the candidates presented here.

We note that the light curves used in this analysis typically had fewer total observations than the number expected from three years of DES data. We suspect that the total number of observations for the “stellar" sample is skewed by objects near the detection limits of DES, which suffer from noisy photometry and likely have few overlapping observations across all five filters. This low number of observations is also a result of the stringent quality cuts we applied on the single epoch photometry in §4.2. In future work, we aim to be more judicious in applying our photometric quality cuts so that we do not discard observations unnecessarily.

To verify that our sample is not affected by spatial fluctuations in the number of observations, we calculated the median number of total observations in each HEALPix of our Y3Q2 stellar data set. We show the median and the standard deviation of the total number of observations of light curves in each HEALPix in Figure 3.14. As expected, regions with the lowest number of observations fall near the edges of the survey footprint. Regions which have a median number of observations $\geq$ 25 correspond to the Science Verification region, in which 50 observations were made in the first year to demonstrate year 5 depth, and the DES Supernova fields, which are observed roughly weekly (e.g. Dark Energy Survey Collaboration et al., 2016). The linear patterns of constant Right Ascension are a result of the survey observation strategy (Abbott et al., 2018). Beyond these patterns, the DES photometry suffers in photometric completeness in crowded stellar fields near the central regions of nearby dSph galaxies and globular clusters, thus our catalog also suffers in completeness near those regions. Otherwise, the survey coverage is fairly uniform and we do not expect large scale trends in RRL detection outside of these fields of larger-than-average observation counts and dense stellar populations. We expect the addition of DES Y4-Y6 data to increase our detections of RRL considerably.

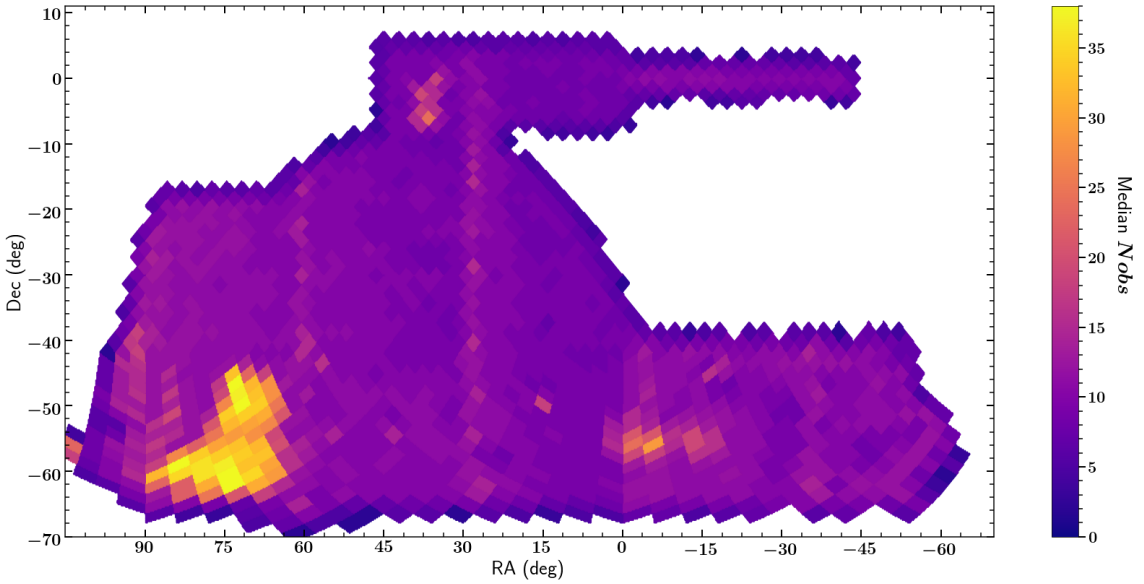

Figure 3.14: Spatial map of the median number of observations across all bands in each HEALPix. As expected, the regions with the fewest observations are near the edges of the survey region. The regions with a relatively large number of observations correspond to Science Verification or supernova fields. Outside these regions, the DES coverage is relatively uniform, but suffers from a small number of time series observations. Future studies of RRL will benefit from additional years of DES data.

Some additional biases in our RRab sample are results of choices made to exclude non-RRab from our analysis. While we weighted our initial variability cuts by the photometric errors to make the cuts robust against spurious observations (see §3.2.2), using these error-weighted metrics biased our variable sample against RRab with smaller amplitudes located at larger distances. We also excluded some real RRab from our sample by limiting the period range to $0.44\,\mathrm{d} \leq P \leq 0.89\,\mathrm{d}$ to avoid the common 1-day alias.

3.6.2 Spatial Distribution of the Candidates

The spatial distribution of the 5783 visually validated RRab candidates is shown in Figure 3.15. We also plot these candidates as a function of their heliocentric distance in Figure 3.16. In both figures, the overdensities of RRab candidates associated with (in order of decreasing heliocentric distance): the Fornax dSph, the Sculptor dSph, and the the outskirts of the Large Magellanic Cloud

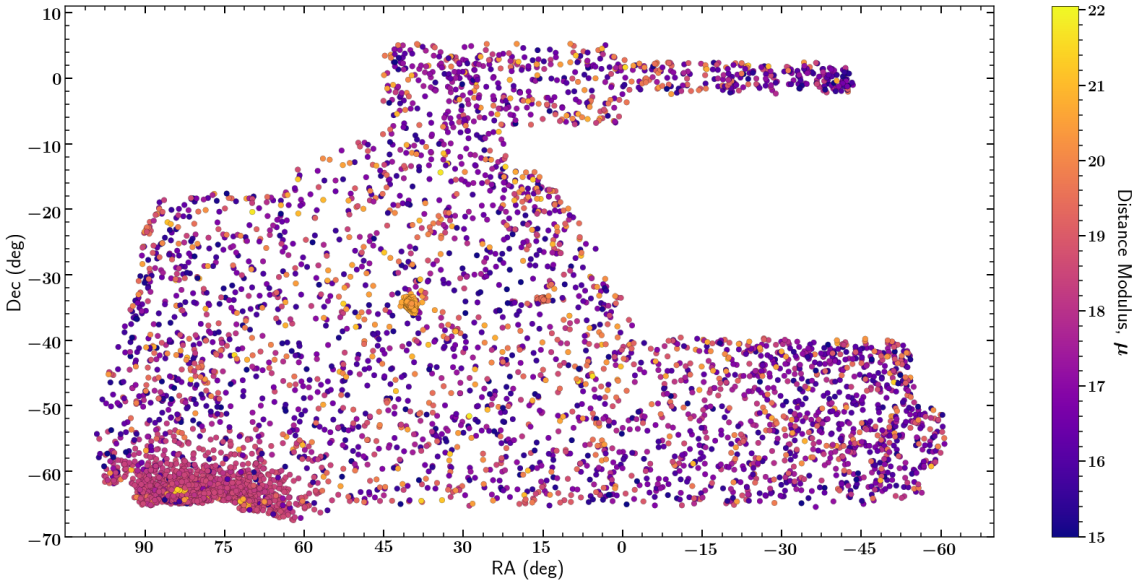

Figure 3.15: Map of 5783 visually accepted RRab candidates across the DES wide-field survey footprint. The RRab are marked by dots colored by distance modulus. Large MW satellite galaxies are easily distinguishable by their overdensities of RRab. The outskirts of the LMC are located near $(80°, -62°)$, the Fornax dSph is located near $(41°, -34°)$, and the Sculptor dSph is located near $(15°, -34°)$.

are easily visible. We expect that the inclusion of a metallicity term into the model combined with additional epochs of DES observations in the next release of this catalog will enable further characterization of these and other substructures.

One of the largest strengths of the DES data set is its depth (see our comparisons to other wide-field surveys in Figure 3.10). This is extremely valuable for our understanding of the outer halo as the current census of RRL known beyond 100 kpc falls short of the thousands predicted by simulations (Sanderson et al., 2017). In this work, we identified 800 RRab candidates beyond 100 kpc (most of which have been previously discovered) and eight RRab candidates beyond 200 kpc, all of which are new discoveries. The coadded images and light curves for the candidates beyond 200 kpc are shown in Figure 3.17.

The three most distant visually verified RRab candidates in our sample have heliocentric distances of ~ 231.6, 223.0, and 221.3 kpc. While these three stars are the most distant to-date RRab

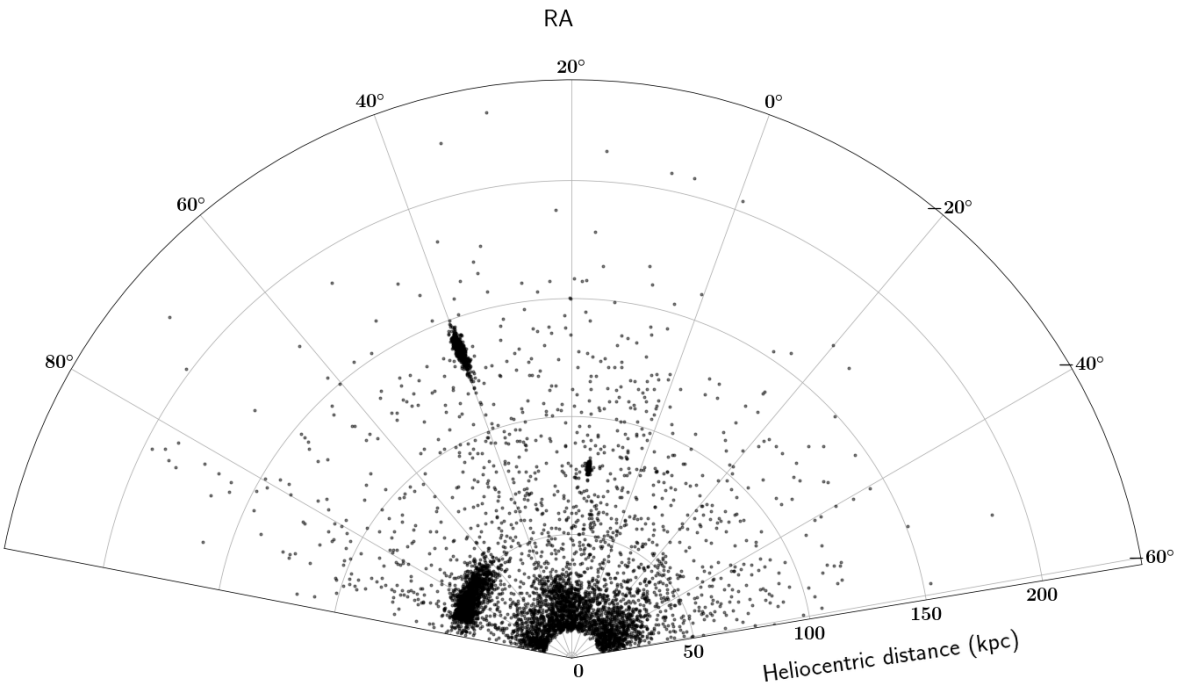

Figure 3.16: Radial distribution of the RRab candidates. The overdensities associated with (in order of decreasing heliocentric distance) the Fornax dSph, the Sculptor dSph, and the periphery of the Large Magellanic Cloud are easily distinguishable. Note: The Sculptor and Fornax galaxies appear elongated due to uncertainties in the RRab distance moduli.

in the Milky Way, they are not the most distant RRL. Medina et al. (2018) recently found two RRc with larger distances (232.9 and 261.2 kpc) using data from the HiTS Survey (Förster et al., 2016). Even though the candidates in our RRab sample suffer from a small number of observations and require additional follow-up for confirmation, the fact that there are so many RRab beyond 100 kpc and three RRab beyond 220 kpc provide reasonable evidence that the Milky Way stellar halo extends at least out to 220 kpc. Future DES data releases and other upcoming deep surveys such as LSST will increase the census of known RRL at this distance, enabling further characterization of the outer halo.

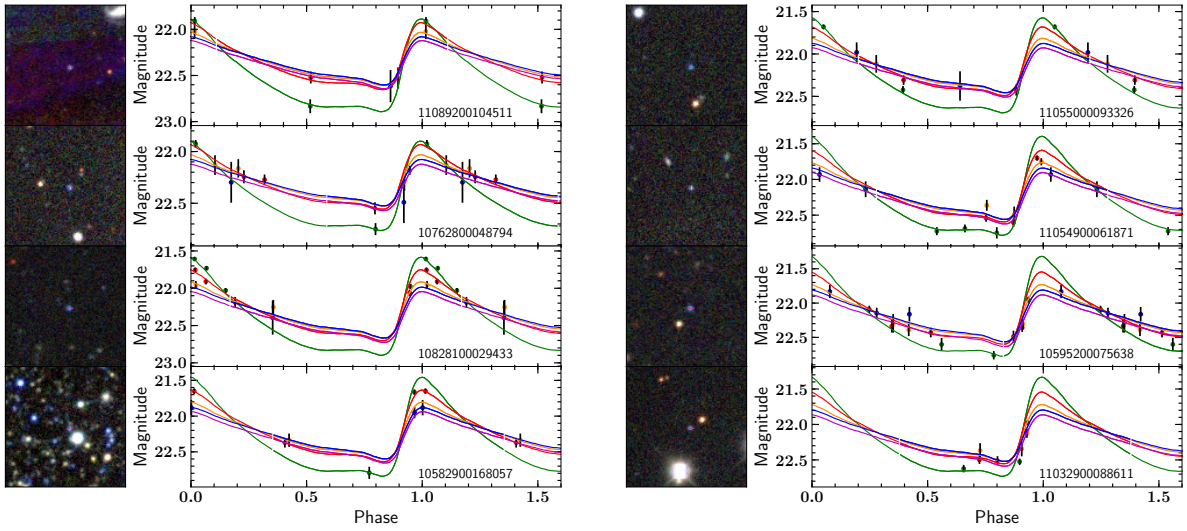

Figure 3.17: DES coadded images and representative light curves of visually-accepted candidates beyond 200 kpc, labeled with their Y3Q2 ID number. The observations and templates are colored by filter using the same convention as Figure 2.4. These very distant candidates have very few observations and will benefit from future DES data releases.

4. APPLICATION TO SIX YEARS OF DES DATA

In this section, we describe the preliminary analysis of the same template on all six years of the DES data, which will be later published in Stringer, et al. (in prep).

4.1 Y6 Quick Catalog

As in Section 3, the light curves for this work were assembled using the internal “Quick" release pipeline. The Year 6 Quick Release catalog (hereafter Y6Q) was constructed using survey exposures processed using the “Final Cut" pipeline. This pipeline applies instrumental calibrations and detrending corrections to the images, then creates photometric source catalogs for each exposure using SExtractor (Bertin and Arnouts, 1996). The full details of this pipeline are summarized in Morganson et al. (2018); however we note that in Y6, this process included a deeper detection threshold (the single epoch exposure catalogs now contain $\sim 3\sigma$ detections instead of the $\sim 5\sigma$ threshold used in prior data releases) and improved astrometric calibrations using Gaia DR2. The complete details of the Y6 calibration procedure will be released in a forthcoming publication by the collaboration.

After the images were reduced through the Final Cut pipeline, several quality cuts were applied to select exposures for the single epoch catalog. Any images with insufficient depth, poor seeing, poor sky subtraction, astronometric errors, or which contained artefacts such as ghosts, bleed trails, and plane streaks were not included. Additionally, only exposures with FGCM zeropoint solutions (Burke et al., 2018) were included in the catalog. These selections were applied to images from Science Verification (SV) through the end of the survey operations (Y6), yielding a total of 78,364 exposures.

Individual objects were identified by matching detections in one exposure to their nearest neighboring detections within an arcsecond radius in all other exposures using scipy.spatial’s `cKDTree` function (Virtanen et al., 2019). In the rare case when multiple detections from one exposure were assigned to one object, these doubled observations were split into multiple objects. All

objects with at least one detection in any band were included in the final coadded catalog to ensure the catalog included any single detections of transient and moving objects. Additionally, the observations were cross-referenced to their associated COADD_OBJECT_IDs in the Y6A1_COADD catalog to provide easy reference to quantities only available in the annual release.

The resulting single epoch catalog contained 610,043,115 total objects across the entire wide field survey footprint partitioned into regions of healpix nside=32 (Górski et al., 2005). Overall, the median number of observations in *grizY* was (1,2,1,0,0), respectively, with a median total number of observations across all bands of 6. As any object with a single detection was included in the final catalog, it is not surprising that these statistics are dominated by spurious objects. When we restrict these values to the 108,698,094 objects which were detected at least once in each band, the median number of observations in *grizY* becomes (7,8,8,6,4) and the median total number of observations across all bands becomes 34, almost doubling the number of epochs in the Year 3 release. Because of the decreased S/N ratio for detections, this catalog also extends deeper than the Year 3 observations by ~ 0.753 mag in each band, thus allowing us to analyze objects to a much fainter depth of $grizY \sim$ (24.33, 24.10, 23.54, 22.86, 21.45) at a $S/N \approx 5$ in Y6.

4.1.1 Error Rescaling

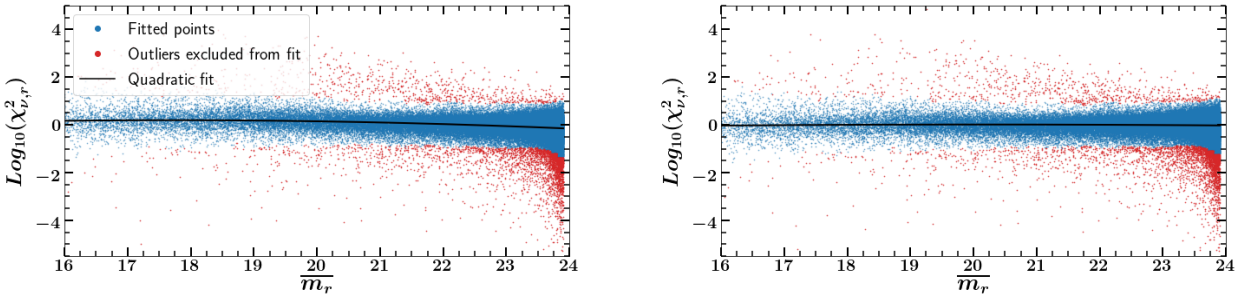

Figure 4.1: *Left:* $\mathrm{Log}_{10}(\chi^2_{\nu,r})$ vs. median r magnitude $\overline{m_r}$ for light curves in a sample DES healpix. Unlike Y3, DES errors are slightly underestimated for brighter objects in the Y6 data. Blue points show objects which were used to fit the quadratic curve in black, while red points were objects excluded by the 3σ clip. *Right:* We correct this trend by rescaling the photometric errors using the quadratic fit so that the remaining trend in $\mathrm{Log}_{10}(\chi^2_{\nu,r})$ is flat. Although this trend is very minor, it is necessary to correct because the trends differ slightly in $grizY$ and across the survey footprint.

Like in Section 3, we rescaled the magnitude errors of each observation according to trends shown in χ^2_{red} given by:

$$\chi^2_{\nu,b} = \frac{1}{N_b - 1} \sum_{1}^{N_b} \frac{[m_{i,b} - \mathrm{med}(m_b)]^2}{\sigma^2_{i,b}}. \tag{4.1}$$

for all stellar objects in the same region as a function of their median magnitude. We fit a quadratic function of the form:

$$\begin{aligned} \log_{10}(\chi^2_{\nu,b}) = \; & c_{0,b} \\ & + \; c_{1,b}\,[\mathrm{med}(m_b) - 20] \\ & + \; c_{2,b}\,[\mathrm{med}(m_b) - 20]^2 \end{aligned} \tag{4.2}$$

to the data. There was a noticeable trend in $\log_{10}(\chi^2_{red})$ in each band like in Section 3 (see Figure 3.1), however, in the Year 6 data, the uncertainties appeared to be underestimated for objects near the bright end of the DES detection limits, as shown in Figure 4.1. Although this trend is far less pronounced than we saw in Y3, we perform this correction since the trends differ slightly over the wide-field footprint. We performed this fitting for each healpix region in each band and multiplied the uncertainties of the observed "MAG_PSF" quantities using the appropriate scale factor calculated from these relations. This process effectively rescaled the errors and flattened the trends in χ^2_{red}.

4.2 Selection Cuts for Template Fitting

4.2.1 Stellar Source Selection

DES probes magnitude depths where many of the faint sources are galaxies, thus we perform an initial star-galaxy separation to preselect stellar sources. For this selection, we use the SPREAD_MODEL_I parameter from the exposure with the best depth as selected with the T_{eff} quantity (Neilsen et al., 2016). The *i* band is an ideal choice for star-galaxy separation because it typically has the best seeing of all the bands gri observed on moonless nights (see §2.3 in Abbott et al. (2018) and Figure 3 in Diehl et al. 2016). This differs from Section 3 in which objects that passed this spread model criterion in griz were considered to avoid omitting objects which were missing observations in a single band. While this enabled the catalog to be more com-

plete, it allowed many extended sources into the sample, which had to be removed visually by the authors. In all six years of DES, almost every non-transient source should have at least one measurement in *i*, so this is no longer a concern. Any object which passed $|\mathrm{SPREAD\_MODEL\_I}| < (0.003 + \mathrm{SPREADERR\_MODEL\_I})$, had a corresponding COADD_OBJECT_ID in the forthcoming DES DR2 catalog, and had at least 10 observations in its light curve was considered. Of the $\sim$610 million objects in the Y6Q catalog, $\sim$122 million passed this cut.

4.2.2 External Catalogs Used for Selection

After applying the star-galaxy separation and error rescaling, we further reduced the size of our catalog by selecting only objects which matched the color and variability range characteristic of RRL. First, however; we had to determine the typical values of these quantities for RRL in the DES data.

To assess the optimal place to make these selection cuts, we cross match objects in Y6Q with RRL found in external surveys. We include objects from SDSS Stripe 82 (Sesar et al., 2010), the Catalina Sky Surveys DR2 (Drake et al., 2013a,b, 2014; Torrealba et al., 2015; Drake et al., 2017), Pan-STARRS PS1 (Sesar et al., 2017), variables from the Sculptor dSph (Martínez-Vázquez et al., 2016), RRL from the Fornax dSph (Bersier and Wood, 2002), and RR Lyrae from Gaia DR2 with measured periods (Holl et al., 2018; Clementini et al., 2019; Rimoldini et al., 2019). As we intend to assess the success of Section 3 using the results from this analysis, we do not include the catalog of RRab candidates from Stringer et al. (2019) here.

To compare against other types of objects which may contaminate the sample, we also match with an internal DES catalog of $\sim$17 million standard sources which were used in the FGCM zeropoint calibrations (Burke et al., 2018). We randomly down-sampled the standard star catalog so that the RRab sample sizes and standard sample sizes were equivalent. We also removed any objects within 10 arcmin of the densely populated centers of the Fornax dSph and Sculptor dSph where the DES photometry suffers from crowding. This left a sample of 5020 RRab, 476 RRc, 46 RRd, 4 Blazkho RRL, and 5020 standard sources for developing reasonable cuts on these values. We discuss the detection efficiency for these external catalogs later in §4.4.

4.2.3 Color Selections

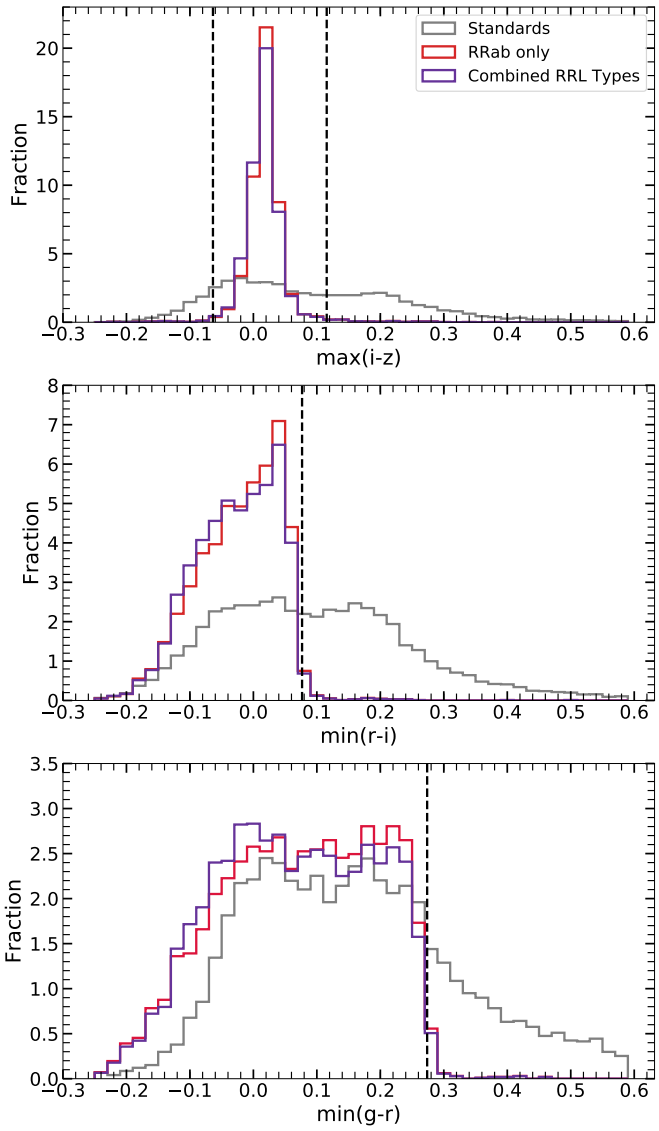

Figure 4.2: Multi-stage color cuts applied to the stars to remove non-RRL in order. Each panel shows the distribution of the extinction-corrected instant color for RRab in red, combined RRL types (including RRab, RRc, RRc, and Blazkho variables) in purple, and standard sources in grey. The black dashed lines indicate the cutoffs chosen to exclude non-RRL. *Top:* Distribution of $(i - z)_{\mathrm{max},0}$. Cuts were chosen at the 1% and 99% quantile values for the combined RRL distribution. *Middle:* Distribution of $(r - i)_{\mathrm{min},0}$. The cutoff denotes the 99% quantile value of the combined RRL population. *Bottom:* Distribution of $(g - r)_{\mathrm{min},0}$. The cutoff denotes the 99% quantile value of the combined RRL population. *Note:* The fractions quoted in the y-axes are a direct result of bin sizes and have no physical meaning.

Then, we applied a color selection to further winnow down the number of objects passed into the template fitting. This selection step sought to exclude stellar objects which are too red to be RRL, such as red giants or red main sequence stars. Even with the restriction on the minimum number of observations, the values of RRL colors calculated using coadded magnitudes are directly dependent on when the RRL was observed in its pulsation cycle, which can reduce the separation between blue RRL and other types of stars. Instead, we take advantage of DES observation patterns and measure “instant colors", or colors measured from observations taken at approximately the same time, directly from the light curves. To reduce the amount of time spent slewing between fields, DES often captures sequences of 2–3 exposures taken of the same field in different filters, with the filters chosen according to the seeing, Moon phase, and number of missing observations in that field (see Figure 3 in Diehl et al. 2016). To select these sequences, we group together any observations taken within an hour of each other and, depending on the filters used, calculate *g*-*r*, *r*-*i*, or *i*-*z*. In the case that there are duplicate instant colors for an object, we store only the maximum and minimum values. We were able to calculate at least one of these instant colors for most of our sample; however, some objects did not have any sequences of observations to use for these instant colors.

Thus, we developed a multistage color selection to remove objects based on their instant colors while also retaining any objects which did not have a particular instant color available. We examined all six instant colors using our training set to identify where to make the appropriate cuts. Although both maximum and minimum colors were measured for *g*-*r*, *r*-*i*, and *i*-*z*, we chose to use just the minimum or the maximum value for each color so that any object with only one instant color measurement would have a value. Using our sample of previously identified RRL, we defined selections as the 99% quantile value of the RRL population. All of these cuts are shown in Figure 4.2 with justification for each in the following section.

The first of these color selections was on the extinction-corrected maximum *i*-*z*. RRL have a very small range of expected colors near their minimum light which makes them useful probes for measuring extinction (Vivas et al., 2017). They also display much less metallicity dependence in

their luminosities at redder wavelengths (Bono et al., 2016, and sources within). This results in a narrow distribution of RRL colors for this value. We defined these color cutoff values at the 1% and 99% quantiles of the RRL distribution. Objects which had measured $(i-z)_{\mathrm{max},0}$ passed the entire set of color cuts if $-0.064 \leq (i-z)_{\mathrm{max},0} \leq 0.116$.

Any objects which did not have a measured $(i-z)_{\mathrm{max},0}$ but did have a $(r-i)_{\mathrm{min},0}$ were funneled into the next color cut. This cut and the following $(g-r)_{\mathrm{min},0}$ cuts are intended to target objects lying near the bottom left (blue) edge of the stellar locus. The value chosen to include 99% of the combined RRL training sample is $(r-i)_{\mathrm{min},0} \leq 0.077$. The final cut targeted faint objects which could potentially be missing observations in izY due to their brighter limiting magnitudes. Any objects which did not have measurements for the previous two colors was selected if it had $(g-r)_{\mathrm{min},0} \leq 0.274$. As can be seen from Figure 4.2, this is the least restrictive of the three cuts.

Any remaining objects without a valid measurement of $(i-z)_{\mathrm{max},0}$, $(r-i)_{\mathrm{min},0}$, or $(g-r)_{\mathrm{min},0}$ were included in the passing set of objects to ensure we did not discard faint objects with fewer observations. 98.56% of our RRab and 98.64% of our input RRab, RRc, RRd, and Blazkho RRL combined passed these subsequent color cuts, while ∼52 million of our overall stellar catalog passed.

4.2.4 Variability Selection

To help select potentially variable objects for template fitting, we calculated various statistics on the light curves in Y6Q, which are summarized in Table 4.1. Here, we describe the variability statistics used to select objects for template fitting, many of which were selected based on the results of the analysis of Sokolovsky et al. (2017). We measured these quantities using the MAG_PSF observations and their rescaled uncertainties from the relations described in §4.1.1. To avoid confusion, we will refer to the error-weighted mean as $\overline{m}$ and the median as med(m).

We use the $\log_{10}\chi^2_{red}$ to measure the base scatter in each single band light curve. As these quantities use the rescaled errors determined in 4.1.1, the non-varying sources have a distribution centered around 0, with positive outliers denoting true variable objects.

We also measure the range in magnitude, which we call $\Delta(\mathrm{mag})$ in each single-band light curve

Abbr. Name	Full Name	Bands Used	Ref.
IQR	Interquartile Range	g, r, i, z	
J	Stetson's J Statistic	$g, r, i, z, (grizY)$	1
Range	Magnitude range	g, r, i, z	
MAD	Median Absolute Deviation	$g, r, i, z, (grizY)$	
NAPD	N Absolute Pairwise Distances	$g, r, i, z, (grizY)$	
NXS	Normalized Excess Variance	$g, r, i, z, (grizY)$	2, 3
Q_n	—	g, r, i, z	4
χ^2_ν	Reduced Chi-Squared	$g, r, i, z, (grizY)$	
RoMS	Robust Median Statistic	$g, r, i, z, (grizY)$	5
S_n	—	g, r, i, z	4

Table 4.1: Variability statistics calculated on Y6Q light curves. References listed: (1) Stetson 1996, (2) Nandra et al. 1997, (3) Simm et al. 2015, (4) Rousseeuw and Croux 1993, (5) Enoch et al. 2003.

to relay information the amplitude of an object's variation. The uncertainties on the maximum and minimum magnitudes used to calculate this quantity are recorded as well.

Another more robust proxy for variability amplitude is the Normalized Excess Variance (σ^2_{NXS}). This statistic was first defined by Nandra et al. (1997) as

$$\sigma^2_{NXS} = \frac{1}{N\overline{m}^2} \sum_{i=1}^{N} [(m_i - \overline{m})^2 - \sigma_i^2]. \tag{4.3}$$

Although this metric is commonly used for x-ray analyses of AGN, it has successfully been deployed on the sparsely sampled Pan-STARRS 3π optical light curves (Simm et al., 2015).

We measure the overall scatter of a light curve using the Median Absolute Deviation (MAD).

$$\mathrm{MAD} = \mathrm{med}\,(\ |m_i - \mathrm{med}(m)|\ ) \tag{4.4}$$

MAD is slightly more robust to outliers than the standard deviation as it does not amplify the effects of an outlier by squaring it. This metric should be sensitive to repeated variations, however a real RRL with observations sampled at close to the same phase value will not appear variable in MAD.

The Robust Median Statistic (RoMS) is a more robust analog of χ^2_{red}, which is more robust to bias in the presence of non-Gaussian uncertainties. This metric was first defined in Enoch et al. (2003) as:

$$\mathrm{RoMS} = \frac{1}{n-1} \sum_{i=1}^{N} \frac{|m_i - \mathrm{med}(m)|}{\sigma_i} \tag{4.5}$$

In a single band, RoMS tends toward values of 1 for non-varying sources.

S_n and Q_n are robust alternatives to the MAD first proposed by (Rousseeuw and Croux, 1993). These metrics seek to measure the midpoint of a dataset like MAD, but do not rely on a central reference value and are thus better estimators for asymmetric distributions. S_n measures the median of the median of pairwise differences between all combinations of the observations and is defined as:

$$S_n = 1.1926 \, \mathrm{med}_i(\, \mathrm{med}_j(\, |m_i - m_j| \,)) \tag{4.6}$$

where m_i and m_j are separate observations. Q_n is a similar metric which is defined as:

$$Q_n = 2.2219 \, (\, |m_i - m_j|; \; i < j \,)_k \tag{4.7}$$

Q_n records the *k*th value in the absolute pairwise differences between all the observations divided by their combined uncertainties. k is the binomial coefficient $\binom{h}{2}$ with $h = \mathrm{floor}(n/2) + 1$ for n observations. Thus, Q_n records roughly the midpoint of these values. Another way to measure this is to calculate quantiles for the differences in separate observations. We use the 90% quantile values of these error-weighted N absolute pairwise distances (NAPD) as a proxy for the weighted range that is less sensitive to outliers.

Stetson's J variability index (Stetson, 1996) has been widely used to identify pulsating variables such as Cepheids and RR Lyrae. It builds upon the Welch-Stetson variability index *I* (Welch and Stetson, 1993) which measures the correlation between subsequent pairs of observations. Stetson's J index measures this correlation using single observations as well as pairs, thus we can apply it on

both the single-band and multiband light curves.

$$J = \frac{\sum_{k=1}^{n} w_k \, \mathrm{sgn}(P_k) \, \sqrt{|P_k|}}{\sum_{k=1}^{n} w_k} \tag{4.8}$$

where sgn is the sign function and

$$P_k = \begin{cases} \text{pair} & \left(\sqrt{\frac{n_v}{n_v - 1}} \frac{v_i - \overline{v}}{\sigma_{v_i}}\right) \left(\sqrt{\frac{n_b}{n_b - 1}} \frac{b_i - \overline{b}}{\sigma_{b_i}}\right) \\ \text{single} & \frac{n_v}{n_v - 1} \left(\frac{v_i - \overline{v}}{\sigma_{v_i}}\right)^2 - 1 \end{cases} \tag{4.9}$$

for pairs of observations in bands *v* and *b* and for single observations. For $\overline{v}$ and $\overline{b}$, we calculate the weighted mean for the observations in that band. Sources with purely noisy light curves have values close to zero. To create the pairs or triplets for this calculation, we group together any observations taken within an hour. Any group with three observations abc within the same hour was treated as three pairs ab, bc, ac, each weighted with a factor of $2/3$ as prescribed in Stetson (1996). All other groups with one or two observations are weighted equally with a factor of 1. For this measurement, we excluded the generally noisier observations in Y.

Since we had numerous metrics at our disposal with many of them potentially correlated, we trained a Random Forest classifier (Amit and Geman, 1997; Breiman, 2001) to select potential RRL for further study instead of determining cuts by hand. Random Forests are a good choice for this task because they are mostly insensitive to uninformative features, so the inclusion of a feature which does not separate the object types well will not harm the overall results. For this classifier, we used the `Random Forest` implementation in `scikit-learn` (Pedregosa et al., 2012). Our training set consisted of an equal number of standard sources and RRab; their distributions are shown in Figure 4.3. Any missing values for a specific feature were imputed with the corresponding median value of the training population.

The cutoff classifier score was chosen based on the F_β score, given as Baeza-Yates and Ribeiro-

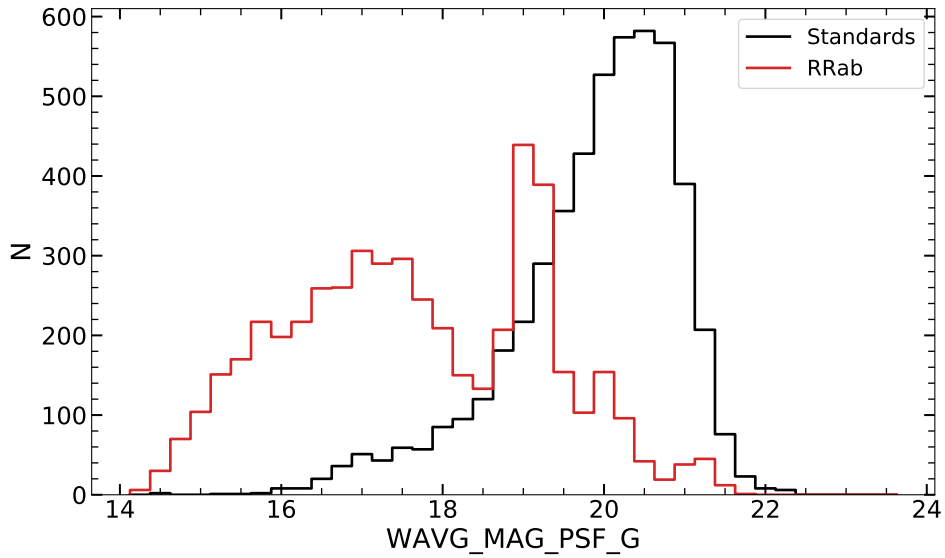

Figure 4.3: Distribution of the RRab and standards used as the training set for the variability classifier. These objects passed the color cuts applied prior to this classification stage. It is worth noting that the RRab (plotted in red) do not follow a constant distribution with respect to magnitude and correlate with the positions of real structures in the Milky Way halo, a pattern which is not reflected in the distribution of the “standard" nonvarying sources, plotted in black.

Neto (1999):

$$F_\beta = (1+\beta)^2 \frac{\text{precision} \cdot \text{recall}}{\beta^2 \cdot \text{precision} + \text{recall}} \tag{4.10}$$

where precision is the percentage of time the classifier was correct in assigning a label of “RRab" and recall is the equivalent of completeness, or how many true RRab were labeled as such by the classifier. We chose this particular score over other popular metrics like informedness or the F1 score because we wished to prioritize completeness at this stage in the analysis and the F_β score with β=2 allowed us to weight the recall twice as high as the sensitivity to ensure this. The hyperparameters for the number of trees, maximum depth of the trees, and number of features were tuned using a grid search and the values were chosen where F_β for the training set approached asymptotic behavior.

The resulting cutoff value which maximized F_β was 0.245. This value yielded a sample RRab purity of 92.30% and a completeness of 98.03% when applied to the training set only. We caution

that this purity value is not truly representative of all the objects in DES since we downsampled the non-varying sources significantly to make the class sizes equal for classifier training and neither our RRab or standard sample extends to the full depth of the Y6Q photometry. The resulting performance curves for the initial variability classifier and its top features are shown in Figure 4.4 and Table 4.2, respectively. Although they were not included in the classifier training, 98.84% of the RRc, 97.83% of the RRd, and 100% of the Blazkho RRL also passed this classifier. When we applied this classifier to the stellar sample which passed the color cuts, 117,383 of the objects remained. With all of these cuts combined, 96.84% of our input RRab and 96.98% of all RRL types combined were passed into the template fitting.

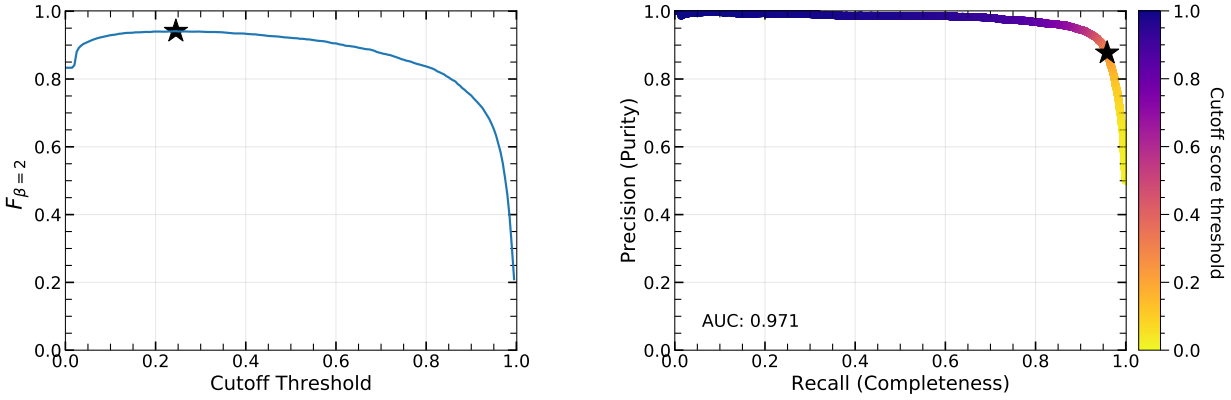

Figure 4.4: Performance curves of the initial variability classifier. *Left:* F_β scores over all possible cutoff score choices. The black star denotes where F_β is maximized at a value of 0.18. *Right:* ROC curve of the RF classifier trained on cross matched RRab and standard sources. The black star shows the location of the preferred cutoff score.

4.3 Template Fitting and Classification

4.3.1 Template Fitting

Once we had a much reduced group of objects showing RRL-like variability and color properties, we further assessed if they are convincing RRL by fitting an empirically-derived multiband RRab light curve template to their extinction-corrected light curves. This technique is particularly

Feature Name	Importance
$\chi^2_{\nu,grizY}$	0.1000
RoMS$_{grizY}$	0.0885
NAPD$_{90,grizY}$	0.0753
J_g	0.0738
$\chi^2_{\nu,g}$	0.0622
RoMS$_g$	0.0583
J_{grizY}	0.0540
NAPD$_{90,g}$	0.0454
RoMS$_z$	0.0312
J_r	0.0290

Table 4.2: Top ten features for initial variable selection. Features are ranked by their importance to the classification.

effective when applied to sparsely-sampled multiband light curves because it fits for only four independent parameters: the period *P*, phase ϕ, *g*-band amplitude A_g, and distance modulus μ, which allows them to be better constrained despite the small number of observations in the light curves. We refer the reader to Section 2 for a thorough discussion of this method.

For this analysis, we fit this template with some minor modifications from Section 3. Instead of fitting over a period range of 0.44 - 0.89 days, which revealed itself to be too restrictive in Section 3, we fit over a range of 0.2 - 1 day. The fitting time for each light curve was $\sim$2 - 6 min, depending on the CPU load at the time of processing. Like in Section 3, the top three best-fitting periods, amplitudes, phases, distance moduli, and RSS per degree of freedom of their fits were kept.

4.3.2 Classification

Even though we dramatically decreased the number of objects to be considered in the template fitting, there are still too many to inspect individually, so we trained another random forest classifier to select potential RRL based on the template fitting results. For the features, we combined the variability metrics from §4.2.4 with the RSS, periods, amplitudes, and phases from the top three best template fits. Like in Section 3, we also calculate the distances of each set of periods and amplitudes to the scaled Oosterhoff relations originally parameterized by Fabrizio et al. (2019)

and scaled by Vivas et al. (2019) (see their Figure 7). Only RRab with periods correctly estimated in one of the top three template fits and standard stars outside regions of high source density where cross-matching confusion was a concern were used to train the classifier. This left a training set composed of 4987 RRab and an equal number of standard sources.

The cutoff classifier score was selected using the Youden (1950) index, given by:

$$Y = \text{recall} + \text{specificity} - 1 \tag{4.11}$$

where the recall refers to the completeness of the RRab and the specificity refers to the completeness for the non-RRab. This metric effectively balances both purity and completeness. The maximum depth, number of trees, and number of features used in each split were chosen in a similar manner to the first classifier, but instead of F_β, the Youden index was used to determine the best set of hyperparameters.

We chose the optimal score cutoff at 0.315 where Youden's index for the training set was maximized. This classifier successfully identified 99.22% of the input RRab with correct periods with a purity of 93.28% (though we caution this purity is likely too optimistic as we did not have examples of all possible object types in the full data set). The performance curves and top features are shown in Figure 4.5 and Table 4.3, respectively. We discuss the recovery fraction for a broader range of RRL distances in §4.5.

4.4 Results

Although 9367 objects passed the classifier, it was clear from visual inspection of their positions that many objects with fewer observations near the edges of the footprint were passing the score threshold due to their low RSS values. To remove these objects without discarding very distant objects which also had few observations, we removed any objects which were located in regions of the footprint which were observed fewer than 20 times in $griz$. This effectively removed objects in regions near bright masked stars and the edges of the footprint and resulted in 8318 objects in the preliminary catalog.

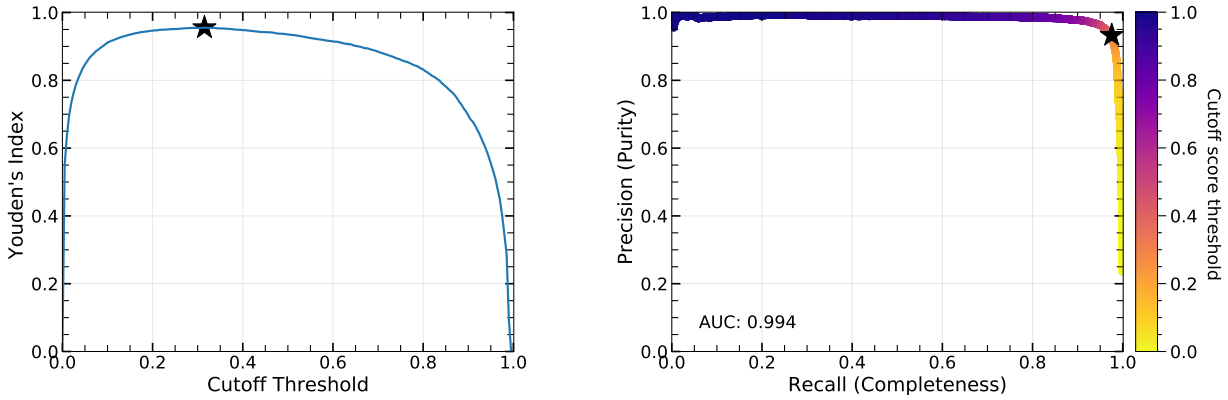

Figure 4.5: Performance curves from the second-stage classifier. *Left:* Youden's index over all possible cutoff score choices. The black star denotes where Youden's index is maximized at a value of 0.315. *Right:* ROC curve of the RF classifier trained on cross matched RRab and standard sources. The black star shows the location of the preferred cutoff score.

Feature Name	Importance
$\text{rss}_{\nu,0}$	0.1628
D(Oo-int)_0	0.0814
$\chi^2_{\nu,\ grizY}$	0.0716
J_g	0.0574
D(Oo-II)_0	0.0548
RoMS_{grizY}	0.0444
D(Oo-int)_2	0.0411
$\chi^2_{\nu,g}$	0.0386
D(Oo-int)_0	0.0302
$\text{NAPD}_{90,\ grizY}$	0.0300

Table 4.3: Top ten features for candidate selection. Features are ranked by their importance to the classification.

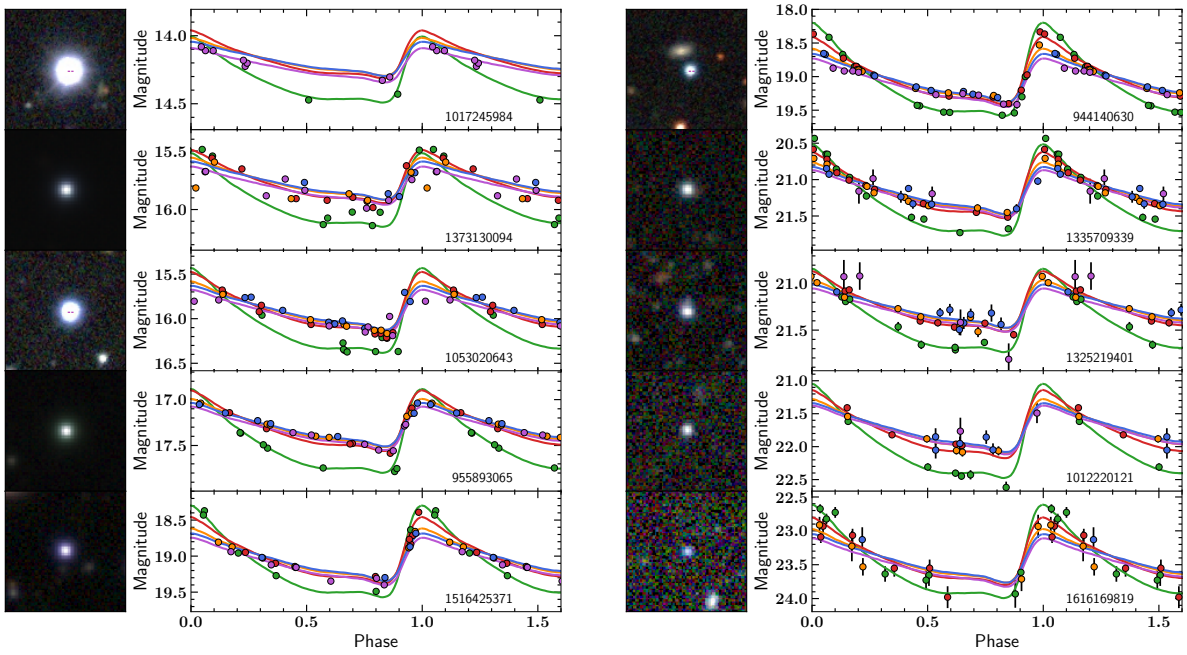

Figure 4.6: Random sample of RRab candidates over the full magnitude range of our catalog. Light curves are arranged vertically by increasing magnitude. If not visible, photometric errors are smaller than the plotting symbols.

Since the star-galaxy separation dramatically decreases in accuracy as observations become fainter, we visually inspected any candidates which had not already been identified as an RRab in an external survey. During this visual inspection, we removed any obvious extended non-stellar sources, bright oversaturated objects, objects with aliased periods, and extremely poor-fitting light curves. The end result was a sample of 6522 objects, 1075 of which are located beyond 120 kpc and do not have a previous label from another survey. We show a random selection of light curves over the full magnitude range of our sample in Figure 4.6. The equatorial positions of the resulting RRab catalog are shown in Figures 4.7, while the radial heliocentric distances are shown in Figure 4.8. The RRab candidates which were previously identified in selected external surveys are shown in Figure 3.10. Although these candidates have passed an visual inspection, they still need additional observations to confirm if they are true RRL, especially objects with very sparsely sampled light curves and very distant objects beyond 200 kpc. Table A.1 shows the first few entries of the full catalog of visually-accepted and previously-identified RRab, which will be presented in

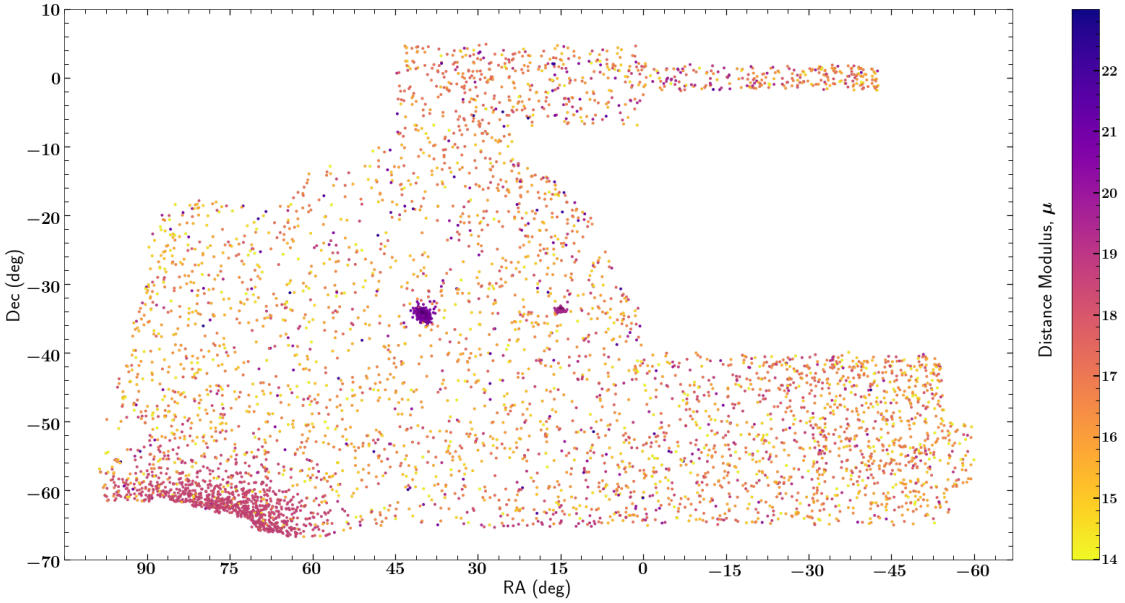

Figure 4.7: Positions of the DES Y6 RRab candidates after all classification stages and visual inspection, colored by distance modulus.

its entirety in Stringer et al. (in prep.).

4.5 Completeness for Faint Objects

Although we had externally identified RRab to use to train our classifiers to select RRab, we did not have any catalogs of RRL to use to verify our completeness efficiency at the faint end of our detection limits. Thus, to estimate our rate of detection at very faint magnitudes, we simulated a set of mock RRL light curves and classified them using our pipeline. This process largely mirrors the simulated light curves generated in Stringer et al. (2019); however, we provide a brief summary of the process below.

First, we constructed smoothed light curve shapes using the best-fitting templates and observational parameters for each of the 483 RRL (379 RRab, and 104 RRc) identified by Sesar et al. (2010, hereafter S10) and converted their magnitudes into the DES filter system[1]. We then shifted these light curves to their absolute magnitudes by subtracting the estimated distance moduli from

[1]The SDSS-DES filter transformation equations are available at `http://www.ctio.noao.edu/noao/node/5828#transformations`.

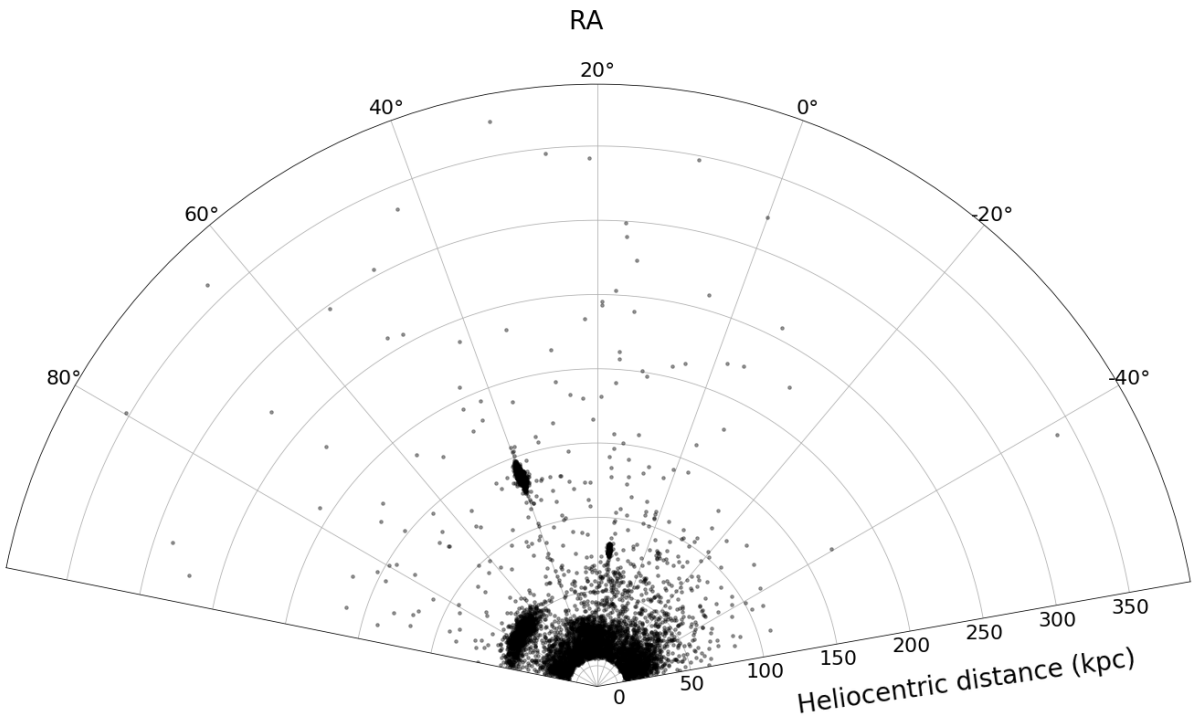

Figure 4.8: Radial distribution of the output RRL candidates from the second-stage classifier.

S10. For a set of magnitude bins ranging from $16 \leq g \leq 24$ with a bin width of 0.5, we shifted the light curve for each of the 483 light curve shapes to an average g magnitude randomly drawn from a uniform distribution within that magnitude bin. As each light curve was shifted to the random distance, any magnitudes within the light curve that fell beyond the Y6 single epoch limiting magnitudes were removed. We then assigned photometric uncertainties to each observation using the rescaled values from §4.1.1 and used them to introduce scatter into the observations. These light curves were then downsampled to a real DES observing cadence randomly drawn from bright stars across the footprint. The total simulated sample included 8211 light curves, of which 6443 were RRab and 1768 were RRc. We are not specifically searching for RRc in this work, but include their simulated curves to assess how often RRc are incorrectly identified as RRab in our classification process.

To assess the recovery of our template fitting and classification process, we subjected all of these light curves to the same minimum number of observations cut, color cuts, variability classi-

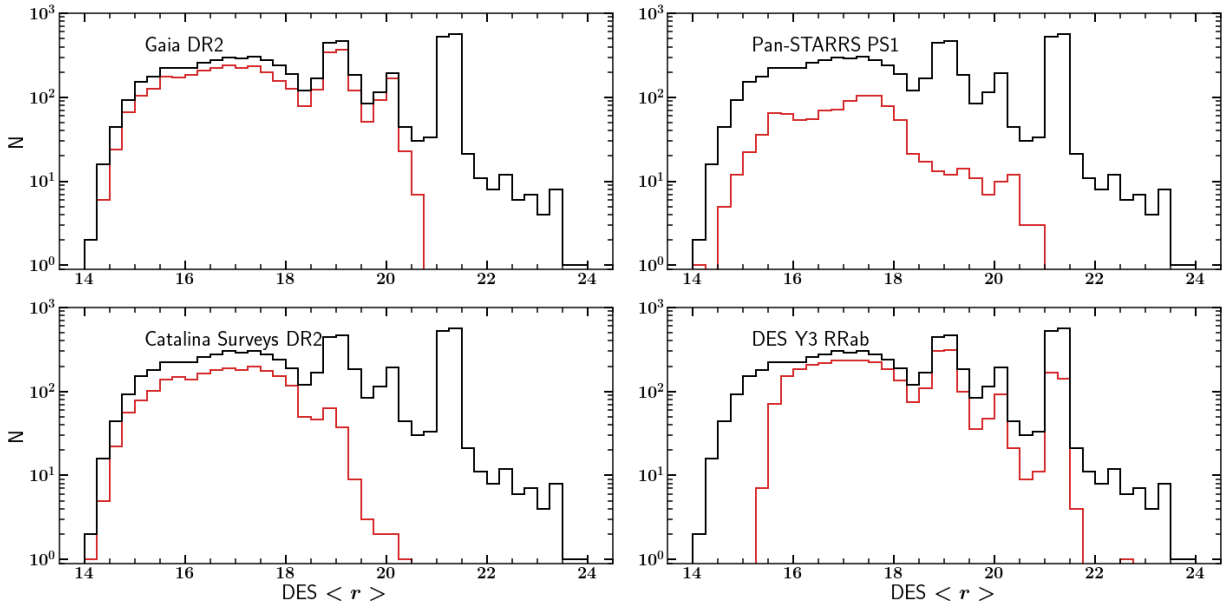

Figure 4.9: Overlap with external RRab catalogs. The distribution of this RRab catalog as a function of the extinction corrected average r magnitudes $\langle r \rangle$ are plotted in black. The distributions of previously identified RRab from external catalogs which were recovered in our catalog are plotted in red. *Bottom right:* We note that the combination of the increased number of observations, decreased S/N threshold, and alternative selection cuts in Y6 increased the depth of our catalog by ~ 1 magnitude, but also extended the detection range to brighter magnitudes as well.

fier, template fitting and final classifier which we applied to the real data. The recovery results and precision of parameter estimates are shown in Figure 4.10.

From these results, we see that our recovery fraction for RRab largely improves as the number of light curve observations increases, with the exception of a small increase for very low observation counts (it is easier to achieve template fits with low RSS to light curves with very few points.) The parameter estimation for both RRab and RRc from the template fitting performs better when there are more observations available to fit and small photometric errors on those observations. The trends in estimated periods and amplitudes from our simulated light curves reflect this and decline in precision with the increasing photometric errors at larger distances. The period accuracy for RRab approaches 100% when the light curve has ≥ 30 observations. The RRc recovery fraction is overall very low ($\leq 10\%$ for light curves with ≥ 25 observations and $< 20\%$ at all distances), which suggests that RRc are unlikely to contribute substantial contamination to our final catalog.

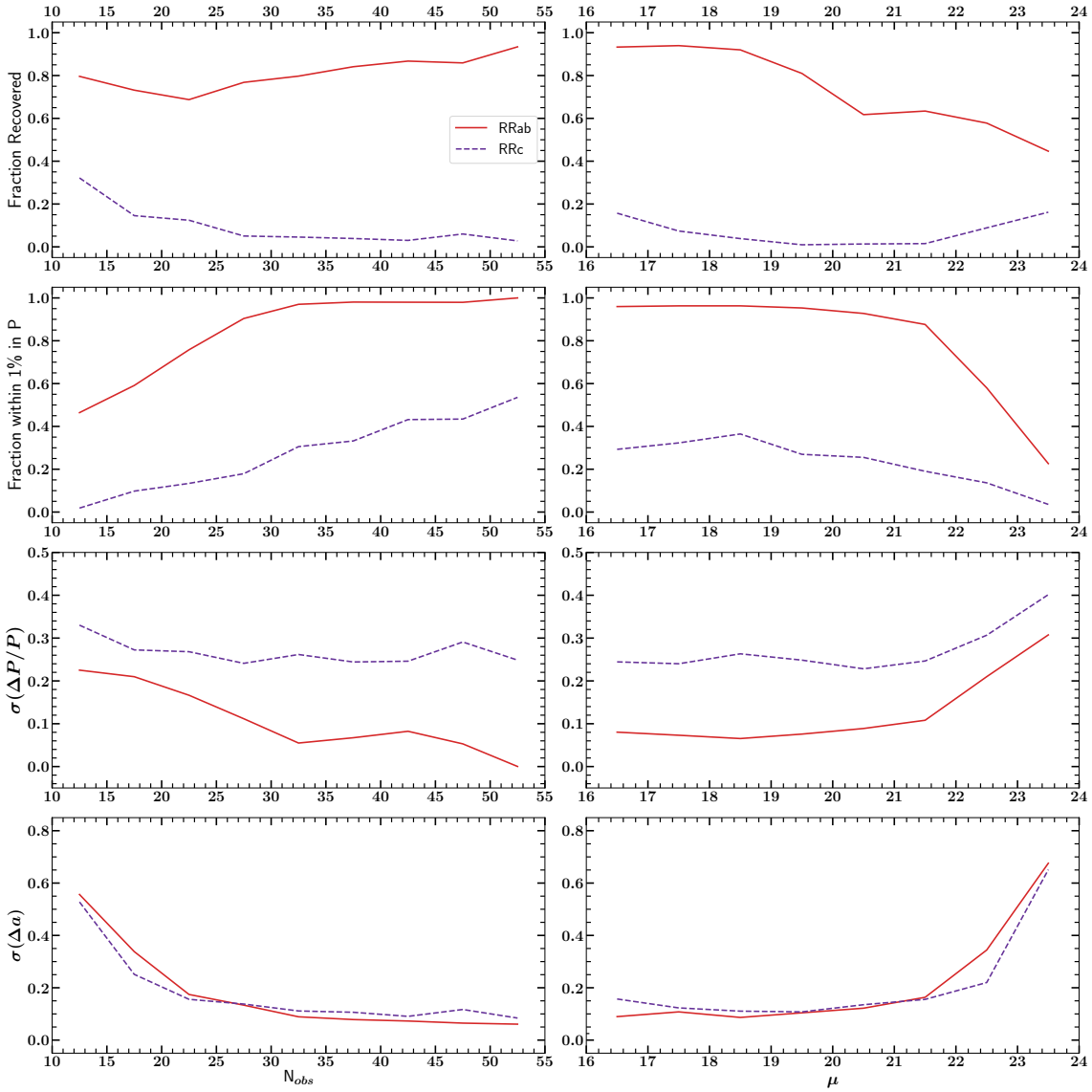

Figure 4.10: Recovery results from simulated RR Lyrae light curves. RRab results are plotted in red, while RRc are plotted in purple. All quantities in the left column are plotted as functions of the number of light curve observations, N_{obs}, while the right column shows these same quantities plotted as a function of distance modulus μ. Although we do not search for RRc in this work, we plot these values to assess how likely they are to contaminate our sample. The quantities shown are as follows. *First row:* Fraction of simulated curves identified as RRab by the full classification pipeline. The bump in RRab recovery near $\mu \sim 20.5$ roughly aligns with the rapid decrease of the RRab density in the training set after $g \sim 20$, shown in Figure 4.3. *Second row:* Fraction of periods correctly estimated within 1% of their input values. Period accuracy approaches 100% near $N_{obs} \geq 30$ and rapidly decreases after $\mu \sim 21$. *Third row:* Standard deviation of period estimate precision. *Bottom row:* Standard deviation of amplitude estimate precision. We see a degradation in precision for light curves with $N_{obs} \leq 30$ and $\mu \geq 21$, similar to that of the period estimates.

The RRab recovery fraction largely decreases as the distance increases, with a bump occurring near $\mu \sim 19.5$, which can largely be attributed to the lack of RRab in the training set for distances beyond this value (see Figure 4.3). While it is difficult to examine the individual classification decisions made by the ensemble of decision trees in our Random Forests, we postulate multiple reasons to explain this unexpected behavior and its dependence on magnitude. First, the number of objects in the training set increased dramatically within the magnitude range of $19 \leq g \leq 22$, with the number of non-varying sources significantly outnumbering the RRab sources after $g \sim 19.5$. To account for this change in the fraction of RRab to non-RRab in this magnitude range, the classifier may have implemented harsher cuts to keep the purity high. This begets the question of how the classifier knew the approximate magnitudes of the objects since there there are no features which directly encode the magnitudes or distances of the objects. In our feature list, we included both photometric error-weighted and unweighted statistics, so it is possible that the machine learning model could have still "learned" the magnitudes of the individual objects because: a) the values of the weighted variability statistics generally decrease with increasing distance because the light curve observations become noisier, b) the unweighted statistics would remain high at greater distances despite the increased noise, and c) fainter objects are more likely to contain imputed values for some of these features as their observations exceed the limiting magnitudes for the redder bands.

Additionally, the training set of known RR Lyrae and standard sources ends at a depth where the DES Y6 data is still well-sampled with a sufficiently high S/N such that an object's variability is easily detectable. Thus, when the training set abruptly ends near $\mu = 20.5$, the classifier is effectively doing very little because it did not learn the variability patterns to separate fainter objects. Despite this, however, our rate of recovery for RRab even at large distances ($\geq 60\%$ for $\mu \leq 22.5$) is sufficient to search for potentially unknown stellar structures, which we discuss in the following section.

4.6 A Preliminary Satellite Search

Groups of RRL are very effective at tracing stellar structures which can evade detection by other methods. Using our RRab catalog and derived recovery curves, we aim to estimate the background (halo) level of RR Lyrae for the full range of distances in our catalog for various half-light radii $r_{1/2}$ and then search for outliers to discover possible new stellar overdensities.

To begin our search, we define our satellite parameter space with a set of ten logarithmically-spaced (base = 10) half light radii, $r_{1/2}$, with values characteristic of dwarf satellite galaxies in the Milky Way ($10 \leq r_{1/2} \leq 2000$ pc). For each of these $r_{1/2}$, we created a sequence of distances with 3 $r_{1/2}$ spacing across the entire distance range of our RRab catalog. For each of these radii and distances, we sampled the DES footprint with a grid of (RA, Dec) positions with angular spacing corresponding to 3 $r_{1/2}$ projected at that distance. For each of these locations, we counted the number of catalog RRab present within a cylinder of length $6\ r_{1/2}$+$6\sigma_{\rm stat}$ and face area of $9\ r_{1/2}^2$ centered on the target location and distance.

To estimate the background level of RRab one would expect to find in a given satellite volume, we removed all RRab counts from regions within 5 $r_{1/2}$ of confirmed and candidate satellite galaxies. Then, we calculated the average count of RRab and its standard deviation for each $r_{1/2}$ and distance. These background RRab counts for each $r_{1/2}$ over the full distance range of our catalog, corrected for the recovery fraction derived from the simulated curves are shown in Figure 4.11. These results match the trends we expect: as the $r_{1/2}$ of the search region increases, so does the background level of RRab present within it. We also see a gradual decrease in the number of RRab at increasing distances, mimicking trends shown by RRL in other works (Hernitschek et al., 2018; Medina et al., 2018).

With our background RRab level recorded, we then searched for outliers in RRab counts over all ($r_{1/2}, d_h$). Any search cylinder containing a number of RRab at least 5σ above the corresponding background RRab level was stored as a potential overdensity. We find that we recover known structures such as the LMC outskirts, the Sculptor dSph and the Fornax dSph with high significance, demonstrating that the method works. Regions which contain at least two RRab and are at least

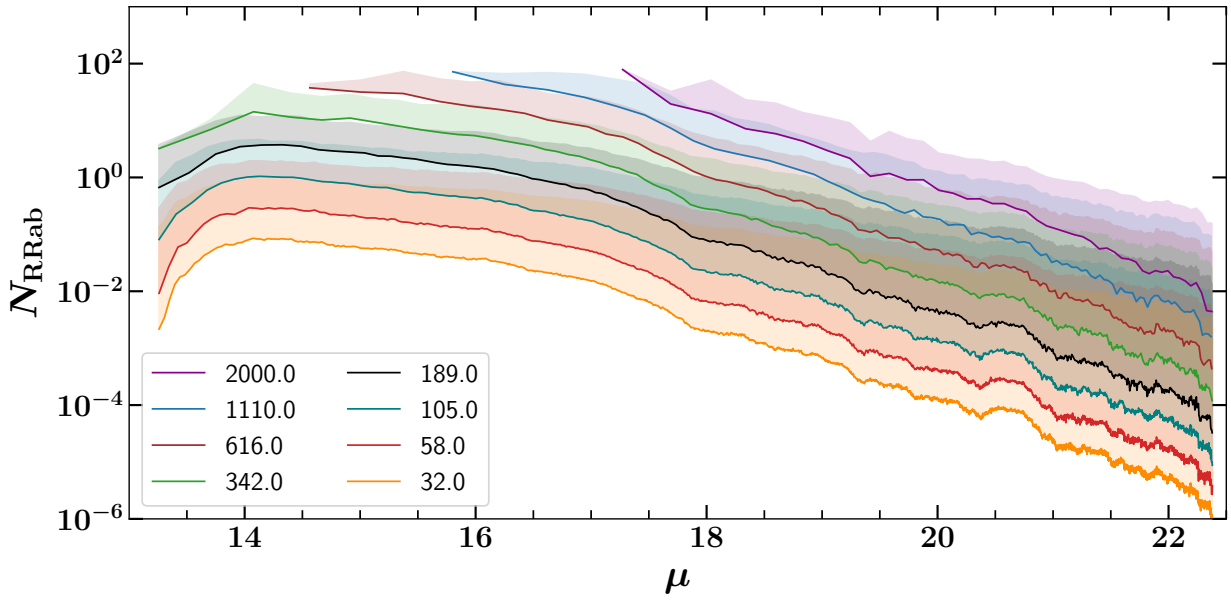

Figure 4.11: Distribution of background RRab expected for a given $r_{1/2}$ over the full range of RRab distances in our catalog, corrected for the recovery fraction as a function of μ. Each colored curve denotes the average number of catalog RRab found in volume cylinders corresponding to each $r_{1/2}$ after known structures were removed. The colored shaded regions show the 3σ confidence interval. $r_{1/2}$ listed in the legend are in pc.

5σ above the background RRab level for $r_{1/2} = 342$ pc are shown in Figure 4.12 in black translucent circles. Outlines of known satellites and streams are plotted in blue and red dots, respectively (Mateu et al., 2018). It is clear from this representation that numerous RRab overdensities overlap with known structures; although this method noticeably (and by design) does not perform well at tracing the entire lengths of streams. Any outlier regions which do not correspond to any known objects will need further study to determine if they trace real structures.

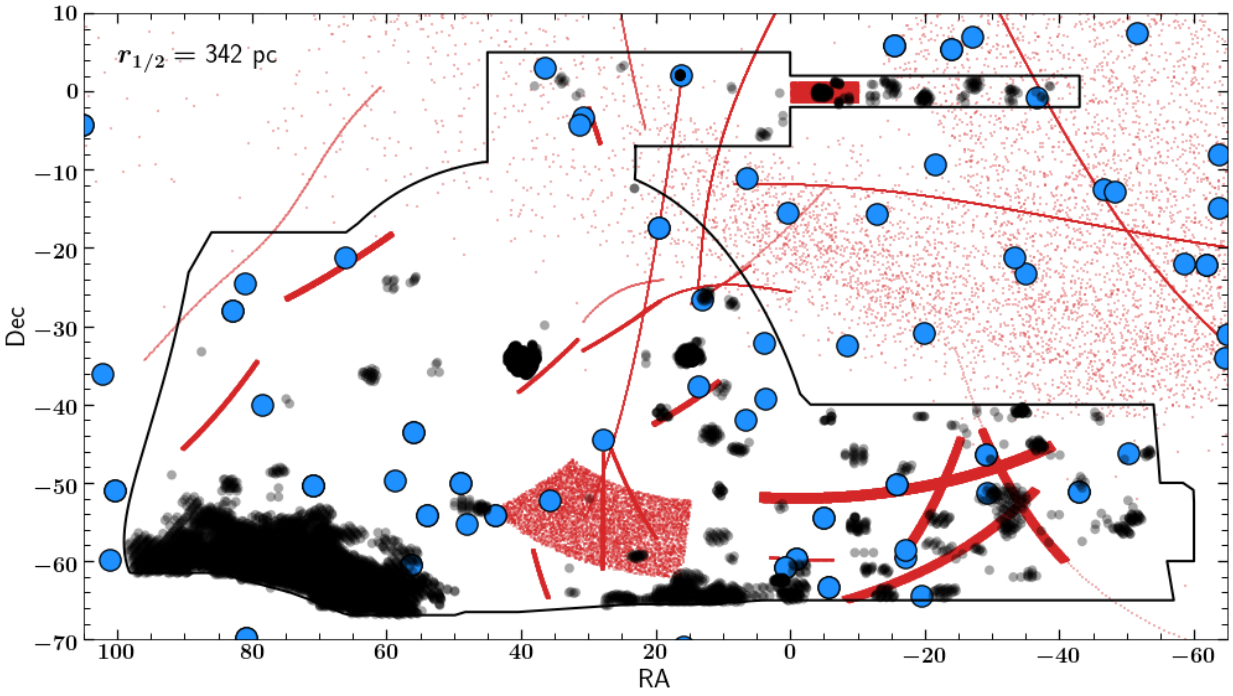

Figure 4.12: Positions of all regions with $\geq 5\sigma$ RRab counts for $r_{1/2} = 342$ pc, shown in black. Previously discovered confirmed and candidate satellite galaxies are shown with blue dots, while the footprints of known streams (Mateu et al., 2018) are shown in red. *Note:* point sizes have been increased for visibility and do not correspond to the physical sizes of these structures. The red points do not represent the locations of real stars and are only shown to demonstrate the projection of the stream footprints.

5. SUMMARY AND CONCLUSIONS*

Even though DES has concluded, there remains multiple opportunities to expand this work in the future. In this section, we discuss necessary followup and some potential modifications to the template fitting. Then, we specifically mention our method's applicability to the next generation wide field survey in the southern hemisphere, LSST. Finally, we summarize the work presented in this document.

5.1 Potential Extensions to This Work

5.1.1 Followup Observations

Although we identified RRab candidates to the best of our ability in the DES data set, candidates with very poorly sampled light curves and at large distancs (>200 kpc) require additional observations to confirm if they are truly RR Lyrae. This confirmation is especially crucial for determining if the overdensities of RRab we located within the DES Y6 data are truly stellar structures or simply chance alignments of contaminating sources. Furthermore, any candidate overdensities will need confirmation through deep imaging and spectroscopy, if available, to locate their Main Sequence Turnoffs and determine the velocity dispersions of their member stars.

5.1.2 DES *P-L-Z* Relation

In Stringer et al. (2019), we found excellent agreement (~ 0.06 mag) between the estimated distance moduli of Sesar et al. (2010) and our model estimates for the RRL in stripe 82. However, a large fraction of these RRL are nearby members of overdensities and thus have similar metallicity values. To estimate the effects of differing stellar metallicity ([Fe/H]) values on our distance estimates, we examined a cross-matched sample of RRL from the Catalina Real-Time Transient Survey (Torrealba et al., 2015, hereafter T15) which had photometric metallicity estimates. By comparing our distance estimates to those of T15, we discovered that our model's fixed metallicity

*Part of this section is reprinted with permission from Identification of RR Lyrae stars in multiband, sparsely-sampled data from the Dark Energy Survey using template fitting and Random Forest classification by Stringer, et al. 2019. *The Astronomical Journal*, 158, 1. Copyright 2019 by The American Astronomical Society.

affects our distance estimates substantially (see Figure 3.12).

Currently, there are no *P-L-Z* relations in DES $grizY$ available, but their derivation is underway (Vivas et al., in prep). Once such relations are derived, it would be trivial to substitute the model's current *P–L* relations with the derived *P-L-Z* relations. The inclusion of a metallicity term adds an additional parameter to the template, which would require prior knowledge of the RRL's metallicity or its own grid search with a corresponding increase in computation time. However, the accuracy of the model's distance estimates will be significantly improved with the inclusion of a *P-L-Z* relation. Additionally, knowing the true metallicity values for our model parameter estimates will allow us to place our distance estimates on a similar scale to those from other catalogs. Combining our RRL catalog with others will enable more complete studies of Milky Way substructures.

5.1.3 Searching for RRc

In our prior search for RRL in DES, we exclusively searched for RRab because their light curves have large amplitudes and a characteristic sawtooth shape that clearly distinguishes them from the light curves of other types of variable objects. We did not search for RRc because their smaller amplitudes and more sinusoidally-shaped light curves are more difficult to classify unambiguously, so their inclusion would likely allow more contamination into the sample. Unfortunately, by prioritizing purity over completeness in this way in our catalog, we likely excluded thousands of additional RRL which could be used to locate and characterize Milky Way substructures.

Using the same methods described in §3.4, one could derive a similar template for RRc. Searching for RRc with this template would require modifications to the frequency grid search to reflect values typical for RRc and careful identification of RRc candidates from the results. However, with adequate sampling, one has the potential to detect thousands more RRL for tracing Galactic structure. Not only would searching for RRc increase the census of known Galactic RRL, but would also shed additional light on the ratios of RRab to RRc in discrete stellar populations and in the Milky Way halo at greater distances.

5.2 Applicability to LSST

The upcoming successor to DES, the next-generation large ground-based Legacy Survey of Space and Time (LSST) (Ivezić et al., 2019) is set to begin full science operations with the Vera Rubin Telescope in early 2023[1]. The most current LSST "Baseline Cadence" for its Wide-Fast-Deep Survey (WFD), which covers 18,000 deg^2 of the sky and comprises $\sim$85% of its total allocated observing time, is to image each field twice 40 minutes apart once every three days in a different filter. After 10 years of operation, each field is expected to have a median of (62, 88, 199, 201, 180, 180) visits in $ugrizy$ with a single epoch depth of (23.14, 24.47, 24.16, 23.40, 22.23, 21.57) mag. Assuming these observations are spaced uniformly over 10 years, one can expect most light curves to have $\sim$80 multiband observations within the first year (Ivezić et al., 2019)[2].

Oluseyi et al. (2012) found from their analysis of simulated LSST data that reliable RRL period estimation will require several years of operation, however, several multiband techniques have been developed since their publication. For instance, VanderPlas and Ivezić (2015) estimated accurate periods 64% of the time on downsampled S10 light curves with $\sim$55 observations and Sesar et al. (2017) accurately estimated periods for 85% of their PS1 training set with $\sim$67 observations. Our simulations show that our template fitting method is capable of estimating the correct periods to within 1% for 95% of the light curves with 20 total observations. Thus, our algorithm would be effective to identify potential RRab candidates (which would need followup for confirmation) within the very first year of LSST operations. After the first year, the light curves in the WFD survey will be adequately sampled to use other multiband methods available in the literature to better characterize any candidates.

This upcoming survey is very timely and will most likely recover any remaining RRL within the MW stellar halo, finally determining once and for all if there are any missing satellite galaxies containing RRL.

[1] `https://www.lsst.org/about/timeline`

[2] See the most current version of the draft of the LSST Observing Strategy white paper located at `https://github.com/LSSTScienceCollaborations/ObservingStrategy`.

5.3 Summary

We have presented a new physically-motivated general multiband RRab template and a computationally efficient fitting procedure. We combined this method with random forest classifiers to create a powerful technique that can robustly identify these variables in sparse multiband data even when fewer than 20 observations are available. Despite the poor cadence and sampling of DES data, we detected 5783 RRab candidates in the first three years, and 6522 in the full data set to distances previously untouched by other ground-based large scale surveys. Using these candidates, we conducted a search for overdensities in the regions probed by DES and recovered previously known satellite galaxies and multiple stellar overdensities. We make the template, these catalogs, and the light curves of the RRab candidates and the training sample available to the scientific community for future studies. Our method is especially useful for other multiband data sets which were not specifically designed for time series analysis.

REFERENCES

T. M. C. Abbott, F. B. Abdalla, S. Allam, A. Amara, J. Annis, J. Asorey, S. Avila, O. Ballester, M. Banerji, W. Barkhouse, L. Baruah, M. Baumer, K. Bechtol, M. R. Becker, A. Benoit-Lévy, G. M. Bernstein, E. Bertin, J. Blazek, S. Bocquet, D. Brooks, D. Brout, E. Buckley-Geer, D. L. Burke, V. Busti, R. Campisano, L. Cardiel-Sas, A. Carnero Rosell, M. Carrasco Kind, J. Carretero, F. J. Castander, R. Cawthon, C. Chang, X. Chen, C. Conselice, G. Costa, M. Crocce, C. E. Cunha, C. B. D'Andrea, L. N. da Costa, R. Das, G. Daues, T. M. Davis, C. Davis, J. De Vicente, D. L. DePoy, J. DeRose, S. Desai, H. T. Diehl, J. P. Dietrich, S. Dodelson, P. Doel, A. Drlica-Wagner, T. F. Eifler, A. E. Elliott, A. E. Evrard, A. Farahi, A. Fausti Neto, E. Fernandez, D. A. Finley, B. Flaugher, R. J. Foley, P. Fosalba, D. N. Friedel, J. Frieman, J. García-Bellido, E. Gaztanaga, D. W. Gerdes, T. Giannantonio, M. S. S. Gill, K. Glazebrook, D. A. Goldstein, M. Gower, D. Gruen, R. A. Gruendl, J. Gschwend, R. R. Gupta, G. Gutierrez, S. Hamilton, W. G. Hartley, S. R. Hinton, J. M. Hislop, D. Hollowood, K. Honscheid, B. Hoyle, D. Huterer, B. Jain, D. J. James, T. Jeltema, M. W. G. Johnson, M. D. Johnson, T. Kacprzak, S. Kent, G. Khullar, M. Klein, A. Kovacs, A. M. G. Koziol, E. Krause, A. Kremin, R. Kron, K. Kuehn, S. Kuhlmann, N. Kuropatkin, O. Lahav, J. Lasker, T. S. Li, R. T. Li, A. R. Liddle, M. Lima, H. Lin, P. López-Reyes, N. MacCrann, M. A. G. Maia, J. D. Maloney, M. Manera, M. March, J. Marriner, J. L. Marshall, P. Martini, T. McClintock, T. McKay, R. G. McMahon, P. Melchior, F. Menanteau, C. J. Miller, R. Miquel, J. J. Mohr, E. Morganson, J. Mould, E. Neilsen, R. C. Nichol, F. Nogueira, B. Nord, P. Nugent, L. Nunes, R. L. C. Ogand o, L. Old, A. B. Pace, A. Palmese, F. Paz-Chinchón, H. V. Peiris, W. J. Percival, D. Petravick, A. A. Plazas, J. Poh, C. Pond, A. Porredon, A. Pujol, A. Refregier, K. Reil, P. M. Ricker, R. P. Rollins, A. K. Romer, A. Roodman, P. Rooney, A. J. Ross, E. S. Rykoff, M. Sako, M. L. Sanchez, E. Sanchez, B. Santiago, A. Saro, V. Scarpine, D. Scolnic, S. Serrano, I. Sevilla-Noarbe, E. Sheldon, N. Shipp, M. L. Silveira, M. Smith, R. C. Smith, J. A. Smith, M. Soares-Santos, F. Sobreira, J. Song, A. Stebbins, E. Suchyta, M. Sullivan, M. E. C. Swanson, G. Tarle, J. Thaler, D. Thomas, R. C. Thomas, M. A.

Troxel, D. L. Tucker, V. Vikram, A. K. Vivas, A. R. Walker, R. H. Wechsler, J. Weller, W. Wester, R. C. Wolf, H. Wu, B. Yanny, A. Zenteno, Y. Zhang, J. Zuntz, DES Collaboration, S. Juneau, M. Fitzpatrick, R. Nikutta, D. Nidever, K. Olsen, A. Scott, and NOAO Data Lab. The Dark Energy Survey: Data Release 1. *ApJS*, 239(2):18, Dec 2018. doi: 10.3847/1538-4365/aae9f0.

Y. Amit and D. Geman. Shape quantization and recognition with randomized trees. *Neural Computation*, 9(7):1545–1588, 1997. doi: 10.1162/neco.1997.9.7.1545. URL `https://doi.org/10.1162/neco.1997.9.7.1545`.

Astropy Collaboration, A. M. Price-Whelan, B. M. Sipőcz, H. M. Günther, P. L. Lim, S. M. Crawford, S. Conseil, D. L. Shupe, M. W. Craig, N. Dencheva, A. Ginsburg, J. T. Vand erPlas, L. D. Bradley, D. Pérez-Suárez, M. de Val-Borro, T. L. Aldcroft, K. L. Cruz, T. P. Robitaille, E. J. Tollerud, C. Ardelean, T. Babej, Y. P. Bach, M. Bachetti, A. V. Bakanov, S. P. Bamford, G. Barentsen, P. Barmby, A. Baumbach, K. L. Berry, F. Biscani, M. Boquien, K. A. Bostroem, L. G. Bouma, G. B. Brammer, E. M. Bray, H. Breytenbach, H. Buddelmeijer, D. J. Burke, G. Calderone, J. L. Cano Rodríguez, M. Cara, J. V. M. Cardoso, S. Cheedella, Y. Copin, L. Corrales, D. Crichton, D. D'Avella, C. Deil, É. Depagne, J. P. Dietrich, A. Donath, M. Droettboom, N. Earl, T. Erben, S. Fabbro, L. A. Ferreira, T. Finethy, R. T. Fox, L. H. Garrison, S. L. J. Gibbons, D. A. Goldstein, R. Gommers, J. P. Greco, P. Greenfield, A. M. Groener, F. Grollier, A. Hagen, P. Hirst, D. Homeier, A. J. Horton, G. Hosseinzadeh, L. Hu, J. S. Hunkeler, Ž. Ivezić, A. Jain, T. Jenness, G. Kanarek, S. Kendrew, N. S. Kern, W. E. Kerzendorf, A. Khvalko, J. King, D. Kirkby, A. M. Kulkarni, A. Kumar, A. Lee, D. Lenz, S. P. Littlefair, Z. Ma, D. M. Macleod, M. Mastropietro, C. McCully, S. Montagnac, B. M. Morris, M. Mueller, S. J. Mumford, D. Muna, N. A. Murphy, S. Nelson, G. H. Nguyen, J. P. Ninan, M. Nöthe, S. Ogaz, S. Oh, J. K. Parejko, N. Parley, S. Pascual, R. Patil, A. A. Patil, A. L. Plunkett, J. X. Prochaska, T. Rastogi, V. Reddy Janga, J. Sabater, P. Sakurikar, M. Seifert, L. E. Sherbert, H. Sherwood-Taylor, A. Y. Shih, J. Sick, M. T. Silbiger, S. Singanamalla, L. P. Singer, P. H. Sladen, K. A. Sooley, S. Sornarajah, O. Streicher, P. Teuben, S. W. Thomas, G. R. Tremblay, J. E. H. Turner, V. Terrón, M. H. van Kerkwijk, A. de la Vega, L. L. Watkins, B. A. Weaver, J. B.

Whitmore, J. Woillez, V. Zabalza, and Astropy Contributors. The Astropy Project: Building an Open-science Project and Status of the v2.0 Core Package. *AJ*, 156(3):123, Sep 2018. doi: 10.3847/1538-3881/aabc4f.

R. A. Baeza-Yates and B. Ribeiro-Neto. *Modern Information Retrieval*. Addison-Wesley Longman Publishing Co., Inc., Boston, MA, USA, 1999. ISBN 020139829X.

S. I. Bailey. A discussion of variable stars in the cluster ω Centauri. *Annals of Harvard College Observatory*, 38:1, Jan 1902.

M. Baker and B. Willman. Charting Unexplored Dwarf Galaxy Territory with RR Lyrae. *AJ*, 150 (5):160, Nov 2015. doi: 10.1088/0004-6256/150/5/160.

N. Baker and R. Kippenhahn. The Pulsations of Models of δ Cephei Stars. With 17 Figures in the Text. *Z. Astrophys.*, 54:114, Jan 1962.

E. Balbinot, B. Yanny, T. S. Li, B. Santiago, J. L. Marshall, D. A. Finley, A. Pieres, T. M. C. Abbott, F. B. Abdalla, S. Allam, A. Benoit-Lévy, G. M. Bernstein, E. Bertin, D. Brooks, D. L. Burke, A. Carnero Rosell, M. Carrasco Kind, J. Carretero, C. E. Cunha, L. N. da Costa, D. L. DePoy, S. Desai, H. T. Diehl, P. Doel, J. Estrada, B. Flaugher, J. Frieman, D. W. Gerdes, D. Gruen, R. A. Gruendl, K. Honscheid, D. J. James, K. Kuehn, N. Kuropatkin, O. Lahav, M. March, P. Martini, R. Miquel, R. C. Nichol, R. Ogando, A. K. Romer, E. Sanchez, M. Schubnell, I. Sevilla-Noarbe, R. C. Smith, M. Soares-Santos, F. Sobreira, E. Suchyta, G. Tarle, D. Thomas, D. Tucker, A. R. Walker, and DES Collaboration. The Phoenix Stream: A Cold Stream in the Southern Hemisphere. *ApJ*, 820(1):58, Mar 2016. doi: 10.3847/0004-637X/820/1/58.

K. Bechtol, A. Drlica-Wagner, E. Balbinot, A. Pieres, J. D. Simon, B. Yanny, B. Santiago, R. H. Wechsler, J. Frieman, A. R. Walker, P. Williams, E. Rozo, E. S. Rykoff, A. Queiroz, E. Luque, A. Benoit-Lévy, D. Tucker, I. Sevilla, R. A. Gruendl, L. N. da Costa, A. Fausti Neto, M. A. G. Maia, T. Abbott, S. Allam, R. Armstrong, A. H. Bauer, G. M. Bernstein, R. A. Bernstein, E. Bertin, D. Brooks, E. Buckley-Geer, D. L. Burke, A. Carnero Rosell, F. J. Castander, R. Covarrubias, C. B. D'Andrea, D. L. DePoy, S. Desai, H. T. Diehl, T. F. Eifler, J. Estrada, A. E. Evrard, E. Fernandez, D. A. Finley, B. Flaugher, E. Gaztanaga, D. Gerdes, L. Girardi, M. Glad-

ders, D. Gruen, G. Gutierrez, J. Hao, K. Honscheid, B. Jain, D. James, S. Kent, R. Kron, K. Kuehn, N. Kuropatkin, O. Lahav, T. S. Li, H. Lin, M. Makler, M. March, J. Marshall, P. Martini, K. W. Merritt, C. Miller, R. Miquel, J. Mohr, E. Neilsen, R. Nichol, B. Nord, R. Ogando, J. Peoples, D. Petravick, A. A. Plazas, A. K. Romer, A. Roodman, M. Sako, E. Sanchez, V. Scarpine, M. Schubnell, R. C. Smith, M. Soares-Santos, F. Sobreira, E. Suchyta, M. E. C. Swanson, G. Tarle, J. Thaler, D. Thomas, W. Wester, J. Zuntz, and DES Collaboration. Eight New Milky Way Companions Discovered in First-year Dark Energy Survey Data. *ApJ*, 807(1): 50, Jul 2015. doi: 10.1088/0004-637X/807/1/50.

V. Belokurov, D. B. Zucker, N. W. Evans, G. Gilmore, S. Vidrih, D. M. Bramich, H. J. Newberg, R. F. G. Wyse, M. J. Irwin, M. Fellhauer, P. C. Hewett, N. A. Walton, M. I. Wilkinson, N. Cole, B. Yanny, C. M. Rockosi, T. C. Beers, E. F. Bell, J. Brinkmann, Ž. Ivezić, and R. Lupton. The Field of Streams: Sagittarius and Its Siblings. *ApJL*, 642(2):L137–L140, May 2006a. doi: 10.1086/504797.

V. Belokurov, D. B. Zucker, N. W. Evans, M. I. Wilkinson, M. J. Irwin, S. Hodgkin, D. M. Bramich, J. M. Irwin, G. Gilmore, B. Willman, S. Vidrih, H. J. Newberg, R. F. G. Wyse, M. Fellhauer, P. C. Hewett, N. Cole, E. F. Bell, T. C. Beers, C. M. Rockosi, B. Yanny, E. K. Grebel, D. P. Schneider, R. Lupton, J. C. Barentine, H. Brewington, J. Brinkmann, M. Harvanek, S. J. Kleinman, J. Krzesinski, D. Long, A. Nitta, J. A. Smith, and S. A. Snedden. A Faint New Milky Way Satellite in Bootes. *ApJL*, 647(2):L111–L114, Aug 2006b. doi: 10.1086/507324.

V. Belokurov, N. W. Evans, E. F. Bell, M. J. Irwin, P. C. Hewett, S. Koposov, C. M. Rockosi, G. Gilmore, D. B. Zucker, M. Fellhauer, M. I. Wilkinson, D. M. Bramich, S. Vidrih, H. W. Rix, T. C. Beers, D. P. Schneider, J. C. Barentine, H. Brewington, J. Brinkmann, M. Harvanek, J. Krzesinski, D. Long, K. Pan, S. A. Snedden, O. Malanushenko, and V. Malanushenko. The Hercules-Aquila Cloud. *ApJL*, 657(2):L89–L92, Mar 2007a. doi: 10.1086/513144.

V. Belokurov, D. B. Zucker, N. W. Evans, J. T. Kleyna, S. Koposov, S. T. Hodgkin, M. J. Irwin, G. Gilmore, M. I. Wilkinson, M. Fellhauer, D. M. Bramich, P. C. Hewett, S. Vidrih, J. T. A. De Jong, J. A. Smith, H. W. Rix, E. F. Bell, R. F. G. Wyse, H. J. Newberg, P. A. Mayeur, B. Yanny,

C. M. Rockosi, O. Y. Gnedin, D. P. Schneider, T. C. Beers, J. C. Barentine, H. Brewington, J. Brinkmann, M. Harvanek, S. J. Kleinman, J. Krzesinski, D. Long, A. Nitta, and S. A. Snedden. Cats and Dogs, Hair and a Hero: A Quintet of New Milky Way Companions. *ApJ*, 654(2):897–906, Jan 2007b. doi: 10.1086/509718.

V. Belokurov, M. G. Walker, N. W. Evans, D. C. Faria, G. Gilmore, M. J. Irwin, S. Koposov, M. Mateo, E. Olszewski, and D. B. Zucker. Leo V: A Companion of a Companion of the Milky Way Galaxy? *ApJL*, 686(2):L83, Oct 2008. doi: 10.1086/592962.

V. Belokurov, M. G. Walker, N. W. Evans, G. Gilmore, M. J. Irwin, M. Mateo, L. Mayer, E. Olszewski, J. Bechtold, and T. Pickering. The discovery of Segue 2: a prototype of the population of satellites of satellites. *MNRAS*, 397(4):1748–1755, Aug 2009. doi: 10.1111/j.1365-2966.2009.15106.x.

V. Belokurov, M. G. Walker, N. W. Evans, G. Gilmore, M. J. Irwin, D. Just, S. Koposov, M. Mateo, E. Olszewski, L. Watkins, and L. Wyrzykowski. Big Fish, Little Fish: Two New Ultra-faint Satellites of the Milky Way. *ApJL*, 712(1):L103–L106, Mar 2010. doi: 10.1088/2041-8205/712/1/L103.

V. Belokurov, A. J. Deason, S. E. Koposov, M. Catelan, D. Erkal, A. J. Drake, and N. W. Evans. Unmixing the Galactic halo with RR Lyrae tagging. *MNRAS*, 477(2):1472–1483, Jun 2018a. doi: 10.1093/mnras/sty615.

V. Belokurov, D. Erkal, N. W. Evans, S. E. Koposov, and A. J. Deason. Co-formation of the disc and the stellar halo. *MNRAS*, 478(1):611–619, Jul 2018b. doi: 10.1093/mnras/sty982.

M. Bergemann, B. Sesar, J. G. Cohen, A. M. Serenelli, A. Sheffield, T. S. Li, L. Casagrande, K. V. Johnston, C. F. P. Laporte, A. M. Price-Whelan, R. Schönrich, and A. Gould. Two chemically similar stellar overdensities on opposite sides of the plane of the Galactic disk. *Nature*, 555(7696):334–337, Mar 2018. doi: 10.1038/nature25490.

E. J. Bernard, A. M. N. Ferguson, E. F. Schlafly, M. Abbas, E. F. Bell, N. R. Deacon, N. F. Martin, H. W. Rix, B. Sesar, C. T. Slater, J. Penarrubia, R. F. G. Wyse, W. S. Burgett, K. C. Chambers, P. W. Draper, K. W. Hodapp, N. Kaiser, R. P. Kudritzki, E. A. Magnier, N. Metcalfe, J. S.

Morgan, P. A. Price, J. L. Tonry, R. J. Wainscoat, and C. Waters. Serendipitous discovery of a thin stellar stream near the Galactic bulge in the Pan-STARRS1 3π Survey. *MNRAS*, 443: L84–L88, Sep 2014. doi: 10.1093/mnrasl/slu089.

E. J. Bernard, A. M. N. Ferguson, E. F. Schlafly, N. F. Martin, H.-W. Rix, E. F. Bell, D. P. Finkbeiner, B. Goldman, D. Martínez-Delgado, B. Sesar, R. F. G. Wyse, W. S. Burgett, K. C. Chambers, P. W. Draper, K. W. Hodapp, N. Kaiser, R.-P. Kudritzki, E. A. Magnier, N. Metcalfe, R. J. Wainscoat, and C. Waters. A Synoptic Map of Halo Substructures from the Pan-STARRS1 3π Survey. *MNRAS*, 463(2):1759–1768, Dec 2016. doi: 10.1093/mnras/stw2134.

D. Bersier and P. R. Wood. Variable Stars in the Fornax Dwarf Galaxy. *AJ*, 123(2):840–847, Feb 2002. doi: 10.1086/338315.

E. Bertin and S. Arnouts. SExtractor: Software for source extraction. *A&As*, 117:393–404, Jun 1996. doi: 10.1051/aas:1996164.

S. Blažko. Mitteilung über veränderliche Sterne. *Astronomische Nachrichten*, 175:325, Aug 1907. doi: 10.1002/asna.19071752002.

E. Boettcher, B. Willman, R. Fadely, J. Strader, M. Baker, E. Hopkins, T. Tasnim Ananna, E. C. Cunningham, T. Douglas, J. Gilbert, A. Preston, and A. P. Sturner. A Search for RR Lyrae Stars in Segue 2 and Segue 3. *AJ*, 146(4):94, Oct 2013. doi: 10.1088/0004-6256/146/4/94.

G. Bono, M. Dall'Ora, F. Caputo, G. Coppola, K. Genovali, M. Marconi, A. M. Piersimoni, and R. F. Stellingwerf. RR Lyrae the Stellar Beacons of the Galactic Structure. In A. McWilliam, editor, *RR Lyrae Stars, Metal-Poor Stars, and the Galaxy*, volume 5, page 1, Aug 2011.

G. Bono, V. F. Braga, A. Pietrinferni, D. Magurno, M. Dall'Ora, G. Fiorentino, K. Fukue, L. Inno, M. Marengo, M. Bergemann, R. Buonanno, R. da Silva, M. Fabrizio, I. Ferraro, R. Gilmozzi, G. Iannicola, W. Kausch, N. Kobayashi, V. Kovtyukh, B. Lemasle, M. Marconi, S. Marinoni, P. M. Marrese, C. E. Martínez-Vázquez, N. Matsunaga, M. Monelli, J. Neeley, M. Nonino, B. Proxauf, N. Przybilla, M. Romaniello, M. Salaris, C. Sneden, P. B. Stetson, F. Thévenin, T. Tsujimoto, M. Urbaneja, E. Valenti, and M. Zoccali. Classical Cepheids and RR Lyrae stars: similar, but not too much. *MmSAI*, 87:358, Jan 2016.

L. Breiman. Random forests. *Machine Learning*, 45(1):532, 2001. doi: 10.1023/a:1010933404324.

J. S. Bullock and K. V. Johnston. Tracing Galaxy Formation with Stellar Halos. I. Methods. *ApJ*, 635(2):931–949, Dec 2005. doi: 10.1086/497422.

D. L. Burke, E. S. Rykoff, S. Allam, J. Annis, K. Bechtol, G. M. Bernstein, A. Drlica-Wagner, D. A. Finley, R. A. Gruendl, D. J. James, S. Kent, R. Kessler, S. Kuhlmann, J. Lasker, T. S. Li, D. Scolnic, J. Smith, D. L. Tucker, W. Wester, B. Yanny, T. M. C. Abbott, F. B. Abdalla, A. Benoit-Lévy, E. Bertin, A. Carnero Rosell, M. Carrasco Kind, J. Carretero, C. E. Cunha, C. B. D'Andrea, L. N. da Costa, S. Desai, H. T. Diehl, P. Doel, J. Estrada, J. García-Bellido, D. Gruen, G. Gutierrez, K. Honscheid, K. Kuehn, N. Kuropatkin, M. A. G. Maia, M. March, J. L. Marshall, P. Melchior, F. Menanteau, R. Miquel, A. A. Plazas, M. Sako, E. Sanchez, V. Scarpine, R. Schindler, I. Sevilla-Noarbe, M. Smith, R. C. Smith, M. Soares-Santos, F. Sobreira, E. Suchyta, G. Tarle, A. R. Walker, and DES Collaboration. Forward Global Photometric Calibration of the Dark Energy Survey. *AJ*, 155(1):41, Jan 2018. doi: 10.3847/1538-3881/aa9f22.

C. Cacciari and G. Clementini. *Globular Cluster Distances from RR Lyrae Stars*, volume 635, pages 105–122. 2003. doi: 10.1007/978-3-540-39882-0_6.

C. Cáceres and M. Catelan. The Period-Luminosity Relation of RR Lyrae Stars in the SDSS Photometric System. *ApJS*, 179(1):242–248, Nov 2008. doi: 10.1086/591231.

M. Catelan. Horizontal branch stars: the interplay between observations and theory, and insights into the formation of the Galaxy. *ApSS*, 320:261–309, Apr 2009. doi: 10.1007/s10509-009-9987-8.

M. Catelan and H. A. Smith. *Pulsating Stars*. 2015.

M. Catelan, B. J. Pritzl, and H. A. Smith. The RR Lyrae Period-Luminosity Relation. I. Theoretical Calibration. *ApJS*, 154(2):633–649, Oct 2004. doi: 10.1086/422916.

K. C. Chambers, E. A. Magnier, N. Metcalfe, H. A. Flewelling, M. E. Huber, C. Z. Waters, L. Denneau, P. W. Draper, D. Farrow, D. P. Finkbeiner, C. Holmberg, J. Koppenhoefer, P. A. Price,

A. Rest, R. P. Saglia, E. F. Schlafly, S. J. Smartt, W. Sweeney, R. J. Wainscoat, W. S. Burgett, S. Chastel, T. Grav, J. N. Heasley, K. W. Hodapp, R. Jedicke, N. Kaiser, R. P. Kudritzki, G. A. Luppino, R. H. Lupton, D. G. Monet, J. S. Morgan, P. M. Onaka, B. Shiao, C. W. Stubbs, J. L. Tonry, R. White, E. Bañados, E. F. Bell, R. Bender, E. J. Bernard, M. Boegner, F. Boffi, M. T. Botticella, A. Calamida, S. Casertano, W. P. Chen, X. Chen, S. Cole, N. Deacon, C. Frenk, A. Fitzsimmons, S. Gezari, V. Gibbs, C. Goessl, T. Goggia, R. Gourgue, B. Goldman, P. Grant, E. K. Grebel, N. C. Hambly, G. Hasinger, A. F. Heavens, T. M. Heckman, R. Henderson, T. Henning, M. Holman, U. Hopp, W. H. Ip, S. Isani, M. Jackson, C. D. Keyes, A. M. Koekemoer, R. Kotak, D. Le, D. Liska, K. S. Long, J. R. Lucey, M. Liu, N. F. Martin, G. Masci, B. McLean, E. Mindel, P. Misra, E. Morganson, D. N. A. Murphy, A. Obaika, G. Narayan, M. A. Nieto-Santisteban, P. Norberg, J. A. Peacock, E. A. Pier, M. Postman, N. Primak, C. Rae, A. Rai, A. Riess, A. Riffeser, H. W. Rix, S. Röser, R. Russel, L. Rutz, E. Schilbach, A. S. B. Schultz, D. Scolnic, L. Strolger, A. Szalay, S. Seitz, E. Small, K. W. Smith, D. R. Soderblom, P. Taylor, R. Thomson, A. N. Taylor, A. R. Thakar, J. Thiel, D. Thilker, D. Unger, Y. Urata, J. Valenti, J. Wagner, T. Walder, F. Walter, S. P. Watters, S. Werner, W. M. Wood-Vasey, and R. Wyse. The Pan-STARRS1 Surveys. *arXiv e-prints*, art. arXiv:1612.05560, Dec 2016.

G. Clementini, R. Gratton, A. Bragaglia, E. Carretta, L. Di Fabrizio, and M. Maio. Distance to the Large Magellanic Cloud: The RR Lyrae Stars. *AJ*, 125(3):1309–1329, Mar 2003. doi: 10.1086/367773.

G. Clementini, V. Ripepi, R. Molinaro, A. Garofalo, T. Muraveva, L. Rimoldini, L. P. Guy, G. Jevardat de Fombelle, K. Nienartowicz, O. Marchal, M. Audard, B. Holl, S. Leccia, M. Marconi, I. Musella, N. Mowlavi, I. Lecoeur-Taibi, L. Eyer, J. De Ridder, S. Regibo, L. M. Sarro, L. Szabados, D. W. Evans, and M. Riello. Gaia Data Release 2. Specific characterisation and validation of all-sky Cepheids and RR Lyrae stars. *A&A*, 622:A60, Feb 2019. doi: 10.1051/0004-6361/201833374.

Dark Energy Survey Collaboration, T. Abbott, F. B. Abdalla, J. Aleksić, S. Allam, A. Amara, D. Bacon, E. Balbinot, M. Banerji, K. Bechtol, A. Benoit-Lévy, G. M. Bernstein, E. Bertin,

J. Blazek, C. Bonnett, S. Bridle, D. Brooks, R. J. Brunner, E. Buckley-Geer, D. L. Burke, G. B. Caminha, D. Capozzi, J. Carlsen, A. Carnero-Rosell, M. Carollo, M. Carrasco-Kind, J. Carretero, F. J. Castander, L. Clerkin, T. Collett, C. Conselice, M. Crocce, C. E. Cunha, C. B. D'Andrea, L. N. da Costa, T. M. Davis, S. Desai, H. T. Diehl, J. P. Dietrich, S. Dodelson, P. Doel, A. Drlica-Wagner, J. Estrada, J. Etherington, A. E. Evrard, J. Fabbri, D. A. Finley, B. Flaugher, R. J. Foley, P. Fosalba, J. Frieman, J. García-Bellido, E. Gaztanaga, D. W. Gerdes, T. Giannantonio, D. A. Goldstein, D. Gruen, R. A. Gruendl, P. Guarnieri, G. Gutierrez, W. Hartley, K. Honscheid, B. Jain, D. J. James, T. Jeltema, S. Jouvel, R. Kessler, A. King, D. Kirk, R. Kron, K. Kuehn, N. Kuropatkin, O. Lahav, T. S. Li, M. Lima, H. Lin, M. A. G. Maia, M. Makler, M. Manera, C. Maraston, J. L. Marshall, P. Martini, R. G. McMahon, P. Melchior, A. Merson, C. J. Miller, R. Miquel, J. J. Mohr, X. Morice-Atkinson, K. Naidoo, E. Neilsen, R. C. Nichol, B. Nord, R. Ogando, F. Ostrovski, A. Palmese, A. Papadopoulos, H. V. Peiris, J. Peoples, W. J. Percival, A. A. Plazas, S. L. Reed, A. Refregier, A. K. Romer, A. Roodman, A. Ross, E. Rozo, E. S. Rykoff, I. Sadeh, M. Sako, C. Sánchez, E. Sanchez, B. Santiago, V. Scarpine, M. Schubnell, I. Sevilla-Noarbe, E. Sheldon, M. Smith, R. C. Smith, M. Soares-Santos, F. Sobreira, M. Soumagnac, E. Suchyta, M. Sullivan, M. Swanson, G. Tarle, J. Thaler, D. Thomas, R. C. Thomas, D. Tucker, J. D. Vieira, V. Vikram, A. R. Walker, R. H. Wechsler, J. Weller, W. Wester, L. Whiteway, H. Wilcox, B. Yanny, Y. Zhang, and J. Zuntz. The Dark Energy Survey: more than dark energy - an overview. *MNRAS*, 460(2):1270–1299, Aug 2016. doi: 10.1093/mnras/stw641.

A. J. Deason, V. Belokurov, K. M. Hamren, S. E. Koposov, K. M. Gilbert, R. L. Beaton, C. E. Dorman, P. Guhathakurta, S. R. Majewski, and E. C. Cunningham. TriAnd and its siblings: satellites of satellites in the Milky Way halo. *MNRAS*, 444(4):3975–3985, Nov 2014. doi: 10.1093/mnras/stu1764.

H. T. Diehl, T. M. C. Abbott, J. Annis, R. Armstrong, L. Baruah, A. Bermeo, G. Bernstein, E. Beynon, C. Bruderer, E. J. Buckley-Geer, H. Campbell, D. Capozzi, M. Carter, R. Casas, L. Clerkin, R. Covarrubias, C. Cuhna, C. D'Andrea, L. da Costa, R. Das, D. L. DePoy, J. Dietrich, A. Drlica-Wagner, A. Elliott, T. Eifler, J. Estrada, J. Etherington, B. L. Flaugher, J. Frie-

man, A. Fausti Neto, M. Gelman, D. Gerdes, D. Gruen, R. Gruendl, J. Hao, H. Head, J. Helsby, K. Hoffman, K. Honscheid, D. James, M. Johnson, T. Kacprzac, J. Katsaros, R. Kennedy, S. Kent, R. Kessler, A. Kim, E. Krause, R. Kron, S. Kuhlmann, A. Kunder, T. Li, H. Lin, N. Maccrann, M. March, J. Marshall, E. Neilsen, P. Nugent, P. Martini, P. Melchior, F. Menanteau, R. C. Nichol, B. Nord, R. Ogando, L. Old, A. Papadopoulos, K. Patton, D. Petravick, A. A. Plazas, R. Poulton, A. Pujol, K. Reil, T. Rigby, A. Romer, A. Roodman, P. Rooney, E. Sanchez Alvaro, S. Serrano, E. Sheldon, A. Smith, R. C. Smith, M. Soares-Santos, M. Soumagnac, H. Spinka, E. Suchyta, D. Tucker, A. R. Walker, W. Wester, M. Wiesner, H. Wilcox, R. Williams, B. Yanny, and Y. . Zhang. *The Dark Energy Survey and operations: Year 1*, volume 9149 of *Society of Photo-Optical Instrumentation Engineers (SPIE) Conference Series*, page 91490V. 2014. doi: 10.1117/12.2056982.

H. T. Diehl, E. Neilsen, R. Gruendl, B. Yanny, T. M. C. Abbott, J. Aleksić, S. Allam, J. Annis, E. Balbinot, M. Baumer, L. Beaufore, K. Bechtol, G. Bernstein, S. Birrer, C. Bonnett, D. Brout, C. Bruderer, E. J. Buckley-Geer, D. Capozzi, A. Carnero Rosell, F. J. Castander, R. Cawthon, C. Chang, L. Clerkin, R. Covarrubias, C. Cuhna, C. D'Andrea, L. da Costa, R. Das, C. Davis, J. Dietrich, A. Drlica-Wagner, A. Elliott, T. F. Eifler, J. Etherington, B. L. Flaugher, J. Frieman, A. Fausti Neto, M. G. Fernández, C. Furlanetto, D. Gangkofner, D. W. Gerdes, D. A. Goldstein, K. Grabowski, R. R. Gupta, S. Hamilton, H. Head, J. Helsby, D. Hollowood, K. Honscheid, D. James, M. Johnson, M. W. G. Johnson, S. Jouvel, T. Kacprzac, S. Kent, R. Kessler, A. Kim, E. Krause, C. I. Krawiec, A. Kremin, R. Kron, S. Kuhlmann, N. Kuropatkin, O. Lahav, J. Lasker, T. S. Li, E. Luque, N. Maccrann, M. March, J. Marshall, N. P. Mondrik, E. P. Morganson, D. Mudd, A. Nadolski, P. Nugent, P. Melchior, F. Menanteau, D. Q. Nagasawa, B. Nord, R. Ogando, L. Old, A. Palmese, D. Petravick, A. A. Plazas, A. Pujol, A. B. A. Queiroz, K. Reil, A. K. Romer, R. Rosenfeld, A. Roodman, P. Rooney, M. Sako, A. I. Salvador, C. Sánchez, E. Sánchez Álvaro, B. X. Santiago, A. Schooneveld, M. Schubnell, E. Sheldon, A. Smith, R. C. Smith, M. Soares-Santos, F. Sobreira, M. Soumagnac, H. Spinka, S. S. Tie, D. Tucker, V. Vikram, K. Vivas, A. R. Walker, W. Wester, M. Wiesner, H. Wilcox, P. Williams, A. Zenteno,

Y. Zhang, and Z. Zhang. *The dark energy survey and operations: years 1 to 3*, volume 9910 of *Society of Photo-Optical Instrumentation Engineers (SPIE) Conference Series*, page 99101D. 2016. doi: 10.1117/12.2233157.

A. J. Drake, S. G. Djorgovski, A. Mahabal, E. Beshore, S. Larson, M. J. Graham, R. Williams, E. Christensen, M. Catelan, A. Boattini, A. Gibbs, R. Hill, and R. Kowalski. First Results from the Catalina Real-Time Transient Survey. *ApJ*, 696(1):870–884, May 2009. doi: 10.1088/0004-637X/696/1/870.

A. J. Drake, M. Catelan, S. G. Djorgovski, G. Torrealba, M. J. Graham, V. Belokurov, S. E. Koposov, A. Mahabal, J. L. Prieto, C. Donalek, R. Williams, S. Larson, E. Christensen, and E. Beshore. Probing the Outer Galactic Halo with RR Lyrae from the Catalina Surveys. *ApJ*, 763(1):32, Jan 2013a. doi: 10.1088/0004-637X/763/1/32.

A. J. Drake, M. Catelan, S. G. Djorgovski, G. Torrealba, M. J. Graham, A. Mahabal, J. L. Prieto, C. Donalek, R. Williams, S. Larson, E. Christensen, and E. Beshore. Evidence for a Milky Way Tidal Stream Reaching Beyond 100 kpc. *ApJ*, 765(2):154, Mar 2013b. doi: 10.1088/0004-637X/765/2/154.

A. J. Drake, M. J. Graham, S. G. Djorgovski, M. Catelan, A. A. Mahabal, G. Torrealba, D. García-Álvarez, C. Donalek, J. L. Prieto, R. Williams, S. Larson, E. Christen sen, V. Belokurov, S. E. Koposov, E. Beshore, A. Boattini, A. Gibbs, R. Hill, R. Kowalski, J. Johnson, and F. Shelly. The Catalina Surveys Periodic Variable Star Catalog. *ApJS*, 213(1):9, Jul 2014. doi: 10.1088/0067-0049/213/1/9.

A. J. Drake, S. G. Djorgovski, M. Catelan, M. J. Graham, A. A. Mahabal, S. Larson, E. Christensen, G. Torrealba, E. Beshore, R. H. McNaught, G. Garradd, V. Belokurov, and S. E. Koposov. The Catalina Surveys Southern periodic variable star catalogue. *MNRAS*, 469(3):3688–3712, Aug 2017. doi: 10.1093/mnras/stx1085.

A. Drlica-Wagner, K. Bechtol, E. S. Rykoff, E. Luque, A. Queiroz, Y. Y. Mao, R. H. Wechsler, J. D. Simon, B. Santiago, B. Yanny, E. Balbinot, S. Dodelson, A. Fausti Neto, D. J. James, T. S. Li, M. A. G. Maia, J. L. Marshall, A. Pieres, K. Stringer, A. R. Walker, T. M. C. Abbott, F. B.

Abdalla, S. Allam, A. Benoit-Lévy, G. M. Bernstein, E. Bertin, D. Brooks, E. Buckley-Geer, D. L. Burke, A. Carnero Rosell, M. Carrasco Kind, J. Carretero, M. Crocce, L. N. da Costa, S. Desai, H. T. Diehl, J. P. Dietrich, P. Doel, T. F. Eifler, A. E. Evrard, D. A. Finley, B. Flaugher, P. Fosalba, J. Frieman, E. Gaztanaga, D. W. Gerdes, D. Gruen, R. A. Gruendl, G. Gutierrez, K. Honscheid, K. Kuehn, N. Kuropatkin, O. Lahav, P. Martini, R. Miquel, B. Nord, R. Ogando, A. A. Plazas, K. Reil, A. Roodman, M. Sako, E. Sanchez, V. Scarpine, M. Schubnell, I. Sevilla-Noarbe, R. C. Smith, M. Soares-Santos, F. Sobreira, E. Suchyta, M. E. C. Swanson, G. Tarle, D. Tucker, V. Vikram, W. Wester, Y. Zhang, J. Zuntz, and DES Collaboration. Eight Ultra-faint Galaxy Candidates Discovered in Year Two of the Dark Energy Survey. *ApJ*, 813(2):109, Nov 2015. doi: 10.1088/0004-637X/813/2/109.

M. L. Enoch, M. E. Brown, and A. J. Burgasser. Photometric Variability at the L/T Dwarf Boundary. *AJ*, 126(2):1006–1016, Aug 2003. doi: 10.1086/376598.

M. Fabrizio, G. Bono, V. F. Braga, D. Magurno, S. Marinoni, P. M. Marrese, I. Ferraro, G. Fiorentino, G. Giuffrida, G. Iannicola, M. Monelli, G. Altavilla, B. Chaboyer, M. Dall'Ora, C. K. Gilligan, A. Layden, M. Marengo, M. Nonino, G. W. Preston, B. Sesar, C. Sneden, E. Valenti, F. Thévenin, and E. Zoccali. On the Use of Field RR Lyrae as Galactic Probes. I. The Oosterhoff Dichotomy Based on Fundamental Variables. *ApJ*, 882(2):169, Sep 2019. doi: 10.3847/1538-4357/ab3977.

G. Fiorentino, G. Bono, M. Monelli, P. B. Stetson, E. Tolstoy, C. Gallart, M. Salaris, C. E. Martínez-Vázquez, and E. J. Bernard. Weak Galactic Halo-Dwarf Spheroidal Connection from RR Lyrae Stars. *ApJL*, 798(1):L12, Jan 2015. doi: 10.1088/2041-8205/798/1/L12.

R. Fisher. Dispersion on a Sphere. *Proceedings of the Royal Society of London Series A*, 217 (1130):295–305, May 1953. doi: 10.1098/rspa.1953.0064.

E. L. Fitzpatrick. Correcting for the Effects of Interstellar Extinction. *PASP*, 111(755):63–75, Jan 1999. doi: 10.1086/316293.

B. Flaugher, H. T. Diehl, K. Honscheid, T. M. C. Abbott, O. Alvarez, R. Angstadt, J. T. Annis, M. Antonik, O. Ballester, L. Beaufore, G. M. Bernstein, R. A. Bernstein, B. Bigelow, M. Bonati,

D. Boprie, D. Brooks, E. J. Buckley-Geer, J. Campa, L. Cardiel-Sas, F. J. Castand er, J. Castilla, H. Cease, J. M. Cela-Ruiz, S. Chappa, E. Chi, C. Cooper, L. N. da Costa, E. Dede, G. Derylo, D. L. DePoy, J. de Vicente, P. Doel, A. Drlica-Wagner, J. Eiting, A. E. Elliott, J. Emes, J. Estrada, A. Fausti Neto, D. A. Finley, R. Flores, J. Frieman, D. Gerdes, M. D. Gladders, B. Gregory, G. R. Gutierrez, J. Hao, S. E. Holland, S. Holm, D. Huffman, C. Jackson, D. J. James, M. Jonas, A. Karcher, I. Karliner, S. Kent, R. Kessler, M. Kozlovsky, R. G. Kron, D. Kubik, K. Kuehn, S. Kuhlmann, K. Kuk, O. Lahav, A. Lathrop, J. Lee, M. E. Levi, P. Lewis, T. S. Li, I. Mand richenko, J. L. Marshall, G. Martinez, K. W. Merritt, R. Miquel, F. Muñoz, E. H. Neilsen, R. C. Nichol, B. Nord, R. Ogando, J. Olsen, N. Palaio, K. Patton, J. Peoples, A. A. Plazas, J. Rauch, K. Reil, J. P. Rheault, N. A. Roe, H. Rogers, A. Roodman, E. Sanchez, V. Scarpine, R. H. Schindler, R. Schmidt, R. Schmitt, M. Schubnell, K. Schultz, P. Schurter, L. Scott, S. Serrano, T. M. Shaw, R. C. Smith, M. Soares-Santos, A. Stefanik, W. Stuermer, E. Suchyta, A. Sypniewski, G. Tarle, J. Thaler, R. Tighe, C. Tran, D. Tucker, A. R. Walker, G. Wang, M. Watson, C. Weaverdyck, W. Wester, R. Woods, B. Yanny, and DES Collaboration. The Dark Energy Camera. *AJ*, 150(5):150, Nov 2015. doi: 10.1088/0004-6256/150/5/150.

F. Förster, J. C. Maureira, J. San Martín, M. Hamuy, J. Martínez, P. Huijse, G. Cabrera, L. Galbany, T. de Jaeger, S. GonzálezGaitán, J. P. Anderson, H. Kunkarayakti, G. Pignata, F. Bufano, J. Littín, F. Olivares, G. Medina, R. C. Smith, A. K. Vivas, P. A. Estévez, R. Muñoz, and E. Vera. The High Cadence Transient Survey (HITS). I. Survey Design and Supernova Shock Breakout Constraints. *ApJ*, 832(2):155, Dec 2016. doi: 10.3847/0004-637X/832/2/155.

Gaia Collaboration, T. Prusti, J. H. J. de Bruijne, A. G. A. Brown, A. Vallenari, C. Babusiaux, C. A. L. Bailer-Jones, U. Bastian, M. Biermann, D. W. Evans, L. Eyer, F. Jansen, C. Jordi, S. A. Klioner, U. Lammers, L. Lindegren, X. Luri, F. Mignard, D. J. Milligan, C. Panem, V. Poinsignon, D. Pourbaix, S. Randich, G. Sarri, P. Sartoretti, H. I. Siddiqui, C. Soubiran, V. Valette, F. van Leeuwen, N. A. Walton, C. Aerts, F. Arenou, M. Cropper, R. Drimmel, E. Høg, D. Katz, M. G. Lattanzi, W. O'Mullane, E. K. Grebel, A. D. Holland, C. Huc, X. Passot, L. Bramante, C. Cacciari, J. Castañeda, L. Chaoul, N. Cheek, F. De Angeli, C. Fabricius, R. Guerra,

J. Hernández, A. Jean-Antoine-Piccolo, E. Masana, R. Messineo, N. Mowlavi, K. Nienartowicz, D. Ordóñez-Blanco, P. Panuzzo, J. Portell, P. J. Richards, M. Riello, G. M. Seabroke, P. Tanga, F. Thévenin, J. Torra, S. G. Els, G. Gracia-Abril, G. Comoretto, M. Garcia-Reinaldos, T. Lock, E. Mercier, M. Altmann, R. Andrae, T. L. Astraatmadja, I. Bellas-Velidis, K. Benson, J. Berthier, R. Blomme, G. Busso, B. Carry, A. Cellino, G. Clementini, S. Cowell, O. Creevey, J. Cuypers, M. Davidson, J. De Ridder, A. de Torres, L. Delchambre, A. Dell'Oro, C. Ducourant, Y. Frémat, M. García-Torres, E. Gosset, J. L. Halbwachs, N. C. Hambly, D. L. Harrison, M. Hauser, D. Hestroffer, S. T. Hodgkin, H. E. Huckle, A. Hutton, G. Jasniewicz, S. Jordan, M. Kontizas, A. J. Korn, A. C. Lanzafame, M. Manteiga, A. Moitinho, K. Muinonen, J. Osinde, E. Pancino, T. Pauwels, J. M. Petit, A. Recio-Blanco, A. C. Robin, L. M. Sarro, C. Siopis, M. Smith, K. W. Smith, A. Sozzetti, W. Thuillot, W. van Reeven, Y. Viala, U. Abbas, A. Abreu Aramburu, S. Accart, J. J. Aguado, P. M. Allan, W. Allasia, G. Altavilla, M. A. Álvarez, J. Alves, R. I. Anderson, A. H. Andrei, E. Anglada Varela, E. Antiche, T. Antoja, S. Antón, B. Arcay, A. Atzei, L. Ayache, N. Bach, S. G. Baker, L. Balaguer-Núñez, C. Barache, C. Barata, A. Barbier, F. Barblan, M. Baroni, D. Barrado y Navascués, M. Barros, M. A. Barstow, U. Becciani, M. Bellazzini, G. Bellei, A. Bello García, V. Belokurov, P. Bendjoya, A. Berihuete, L. Bianchi, O. Bienaymé, F. Billebaud, N. Blagorodnova, S. Blanco-Cuaresma, T. Boch, A. Bombrun, R. Borrachero, S. Bouquillon, G. Bourda, H. Bouy, A. Bragaglia, M. A. Breddels, N. Brouillet, T. Brüsemeister, B. Bucciarelli, F. Budnik, P. Burgess, R. Burgon, A. Burlacu, D. Busonero, R. Buzzi, E. Caffau, J. Cambras, H. Campbell, R. Cancelliere, T. Cantat-Gaudin, T. Carlucci, J. M. Carrasco, M. Castellani, P. Charlot, J. Charnas, P. Charvet, F. Chassat, A. Chiavassa, M. Clotet, G. Cocozza, R. S. Collins, P. Collins, G. Costigan, F. Crifo, N. J. G. Cross, M. Crosta, C. Crowley, C. Dafonte, Y. Damerdji, A. Dapergolas, P. David, M. David, P. De Cat, F. de Felice, P. de Laverny, F. De Luise, R. De March, D. de Martino, R. de Souza, J. Debosscher, E. del Pozo, M. Delbo, A. Delgado, H. E. Delgado, F. di Marco, P. Di Matteo, S. Diakite, E. Distefano, C. Dolding, S. Dos Anjos, P. Drazinos, J. Durán, Y. Dzigan, E. Ecale, B. Edvardsson, H. Enke, M. Erdmann, D. Escolar, M. Espina, N. W. Evans, G. Eynard Bontemps, C. Fabre, M. Fabrizio, S. Faigler, A. J.

Falcão, M. Farràs Casas, F. Faye, L. Federici, G. Fedorets, J. Fernández-Hernández, P. Fernique, A. Fienga, F. Figueras, F. Filippi, K. Findeisen, A. Fonti, M. Fouesneau, E. Fraile, M. Fraser, J. Fuchs, R. Furnell, M. Gai, S. Galleti, L. Galluccio, D. Garabato, F. García-Sedano, P. Garé, A. Garofalo, N. Garralda, P. Gavras, J. Gerssen, R. Geyer, G. Gilmore, S. Girona, G. Giuffrida, M. Gomes, A. González-Marcos, J. González-Núñez, J. J. González-Vidal, M. Granvik, A. Guerrier, P. Guillout, J. Guiraud, A. Gúrpide, R. Gutiérrez-Sánchez, L. P. Guy, R. Haigron, D. Hatzidimitriou, M. Haywood, U. Heiter, A. Helmi, D. Hobbs, W. Hofmann, B. Holl, G. Holland , J. A. S. Hunt, A. Hypki, V. Icardi, M. Irwin, G. Jevardat de Fombelle, P. Jofré, P. G. Jonker, A. Jorissen, F. Julbe, A. Karampelas, A. Kochoska, R. Kohley, K. Kolenberg, E. Kontizas, S. E. Koposov, G. Kordopatis, P. Koubsky, A. Kowalczyk, A. Krone-Martins, M. Kudryashova, I. Kull, R. K. Bachchan, F. Lacoste-Seris, A. F. Lanza, J. B. Lavigne, C. Le Poncin-Lafitte, Y. Lebreton, T. Lebzelter, S. Leccia, N. Leclerc, I. Lecoeur-Taibi, V. Lemaitre, H. Lenhardt, F. Leroux, S. Liao, E. Licata, H. E. P. Lindstrøm, T. A. Lister, E. Livanou, A. Lobel, W. Löffler, M. López, A. Lopez-Lozano, D. Lorenz, T. Loureiro, I. MacDonald, T. Magalhães Fernandes, S. Managau, R. G. Mann, G. Mantelet, O. Marchal, J. M. Marchant, M. Marconi, J. Marie, S. Marinoni, P. M. Marrese, G. Marschalkó, D. J. Marshall, J. M. Martín-Fleitas, M. Martino, N. Mary, G. Matijevič, T. Mazeh, P. J. McMillan, S. Messina, A. Mestre, D. Michalik, N. R. Millar, B. M. H. Miranda, D. Molina, R. Molinaro, M. Molinaro, L. Molnár, M. Moniez, P. Montegriffo, D. Monteiro, R. Mor, A. Mora, R. Morbidelli, T. Morel, S. Morgenthaler, T. Morley, D. Morris, A. F. Mulone, T. Muraveva, I. Musella, J. Narbonne, G. Nelemans, L. Nicastro, L. Noval, C. Ordénovic, J. Ordieres-Meré, P. Osborne, C. Pagani, I. Pagano, F. Pailler, H. Palacin, L. Palaversa, P. Parsons, T. Paulsen, M. Pecoraro, R. Pedrosa, H. Pentikäinen, J. Pereira, B. Pichon, A. M. Piersimoni, F. X. Pineau, E. Plachy, G. Plum, E. Poujoulet, A. Prša, L. Pulone, S. Ragaini, S. Rago, N. Rambaux, M. Ramos-Lerate, P. Ranalli, G. Rauw, A. Read, S. Regibo, F. Renk, C. Reylé, R. A. Ribeiro, L. Rimoldini, V. Ripepi, A. Riva, G. Rixon, M. Roelens, M. Romero-Gómez, N. Rowell, F. Royer, A. Rudolph, L. Ruiz-Dern, G. Sadowski, T. Sagristà Sellés, J. Sahlmann, J. Salgado, E. Salguero, M. Sarasso, H. Savietto, A. Schnorhk, M. Schultheis,

E. Sciacca, M. Segol, J. C. Segovia, D. Segransan, E. Serpell, I. C. Shih, R. Smareglia, R. L. Smart, C. Smith, E. Solano, F. Solitro, R. Sordo, S. Soria Nieto, J. Souchay, A. Spagna, F. Spoto, U. Stampa, I. A. Steele, H. Steidelmüller, C. A. Stephenson, H. Stoev, F. F. Suess, M. Süveges, J. Surdej, L. Szabados, E. Szegedi-Elek, D. Tapiador, F. Taris, G. Tauran, M. B. Taylor, R. Teixeira, D. Terrett, B. Tingley, S. C. Trager, C. Turon, A. Ulla, E. Utrilla, G. Valentini, A. van Elteren, E. Van Hemelryck, M. van Leeuwen, M. Varadi, A. Vecchiato, J. Veljanoski, T. Via, D. Vicente, S. Vogt, H. Voss, V. Votruba, S. Voutsinas, G. Walmsley, M. Weiler, K. Weingrill, D. Werner, T. Wevers, G. Whitehead, Ł. Wyrzykowski, A. Yoldas, M. Žerjal, S. Zucker, C. Zurbach, T. Zwitter, A. Alecu, M. Allen, C. Allende Prieto, A. Amorim, G. Anglada-Escudé, V. Arsenijevic, S. Azaz, P. Balm, M. Beck, H. H. Bernstein, L. Bigot, A. Bijaoui, C. Blasco, M. Bonfigli, G. Bono, S. Boudreault, A. Bressan, S. Brown, P. M. Brunet, P. Bunclark, R. Buonanno, A. G. Butkevich, C. Carret, C. Carrion, L. Chemin, F. Chéreau, L. Corcione, E. Darmigny, K. S. de Boer, P. de Teodoro, P. T. de Zeeuw, C. Delle Luche, C. D. Domingues, P. Dubath, F. Fodor, B. Frézouls, A. Fries, D. Fustes, D. Fyfe, E. Gallardo, J. Gallegos, D. Gardiol, M. Gebran, A. Gomboc, A. Gómez, E. Grux, A. Gueguen, A. Heyrovsky, J. Hoar, G. Iannicola, Y. Isasi Parache, A. M. Janotto, E. Joliet, A. Jonckheere, R. Keil, D. W. Kim, P. Klagyivik, J. Klar, J. Knude, O. Kochukhov, I. Kolka, J. Kos, A. Kutka, V. Lainey, D. LeBouquin, C. Liu, D. Loreggia, V. V. Makarov, M. G. Marseille, C. Martayan, O. Martinez-Rubi, B. Massart, F. Meynadier, S. Mignot, U. Munari, A. T. Nguyen, T. Nordlander, P. Ocvirk, K. S. O'Flaherty, A. Olias Sanz, P. Ortiz, J. Osorio, D. Oszkiewicz, A. Ouzounis, M. Palmer, P. Park, E. Pasquato, C. Peltzer, J. Peralta, F. Péturaud, T. Pieniluoma, E. Pigozzi, J. Poels, G. Prat, T. Prod'homme, F. Raison, J. M. Rebordao, D. Risquez, B. Rocca-Volmerange, S. Rosen, M. I. Ruiz-Fuertes, F. Russo, S. Sembay, I. Serraller Vizcaino, A. Short, A. Siebert, H. Silva, D. Sinachopoulos, E. Slezak, M. Soffel, D. Sosnowska, V. Straižys, M. ter Linden, D. Terrell, S. Theil, C. Tiede, L. Troisi, P. Tsalmantza, D. Tur, M. Vaccari, F. Vachier, P. Valles, W. Van Hamme, L. Veltz, J. Virtanen, J. M. Wallut, R. Wichmann, M. I. Wilkinson, H. Ziaeepour, and S. Zschocke. The Gaia mission. *A&A*, 595:A1, Nov 2016. doi: 10.1051/0004-6361/201629272.

K. M. Górski, E. Hivon, A. J. Banday, B. D. Wand elt, F. K. Hansen, M. Reinecke, and M. Bartelmann. HEALPix: A Framework for High-Resolution Discretization and Fast Analysis of Data Distributed on the Sphere. *ApJ*, 622(2):759–771, Apr 2005. doi: 10.1086/427976.

R. G. Gratton, A. Bragaglia, E. Carretta, G. Clementini, S. Desidera, F. Grundahl, and S. Lucatello. Distances and ages of NGC 6397, NGC 6752 and 47 Tuc. *A&A*, 408:529–543, Sep 2003. doi: 10.1051/0004-6361:20031003.

C. Greco, G. Clementini, E. V. Held, E. Poretti, M. Catelan, L. Dell'Arciprete, M. Gullieuszik, M. Maio, L. Rizzi, H. A. Smith, B. J. Pritzl, A. Rest, and N. De Lee. Variable stars in Fornax dwarf spheroidal galaxy. *arXiv e-prints*, art. astro-ph/0507244, Jul 2005.

C. J. Grillmair. Detection of a 60-long Dwarf Galaxy Debris Stream. *ApJL*, 645(1):L37–L40, Jul 2006. doi: 10.1086/505863.

C. J. Grillmair. Four New Stellar Debris Streams in the Galactic Halo. *ApJ*, 693(2):1118–1127, Mar 2009. doi: 10.1088/0004-637X/693/2/1118.

C. J. Grillmair and J. L. Carlin. *Stellar Streams and Clouds in the Galactic Halo*, volume 420 of *Astrophysics and Space Science Library*, page 87. 2016. doi: 10.1007/978-3-319-19336-6_4.

A. N. Heinze, J. L. Tonry, L. Denneau, H. Flewelling, B. Stalder, A. Rest, K. W. Smith, S. J. Smartt, and H. Weiland. A First Catalog of Variable Stars Measured by the Asteroid Terrestrial-impact Last Alert System (ATLAS). *AJ*, 156(5):241, Nov 2018. doi: 10.3847/1538-3881/aae47f.

N. Hernitschek, E. F. Schlafly, B. Sesar, H.-W. Rix, D. W. Hogg, Ž. Ivezić, E. K. Grebel, E. F. Bell, N. F. Martin, W. S. Burgett, H. Flewelling, K. W. Hodapp, N. Kaiser, E. A. Magnier, N. Metcalfe, R. J. Wainscoat, and C. Waters. Finding, Characterizing, and Classifying Variable Sources in Multi-epoch Sky Surveys: QSOs and RR Lyrae in PS1 3π data. *ApJ*, 817(1):73, Jan 2016. doi: 10.3847/0004-637X/817/1/73.

N. Hernitschek, J. G. Cohen, H.-W. Rix, B. Sesar, N. F. Martin, E. Magnier, R. Wainscoat, N. Kaiser, J. L. Tonry, R.-P. Kudritzki, K. Hodapp, K. Chambers, H. Flewelling, and W. Burgett. The Profile of the Galactic Halo from Pan-STARRS1 3π RR Lyrae. *ApJ*, 859(1):31, May 2018. doi: 10.3847/1538-4357/aabfbb.

B. Holl, M. Audard, K. Nienartowicz, G. Jevardat de Fombelle, O. Marchal, N. Mowlavi, G. Clementini, J. De Ridder, D. W. Evans, L. P. Guy, A. C. Lanzafame, T. Lebzelter, L. Rimoldini, M. Roelens, S. Zucker, E. Distefano, A. Garofalo, I. Lecoeur-Taïbi, M. Lopez, R. Molinaro, T. Muraveva, A. Panahi, S. Regibo, V. Ripepi, L. M. Sarro, C. Aerts, R. I. Anderson, J. Charnas, F. Barblan, S. Blanco-Cuaresma, G. Busso, J. Cuypers, F. De Angeli, F. Glass, M. Grenon, Á. L. Juhász, A. Kochoska, P. Koubsky, A. F. Lanza, S. Leccia, D. Lorenz, M. Marconi, G. Marschalkó, T. Mazeh, S. Messina, F. Mignard, A. Moitinho, L. Molnár, S. Morgenthaler, I. Musella, C. Ordenovic, D. Ordóñez, I. Pagano, L. Palaversa, M. Pawlak, E. Plachy, A. Prša, M. Riello, M. Süveges, L. Szabados, E. Szegedi-Elek, V. Votruba, and L. Eyer. Gaia Data Release 2. Summary of the variability processing and analysis results. *A&A*, 618:A30, Oct 2018. doi: 10.1051/0004-6361/201832892.

M. J. Irwin, V. Belokurov, N. W. Evans, E. V. Ryan-Weber, J. T. A. de Jong, S. Koposov, D. B. Zucker, S. T. Hodgkin, G. Gilmore, P. Prema, L. Hebb, A. Begum, M. Fellhauer, P. C. Hewett, J. Kennicutt, R. C., M. I. Wilkinson, D. M. Bramich, S. Vidrih, H. W. Rix, T. C. Beers, J. C. Barentine, H. Brewington, M. Harvanek, J. Krzesinski, D. Long, A. Nitta, and S. A. Snedden. Discovery of an Unusual Dwarf Galaxy in the Outskirts of the Milky Way. *ApJL*, 656(1):L13–L16, Feb 2007. doi: 10.1086/512183.

Ž. Ivezić, R. H. Lupton, D. Schlegel, B. Boroski, J. Adelman-McCarthy, B. Yanny, S. Kent, C. Stoughton, D. Finkbeiner, N. Padmanabhan, C. M. Rockosi, J. E. Gunn, G. R. Knapp, M. A. Strauss, G. T. Richards, D. Eisenstein, T. Nicinski, S. J. Kleinman, J. Krzesinski, P. R. Newman, S. Snedden, A. R. Thakar, A. Szalay, J. A. Munn, J. A. Smith, D. Tucker, and B. C. Lee. SDSS data management and photometric quality assessment. *Astronomische Nachrichten*, 325 (6):583–589, Oct 2004. doi: 10.1002/asna.200410285.

Ž. Ivezić, J. A. Smith, G. Miknaitis, H. Lin, D. Tucker, R. H. Lupton, J. E. Gunn, G. R. Knapp, M. A. Strauss, B. Sesar, M. Doi, M. Tanaka, M. Fukugita, J. Holtzman, S. Kent, B. Yanny, D. Schlegel, D. Finkbeiner, N. Padmanabhan, C. M. Rockosi, M. Jurić, N. Bond, B. Lee, C. Stoughton, S. Jester, H. Harris, P. Harding, H. Morrison, J. Brinkmann, D. P. Schneider,

and D. York. Sloan Digital Sky Survey Standard Star Catalog for Stripe 82: The Dawn of Industrial 1% Optical Photometry. *AJ*, 134(3):973–998, Sep 2007. doi: 10.1086/519976.

Ž. Ivezić, B. Sesar, M. Jurić, N. Bond, J. Dalcanton, C. M. Rockosi, B. Yanny, H. J. Newberg, T. C. Beers, C. Allende Prieto, R. Wilhelm, Y. S. Lee, T. Sivarani, J. E. Norris, C. A. L. Bailer-Jones, P. Re Fiorentin, D. Schlegel, A. Uomoto, R. H. Lupton, G. R. Knapp, J. E. Gunn, K. R. Covey, J. Allyn Smith, G. Miknaitis, M. Doi, M. Tanaka, M. Fukugita, S. Kent, D. Finkbeiner, J. A. Munn, J. R. Pier, T. Quinn, S. Hawley, S. Anderson, F. Kiuchi, A. Chen, J. Bushong, H. Sohi, D. Haggard, A. Kimball, J. Barentine, H. Brewington, M. Harvanek, S. Kleinman, J. Krzesinski, D. Long, A. Nitta, S. Snedden, B. Lee, H. Harris, J. Brinkmann, D. P. Schneider, and D. G. York. The Milky Way Tomography with SDSS. II. Stellar Metallicity. *ApJ*, 684(1):287–325, Sep 2008. doi: 10.1086/589678.

Ž. Ivezić, S. M. Kahn, J. A. Tyson, B. Abel, E. Acosta, R. Allsman, D. Alonso, Y. AlSayyad, S. F. Anderson, J. Andrew, J. R. P. Angel, G. Z. Angeli, R. Ansari, P. Antilogus, C. Araujo, R. Armstrong, K. T. Arndt, P. Astier, É. Aubourg, N. Auza, T. S. Axelrod, D. J. Bard, J. D. Barr, A. Barrau, J. G. Bartlett, A. E. Bauer, B. J. Bauman, S. Baumont, E. Bechtol, K. Bechtol, A. C. Becker, J. Becla, C. Beldica, S. Bellavia, F. B. Bianco, R. Biswas, G. Blanc, J. Blazek, R. D. Bland ford, J. S. Bloom, J. Bogart, T. W. Bond, M. T. Booth, A. W. Borgland, K. Borne, J. F. Bosch, D. Boutigny, C. A. Brackett, A. Bradshaw, W. N. Brand t, M. E. Brown, J. S. Bullock, P. Burchat, D. L. Burke, G. Cagnoli, D. Calabrese, S. Callahan, A. L. Callen, J. L. Carlin, E. L. Carlson, S. Chand rasekharan, G. Charles-Emerson, S. Chesley, E. C. Cheu, H.-F. Chiang, J. Chiang, C. Chirino, D. Chow, D. R. Ciardi, C. F. Claver, J. Cohen-Tanugi, J. J. Cockrum, R. Coles, A. J. Connolly, K. H. Cook, A. Cooray, K. R. Covey, C. Cribbs, W. Cui, R. Cutri, P. N. Daly, S. F. Daniel, F. Daruich, G. Daubard, G. Daues, W. Dawson, F. Delgado, A. Dellapenna, R. de Peyster, M. de Val-Borro, S. W. Digel, P. Doherty, R. Dubois, G. P. Dubois-Felsmann, J. Durech, F. Economou, T. Eifler, M. Eracleous, B. L. Emmons, A. Fausti Neto, H. Ferguson, E. Figueroa, M. Fisher-Levine, W. Focke, M. D. Foss, J. Frank, M. D. Freemon, E. Gangler, E. Gawiser, J. C. Geary, P. Gee, M. Geha, C. J. B. Gessner, R. R. Gibson, D. K.

Gilmore, T. Glanzman, W. Glick, T. Goldina, D. A. Goldstein, I. Goodenow, M. L. Graham, W. J. Gressler, P. Gris, L. P. Guy, A. Guyonnet, G. Haller, R. Harris, P. A. Hascall, J. Haupt, F. Hernand ez, S. Herrmann, E. Hileman, J. Hoblitt, J. A. Hodgson, C. Hogan, J. D. Howard, D. Huang, M. E. Huffer, P. Ingraham, W. R. Innes, S. H. Jacoby, B. Jain, F. Jammes, M. J. Jee, T. Jenness, G. Jernigan, D. Jevremović, K. Johns, A. S. Johnson, M. W. G. Johnson, R. L. Jones, C. Juramy-Gilles, M. Jurić, J. S. Kalirai, N. J. Kallivayalil, B. Kalmbach, J. P. Kantor, P. Karst, M. M. Kasliwal, H. Kelly, R. Kessler, V. Kinnison, D. Kirkby, L. Knox, I. V. Kotov, V. L. Krabbendam, K. S. Krughoff, P. Kubánek, J. Kuczewski, S. Kulkarni, J. Ku, N. R. Kurita, C. S. Lage, R. Lambert, T. Lange, J. B. Langton, L. Le Guillou, D. Levine, M. Liang, K.-T. Lim, C. J. Lintott, K. E. Long, M. Lopez, P. J. Lotz, R. H. Lupton, N. B. Lust, L. A. MacArthur, A. Mahabal, R. Mand elbaum, T. W. Markiewicz, D. S. Marsh, P. J. Marshall, S. Marshall, M. May, R. McKercher, M. McQueen, J. Meyers, M. Migliore, M. Miller, D. J. Mills, C. Miraval, J. Moeyens, F. E. Moolekamp, D. G. Monet, M. Moniez, S. Monkewitz, C. Montgomery, C. B. Morrison, F. Mueller, G. P. Muller, F. Muñoz Arancibia, D. R. Neill, S. P. Newbry, J.-Y. Nief, A. Nomerotski, M. Nordby, P. O'Connor, J. Oliver, S. S. Olivier, K. Olsen, W. O'Mullane, S. Ortiz, S. Osier, R. E. Owen, R. Pain, P. E. Palecek, J. K. Parejko, J. B. Parsons, N. M. Pease, J. M. Peterson, J. R. Peterson, D. L. Petravick, M. E. Libby Petrick, C. E. Petry, F. Pierfederici, S. Pietrowicz, R. Pike, P. A. Pinto, R. Plante, S. Plate, J. P. Plutchak, P. A. Price, M. Prouza, V. Radeka, J. Rajagopal, A. P. Rasmussen, N. Regnault, K. A. Reil, D. J. Reiss, M. A. Reuter, S. T. Ridgway, V. J. Riot, S. Ritz, S. Robinson, W. Roby, A. Roodman, W. Rosing, C. Roucelle, M. R. Rumore, S. Russo, A. Saha, B. Sassolas, T. L. Schalk, P. Schellart, R. H. Schindler, S. Schmidt, D. P. Schneider, M. D. Schneider, W. Schoening, G. Schumacher, M. E. Schwamb, J. Sebag, B. Selvy, G. H. Sembroski, L. G. Seppala, A. Serio, E. Serrano, R. A. Shaw, I. Shipsey, J. Sick, N. Silvestri, C. T. Slater, J. A. Smith, R. C. Smith, S. Sobhani, C. Soldahl, L. Storrie-Lombardi, E. Stover, M. A. Strauss, R. A. Street, C. W. Stubbs, I. S. Sullivan, D. Sweeney, J. D. Swinbank, A. Szalay, P. Takacs, S. A. Tether, J. J. Thaler, J. G. Thayer, S. Thomas, A. J. Thornton, V. Thukral, J. Tice, D. E. Trilling, M. Turri, R. Van Berg, D. Vanden Berk, K. Vetter,

F. Virieux, T. Vucina, W. Wahl, L. Walkowicz, B. Walsh, C. W. Walter, D. L. Wang, S.-Y. Wang, M. Warner, O. Wiecha, B. Willman, S. E. Winters, D. Wittman, S. C. Wolff, W. M. Wood-Vasey, X. Wu, B. Xin, P. Yoachim, and H. Zhan. LSST: From Science Drivers to Reference Design and Anticipated Data Products. *ApJ*, 873(2):111, Mar 2019. doi: 10.3847/1538-4357/ab042c.

P. E. Jupp and K. V. Mardia. Maximum likelihood estimators for the matrix von mises-fisher and bingham distributions. *Ann. Statist.*, 7(3):599–606, 05 1979. doi: 10.1214/aos/1176344681. URL `https://doi.org/10.1214/aos/1176344681`.

J. Kaluzny, K. Z. Stanek, M. Krockenberger, D. D. Sasselov, J. L. Tonry, and M. Mateo. DIRECT Distances to Nearby Galaxies Using Detached Eclipsing Binaries and Cepheids. I. Variables in the Field M31B. *AJ*, 115(3):1016–1044, Mar 1998. doi: 10.1086/300235.

R. Kessler, J. Marriner, M. Childress, R. Covarrubias, C. B. D'Andrea, D. A. Finley, J. Fischer, R. J. Foley, D. Goldstein, R. R. Gupta, K. Kuehn, M. Marcha, R. C. Nichol, A. Papadopoulos, M. Sako, D. Scolnic, M. Smith, M. Sullivan, W. Wester, F. Yuan, T. Abbott, F. B. Abdalla, S. Allam, A. Benoit-Lévy, G. M. Bernstein, E. Bertin, D. Brooks, A. Carnero Rosell, M. Carrasco Kind, F. J. Castander, M. Crocce, L. N. da Costa, S. Desai, H. T. Diehl, T. F. Eifler, A. Fausti Neto, B. Flaugher, J. Frieman, D. W. Gerdes, D. Gruen, R. A. Gruendl, K. Honscheid, D. J. James, N. Kuropatkin, T. S. Li, M. A. G. Maia, J. L. Marshall, P. Martini, C. J. Miller, R. Miquel, B. Nord, R. Ogando, A. A. Plazas, K. Reil, A. K. Romer, A. Roodman, E. Sanchez, I. Sevilla-Noarbe, R. C. Smith, M. Soares-Santos, F. Sobreira, G. Tarle, J. Thaler, R. C. Thomas, D. Tucker, A. R. Walker, and DES Collaboration. The Difference Imaging Pipeline for the Transient Search in the Dark Energy Survey. *AJ*, 150(6):172, Dec 2015. doi: 10.1088/0004-6256/150/6/172.

D. Kim, H. Jerjen, D. Mackey, G. S. Da Costa, and A. P. Milone. A Hero's Dark Horse: Discovery of an Ultra-faint Milky Way Satellite in Pegasus. *ApJL*, 804(2):L44, May 2015. doi: 10.1088/2041-8205/804/2/L44.

D. S. King and J. P. Cox. Pulsating Stars. *PASP*, 80(475):365, Aug 1968. doi: 10.1086/128650.

S. E. Koposov, M. Irwin, V. Belokurov, E. Gonzalez-Solares, A. K. Yoldas, J. Lewis, N. Metcalfe,

and T. Shanks. Discovery of a cold stellar stream in the ATLAS DR1 data. *MNRAS*, 442: L85–L89, Jul 2014. doi: 10.1093/mnrasl/slu060.

S. E. Koposov, V. Belokurov, G. Torrealba, and N. W. Evans. Beasts of the Southern Wild: Discovery of Nine Ultra Faint Satellites in the Vicinity of the Magellanic Clouds. *ApJ*, 805(2):130, Jun 2015. doi: 10.1088/0004-637X/805/2/130.

S. E. Koposov, M. G. Walker, V. Belokurov, A. R. Casey, A. Geringer-Sameth, D. Mackey, G. Da Costa, D. Erkal, P. Jethwa, M. Mateo, E. W. Olszewski, and J. I. Bailey. Snake in the Clouds: a new nearby dwarf galaxy in the Magellanic bridge*. *MNRAS*, 479(4):5343–5361, Oct 2018. doi: 10.1093/mnras/sty1772.

A. Kunder, A. Walker, P. B. Stetson, G. Bono, J. M. Nemec, R. de Propris, M. Monelli, S. Cassisi, G. Andreuzzi, M. Dall'Ora, A. Di Cecco, and M. Zoccali. Period Change Similarities Among the RR Lyrae Variables in Oosterhoff I and Oosterhoff II Globular Systems. *AJ*, 141(1):15, Jan 2011. doi: 10.1088/0004-6256/141/1/15.

B. P. M. Laevens, N. F. Martin, E. J. Bernard, E. F. Schlafly, B. Sesar, H.-W. Rix, E. F. Bell, A. M. N. Ferguson, C. T. Slater, W. E. Sweeney, R. F. G. Wyse, A. P. Huxor, W. S. Burgett, K. C. Chambers, P. W. Draper, K. A. Hodapp, N. Kaiser, E. A. Magnier, N. Metcalfe, J. L. Tonry, R. J. Wainscoat, and C. Waters. Sagittarius II, Draco II and Laevens 3: Three New Milky Way Satellites Discovered in the Pan-STARRS 1 3π Survey. *ApJ*, 813(1):44, Nov 2015a. doi: 10.1088/0004-637X/813/1/44.

B. P. M. Laevens, N. F. Martin, R. A. Ibata, H.-W. Rix, E. J. Bernard, E. F. Bell, B. Sesar, A. M. N. Ferguson, E. F. Schlafly, C. T. Slater, W. S. Burgett, K. C. Chambers, H. Flewelling, K. A. Hodapp, N. Kaiser, R.-P. Kudritzki, R. H. Lupton, E. A. Magnier, N. Metcalfe, J. S. Morgan, P. A. Price, J. L. Tonry, R. J. Wainscoat, and C. Waters. A New Faint Milky Way Satellite Discovered in the Pan-STARRS1 3π Survey. *ApJL*, 802(2):L18, Apr 2015b. doi: 10.1088/2041-8205/802/2/L18.

J. Lafler and T. D. Kinman. An RR Lyrae Star Survey with Ihe Lick 20-INCH Astrograph II. The Calculation of RR Lyrae Periods by Electronic Computer. *ApJS*, 11:216, Jun 1965. doi:

10.1086/190116.

K. Lange. *Numerical Analysis for Statisticians*. Springer-Verlag New York Inc., 2010.

A. C. Layden. RR Lyrae Variables in the Inner Halo. I. Photometry. *AJ*, 115(1):193–203, Jan 1998. doi: 10.1086/300195.

J. F. Le Borgne, A. Paschke, J. Vandenbroere, E. Poretti, A. Klotz, M. Boër, Y. Damerdji, M. Martignoni, and F. Acerbi. Stellar evolution through the ages: period variations in galactic RRab stars as derived from the GEOS database and TAROT telescopes. *A&A*, 476(1):307–316, Dec 2007. doi: 10.1051/0004-6361:20077957.

J.-W. Lee, M. López-Morales, K. Hong, Y.-W. Kang, B. L. Pohl, and A. Walker. Toward a Better Understanding of the Distance Scale from RR Lyrae Variable Stars: A Case Study for the Inner Halo Globular Cluster NGC 6723. *ApJS*, 210(1):6, Jan 2014. doi: 10.1088/0067-0049/210/1/6.

T. S. Li, E. Balbinot, N. Mondrik, J. L. Marshall, B. Yanny, K. Bechtol, A. Drlica-Wagner, D. Oscar, B. Santiago, J. D. Simon, A. K. Vivas, A. R. Walker, M. Y. Wang, T. M. C. Abbott, F. B. Abdalla, A. Benoit-Lévy, G. M. Bernstein, E. Bertin, D. Brooks, D. L. Burke, A. Carnero Rosell, M. Carrasco Kind, J. Carretero, L. N. da Costa, D. L. DePoy, S. Desai, H. T. Diehl, P. Doel, J. Estrada, D. A. Finley, B. Flaugher, J. Frieman, D. Gruen, R. A. Gruendl, G. Gutierrez, K. Honscheid, D. J. James, K. Kuehn, N. Kuropatkin, O. Lahav, M. A. G. Maia, M. March, P. Martini, R. Ogando, A. A. Plazas, K. Reil, A. K. Romer, A. Roodman, E. Sanchez, V. Scarpine, M. Schubnell, I. Sevilla-Noarbe, R. C. Smith, M. Soares-Santos, F. Sobreira, E. Suchyta, M. E. C. Swanson, G. Tarle, D. Tucker, Y. Zhang, and DES Collaboration. Discovery of a Stellar Overdensity in Eridanus-Phoenix in the Dark Energy Survey. *ApJ*, 817 (2):135, Feb 2016. doi: 10.3847/0004-637X/817/2/135.

N. R. Lomb. Least-Squares Frequency Analysis of Unequally Spaced Data. *ApSS*, 39(2):447–462, Feb 1976. doi: 10.1007/BF00648343.

J. P. Long. A note on parameter estimation for misspecified regression models with heteroskedastic errors. *Electron. J. Statist.*, 11(1):1464–1490, 2017. doi: 10.1214/17-EJS1255. URL `https://doi.org/10.1214/17-EJS1255`.

E. Luque, A. Queiroz, B. Santiago, A. Pieres, E. Balbinot, K. Bechtol, A. Drlica-Wagner, A. F. Neto, L. N. da Costa, M. A. G. Maia, B. Yanny, T. Abbott, S. Allam, A. Benoit-Lévy, E. Bertin, D. Brooks, E. Buckley-Geer, D. L. Burke, A. C. Rosell, M. C. Kind, J. Carretero, C. E. Cunha, S. Desai, H. T. Diehl, J. P. Dietrich, T. F. Eifler, D. A. Finley, B. Flaugher, P. Fosalba, J. Frieman, D. W. Gerdes, D. Gruen, G. Gutierrez, K. Honscheid, D. J. James, K. Kuehn, N. Kuropatkin, O. Lahav, T. S. Li, M. March, J. L. Marshall, P. Martini, R. Miquel, E. Neilsen, R. C. Nichol, B. Nord, R. Ogando, A. A. Plazas, A. K. Romer, A. Roodman, E. Sanchez, V. Scarpine, M. Schubnell, I. Sevilla-Noarbe, R. C. Smith, M. Soares-Santos, F. Sobreira, E. Suchyta, M. E. C. Swanson, G. Tarle, J. Thaler, D. Tucker, A. R. Walker, and Y. Zhang. Digging deeper into the Southern skies: a compact Milky Way companion discovered in first-year Dark Energy Survey data. *MNRAS*, 458(1):603–612, May 2016. doi: 10.1093/mnras/stw302.

E. Luque, A. Pieres, B. Santiago, B. Yanny, A. K. Vivas, A. Queiroz, A. Drlica-Wagner, E. Morganson, E. Balbinot, J. L. Marshall, T. S. Li, A. F. Neto, L. N. da Costa, M. A. G. Maia, K. Bechtol, A. G. Kim, G. M. Bernstein, S. Dodelson, L. Whiteway, H. T. Diehl, D. A. Finley, T. Abbott, F. B. Abdalla, S. Allam, J. Annis, A. Benoit-Lévy, E. Bertin, D. Brooks, D. L. Burke, A. C. Rosell, M. C. Kind, J. Carretero, C. E. Cunha, C. B. D'Andrea, S. Desai, P. Doel, A. E. Evrard, B. Flaugher, P. Fosalba, D. W. Gerdes, D. A. Goldstein, D. Gruen, R. A. Gruendl, G. Gutierrez, D. J. James, K. Kuehn, N. Kuropatkin, O. Lahav, P. Martini, R. Miquel, B. Nord, R. Ogando, A. A. Plazas, A. K. Romer, E. Sanchez, V. Scarpine, M. Schubnell, I. Sevilla-Noarbe, R. C. Smith, M. Soares-Santos, F. Sobreira, E. Suchyta, M. E. C. Swanson, G. Tarle, D. Thomas, and A. R. Walker. The Dark Energy Survey view of the Sagittarius stream: discovery of two faint stellar system candidates. *MNRAS*, 468(1):97–108, Jun 2017. doi: 10.1093/mnras/stx405.

S. R. Majewski, J. C. Ostheimer, H. J. Rocha-Pinto, R. J. Patterson, P. Guhathakurta, and D. Reitzel. Detection of the Main-Sequence Turnoff of a Newly Discovered Milky Way Halo Structure in the Triangulum-Andromeda Region. *ApJ*, 615(2):738–743, Nov 2004. doi: 10.1086/424586.

M. Marconi. RR Lyrae pulsating stars as stellar population tracers and distance indicators . *Memorie della Societa Astronomica Italiana Supplementi*, 19:138, Jan 2012.

M. Marconi, G. Coppola, G. Bono, V. Braga, A. Pietrinferni, R. Buonanno, M. Castellani, I. Musella, V. Ripepi, and R. F. Stellingwerf. On a New Theoretical Framework for RR Lyrae Stars. I. The Metallicity Dependence. *ApJ*, 808(1):50, Jul 2015. doi: 10.1088/0004-637X/808/1/50.

C. E. Martínez-Vázquez, P. B. Stetson, M. Monelli, E. J. Bernard, G. Fiorentino, C. Gallart, G. Bono, S. Cassisi, M. Dall'Ora, I. Ferraro, G. Iannicola, and A. R. Walker. Variable stars in Local Group Galaxies - II. Sculptor dSph. *MNRAS*, 462(4):4349–4370, Nov 2016. doi: 10.1093/mnras/stw1895.

C. E. Martínez-Vázquez, M. Monelli, E. J. Bernard, C. Gallart, P. B. Stetson, E. D. Skillman, G. Bono, S. Cassisi, G. Fiorentino, K. B. W. McQuinn, A. A. Cole, A. W. McConnachie, N. F. Martin, A. E. Dolphin, M. Boylan-Kolchin, A. Aparicio, S. L. Hidalgo, and D. R. Weisz. The ISLAnds Project. III. Variable Stars in Six Andromeda Dwarf Spheroidal Galaxies. *ApJ*, 850 (2):137, Dec 2017. doi: 10.3847/1538-4357/aa9381.

C. E. Martínez-Vázquez, A. K. Vivas, M. Gurevich, A. R. Walker, M. McCarthy, A. B. Pace, K. M. Stringer, B. Santiago, R. Hounsell, L. Macri, T. S. Li, K. Bechtol, A. H. Riley, A. G. Kim, J. D. Simon, A. Drlica-Wagner, E. O. Nadler, J. L. Marshall, J. Annis, S. Avila, E. Bertin, D. Brooks, E. Buckley-Geer, D. L. Burke, A. Carnero Rosell, M. Carrasco Kind, L. N. da Costa, J. De Vicente, S. Desai, H. T. Diehl, P. Doel, S. Everett, J. Frieman, J. García-Bellido, E. Gaztanaga, D. Gruen, R. A. Gruendl, J. Gschwend, G. Gutierrez, D. L. Hollowood, K. Honscheid, D. J. James, K. Kuehn, N. Kuropatkin, M. A. G. Maia, F. Menanteau, C. J. Miller, R. Miquel, F. Paz-Chinchón, A. A. Plazas, E. Sanchez, V. Scarpine, S. Serrano, I. Sevilla-Noarbe, M. Smith, M. Soares-Santos, F. Sobreira, M. E. C. Swanson, G. Tarle, V. Vikram, and DES Collaboration. Search for RR Lyrae stars in DES ultrafaint systems: Grus I, Kim 2, Phoenix II, and Grus II. *MNRAS*, 490(2):2183–2199, Dec 2019. doi: 10.1093/mnras/stz2609.

C. Mateu, A. K. Vivas, R. Zinn, L. R. Miller, and C. Abad. No Excess of RR Lyrae Stars in the Canis Major Overdensity. *AJ*, 137(5):4412–4423, May 2009. doi: 10.1088/0004-6256/137/5/4412.

C. Mateu, A. K. Vivas, J. J. Downes, C. Briceño, R. Zinn, and G. Cruz-Diaz. The QUEST RR Lyrae Survey - III. The low Galactic latitude catalogue. *MNRAS*, 427(4):3374–3395, Dec 2012. doi: 10.1111/j.1365-2966.2012.21968.x.

C. Mateu, J. I. Read, and D. Kawata. Fourteen candidate RR Lyrae star streams in the inner Galaxy. *MNRAS*, 474(3):4112–4129, Mar 2018. doi: 10.1093/mnras/stx2937.

A. W. McConnachie. The Observed Properties of Dwarf Galaxies in and around the Local Group. *AJ*, 144(1):4, Jul 2012. doi: 10.1088/0004-6256/144/1/4.

G. E. Medina, R. R. Muñoz, A. K. Vivas, F. Förster, J. L. Carlin, J. Martinez, L. Galbany, S. González-Gaitán, M. Hamuy, T. de Jaeger, J. C. Maureira, and J. San Martín. Serendipitous Discovery of RR Lyrae Stars in the Leo V Ultra-faint Galaxy. *ApJL*, 845(1):L10, Aug 2017. doi: 10.3847/2041-8213/aa821e.

G. E. Medina, R. R. Muñoz, A. K. Vivas, J. L. Carlin, F. Förster, J. Martínez, L. Galbany, S. González-Gaitán, M. Hamuy, T. de Jaeger, J. C. Maureira, and J. San Martín. Discovery of Distant RR Lyrae Stars in the Milky Way Using DECam. *ApJ*, 855(1):43, Mar 2018. doi: 10.3847/1538-4357/aaad02.

N. Mondrik, J. P. Long, and J. L. Marshall. A Multiband Generalization of the Multiharmonic Analysis of Variance Period Estimation Algorithm and the Effect of Inter-band Observing Cadence on Period Recovery Rate. *ApJL*, 811(2):L34, Oct 2015. doi: 10.1088/2041-8205/811/2/L34.

E. Morganson, R. A. Gruendl, F. Menanteau, M. Carrasco Kind, Y. C. Chen, G. Daues, A. Drlica-Wagner, D. N. Friedel, M. Gower, M. W. G. Johnson, M. D. Johnson, R. Kessler, F. Paz-Chinchón, D. Petravick, C. Pond, B. Yanny, S. Allam, R. Armstrong, W. Barkhouse, K. Bechtol, A. Benoit-Lévy, G. M. Bernstein, E. Bertin, E. Buckley-Geer, R. Covarrubias, S. Desai, H. T. Diehl, D. A. Goldstein, D. Gruen, T. S. Li, H. Lin, J. Marriner, J. J. Mohr, E. Neilsen, C. C. Ngeow, K. Paech, E. S. Rykoff, M. Sako, I. Sevilla-Noarbe, E. Sheldon, F. Sobreira, D. L. Tucker, W. Wester, and DES Collaboration. The Dark Energy Survey Image Processing Pipeline. *PASP*, 130(989):074501, Jul 2018. doi: 10.1088/1538-3873/aab4ef.

T. Muraveva, H. E. Delgado, G. Clementini, L. M. Sarro, and A. Garofalo. RR Lyrae stars as standard candles in the Gaia Data Release 2 Era. *MNRAS*, 481(1):1195–1211, Nov 2018. doi: 10.1093/mnras/sty2241.

G. C. Myeong, N. W. Evans, V. Belokurov, J. L. Sand ers, and S. E. Koposov. The Milky Way Halo in Action Space. *ApJL*, 856(2):L26, Apr 2018. doi: 10.3847/2041-8213/aab613.

K. Nandra, I. M. George, R. F. Mushotzky, T. J. Turner, and T. Yaqoob. ASCA Observations of Seyfert 1 Galaxies. I. Data Analysis, Imaging, and Timing. *ApJ*, 476(1):70–82, Feb 1997. doi: 10.1086/303600.

E. Neilsen and J. Annis. *ObsTac: Automated Execution of Dark Energy Survey Observing Tactics*, volume 485 of *Astronomical Society of the Pacific Conference Series*, page 77. 2014.

E. H. Neilsen, Jr., G. Bernstein, R. Gruendl, and S. Kent. Limiting Magnitude, τ, t_{eff}, and Image Quality in DESY Year 1. 2016. doi: 10.2172/1250877.

H. J. Newberg, B. Yanny, C. Rockosi, E. K. Grebel, H.-W. Rix, J. Brinkmann, I. Csabai, G. Hennessy, R. B. Hindsley, R. Ibata, Z. Ivezić, D. Lamb, E. T. Nash, M. Odenkirchen, H. A. Rave, D. P. Schneider, J. A. Smith, A. Stolte, and D. G. York. The Ghost of Sagittarius and Lumps in the Halo of the Milky Way. *ApJ*, 569(1):245–274, Apr 2002. doi: 10.1086/338983.

M. Odenkirchen, E. K. Grebel, C. M. Rockosi, W. Dehnen, R. Ibata, H.-W. Rix, A. Stolte, C. Wolf, J. Anderson, John E., N. A. Bahcall, J. Brinkmann, I. Csabai, G. Hennessy, R. B. Hindsley, Ž. Ivezić, R. H. Lupton, J. A. Munn, J. R. Pier, C. Stoughton, and D. G. York. Detection of Massive Tidal Tails around the Globular Cluster Palomar 5 with Sloan Digital Sky Survey Commissioning Data. *ApJL*, 548(2):L165–L169, Feb 2001. doi: 10.1086/319095.

H. M. Oluseyi, A. C. Becker, C. Culliton, M. Furqan, K. L. Hoadley, P. Regencia, A. J. Wells, Ž. Ivezic, R. L. Jones, K. S. Krughoff, B. Sesar, S. Jacoby, and I. J. Allison. Simulated LSST Survey of RR Lyrae Stars throughout the Local Group. *AJ*, 144(1):9, Jul 2012. doi: 10.1088/0004-6256/144/1/9.

P. T. Oosterhoff. Some remarks on the variable stars in globular clusters. *The Observatory*, 62: 104–109, Apr 1939.

F. Pedregosa, G. Varoquaux, A. Gramfort, V. Michel, B. Thirion, O. Grisel, M. Blondel, A. Müller, J. Nothman, G. Louppe, P. Prettenhofer, R. Weiss, V. Dubourg, J. Vanderplas, A. Passos, D. Cournapeau, M. Brucher, M. Perrot, and É. Duchesnay. Scikit-learn: Machine Learning in Python. *arXiv e-prints*, art. arXiv:1201.0490, Jan 2012.

E. C. Pickering, H. R. Colson, W. P. Fleming, and L. D. Wells. Sixty-four new variable stars. *ApJ*, 13:226–230, Apr 1901. doi: 10.1086/140808.

A. Pieres, B. X. Santiago, A. Drlica-Wagner, K. Bechtol, R. P. v. d. Marel, G. Besla, N. F. Martin, V. Belokurov, C. Gallart, D. Martinez-Delgado, J. Marshall, N. E. D. Nöel, S. R. Majewski, M. R. L. Cioni, T. S. Li, W. Hartley, E. Luque, B. C. Conn, A. R. Walker, E. Balbinot, G. S. Stringfellow, K. A. G. Olsen, D. Nidever, L. N. da Costa, R. Ogando, M. Maia, A. F. Neto, T. M. C. Abbott, F. B. Abdalla, S. Allam, J. Annis, A. Benoit-Lévy, A. C. Rosell, M. C. Kind, J. Carretero, C. E. Cunha, C. B. D'Andrea, S. Desai, H. T. Diehl, P. Doel, B. Flaugher, P. Fosalba, J. García-Bellido, D. Gruen, R. A. Gruendl, J. Gschwend, G. Gutierrez, K. Honscheid, D. James, K. Kuehn, N. Kuropatkin, F. Menanteau, R. Miquel, A. A. Plazas, A. K. Romer, M. Sako, E. Sanchez, V. Scarpine, M. Schubnell, I. Sevilla-Noarbe, R. C. Smith, M. Soares-Santos, F. Sobreira, E. Suchyta, M. E. C. Swanson, G. Tarle, D. L. Tucker, and W. Wester. A stellar overdensity associated with the Small Magellanic Cloud. *MNRAS*, 468(2):1349–1360, Jun 2017. doi: 10.1093/mnras/stx507.

A. Pietrinferni, S. Cassisi, M. Salaris, and F. Castelli. A Large Stellar Evolution Database for Population Synthesis Studies. I. Scaled Solar Models and Isochrones. *ApJ*, 612(1):168–190, Sep 2004. doi: 10.1086/422498.

A. Pietrinferni, S. Cassisi, M. Salaris, and F. Castelli. A Large Stellar Evolution Database for Population Synthesis Studies. II. Stellar Models and Isochrones for an α-enhanced Metal Distribution. *ApJ*, 642(2):797–812, May 2006. doi: 10.1086/501344.

Z. Prudil, E. K. Grebel, I. Dékány, and R. Smolec. Photometric study of the SMCNOD using variable stars from the OGLE-IV survey. *MNRAS*, 480(1):669–680, Oct 2018. doi: 10.1093/mnras/sty1885.

Z. Prudil, I. Dékány, R. Smolec, M. Catelan, E. K. Grebel, and A. Kunder. Humps and bumps: The effects of shocks on the optical light curves of fundamental-mode RR Lyrae stars. *arXiv e-prints*, art. arXiv:2001.08272, Jan 2020.

J. D. Reimann. *Frequency Estimation Using Unequally-Spaced Astronomical Data.* PhD thesis, UNIVERSITY OF CALIFORNIA, BERKELEY., Jan 1994.

J. W. Richards, D. L. Starr, N. R. Butler, J. S. Bloom, J. M. Brewer, A. Crellin-Quick, J. Higgins, R. Kennedy, and M. Rischard. On Machine-learned Classification of Variable Stars with Sparse and Noisy Time-series Data. *ApJ*, 733(1):10, May 2011. doi: 10.1088/0004-637X/733/1/10.

L. Rimoldini, B. Holl, M. Audard, N. Mowlavi, K. Nienartowicz, D. W. Evans, L. P. Guy, I. Lecoeur-Taïbi, G. Jevardat de Fombelle, O. Marchal, M. Roelens, J. De Ridder, L. M. Sarro, S. Regibo, M. Lopez, G. Clementini, V. Ripepi, R. Molinaro, A. Garofalo, L. Molnár, E. Plachy, Á. Juhász, L. Szabados, T. Lebzelter, D. Teyssier, and L. Eyer. Gaia Data Release 2. All-sky classification of high-amplitude pulsating stars. *A&A*, 625:A97, May 2019. doi: 10.1051/0004-6361/201834616.

L. Rizzi, E. V. Held, I. Saviane, R. B. Tully, and M. Gullieuszik. The distance to the Fornax dwarf spheroidal galaxy. *MNRAS*, 380(3):1255–1260, Sep 2007. doi: 10.1111/j.1365-2966.2007.12196.x.

H. J. Rocha-Pinto, S. R. Majewski, M. F. Skrutskie, J. D. Crane, and R. J. Patterson. Exploring Halo Substructure with Giant Stars: A Diffuse Star Cloud or Tidal Debris around the Milky Way in Triangulum-Andromeda. *ApJ*, 615(2):732–737, Nov 2004. doi: 10.1086/424585.

P. Rousseeuw and C. Croux. Alternatives to median absolute deviation. *Journal of the American Statistical Association*, 88:1273 – 1283, 12 1993. doi: 10.1080/01621459.1993.10476408.

A. Saha and A. K. Vivas. A Hybrid Algorithm for Period Analysis from Multiband Data with Sparse and Irregular Sampling for Arbitrary Light-curve Shapes. *AJ*, 154(6):231, Dec 2017. doi: 10.3847/1538-3881/aa8fd3.

T. Sakamoto and T. Hasegawa. Discovery of a Faint Old Stellar System at 150 kpc. *ApJL*, 653(1):L29–L32, Dec 2006. doi: 10.1086/510332.

M. Salaris and S. Cassisi. *Evolution of Stars and Stellar Populations*. 2005.

N. N. Samus', E. V. Kazarovets, O. V. Durlevich, N. N. Kireeva, and E. N. Pastukhova. General catalogue of variable stars: Version GCVS 5.1. *Astronomy Reports*, 61(1):80–88, Jan 2017. doi: 10.1134/S1063772917010085.

R. E. Sanderson, A. Secunda, K. V. Johnston, and J. J. Bochanski. New views of the distant stellar halo. *MNRAS*, 470(4):5014–5031, Oct 2017. doi: 10.1093/mnras/stx1614.

J. D. Scargle. Studies in astronomical time series analysis. II. Statistical aspects of spectral analysis of unevenly spaced data. *ApJ*, 263:835–853, Dec 1982. doi: 10.1086/160554.

E. F. Schlafly and D. P. Finkbeiner. Measuring Reddening with Sloan Digital Sky Survey Stellar Spectra and Recalibrating SFD. *ApJ*, 737(2):103, Aug 2011. doi: 10.1088/0004-637X/737/2/103.

D. J. Schlegel, D. P. Finkbeiner, and M. Davis. Maps of Dust Infrared Emission for Use in Estimation of Reddening and Cosmic Microwave Background Radiation Foregrounds. *ApJ*, 500(2):525–553, Jun 1998. doi: 10.1086/305772.

B. Sesar, Ž. Ivezić, R. H. Lupton, M. Jurić, J. E. Gunn, G. R. Knapp, N. DeLee, J. A. Smith, G. Miknaitis, H. Lin, D. Tucker, M. Doi, M. Tanaka, M. Fukugita, J. Holtzman, S. Kent, B. Yanny, D. Schlegel, D. Finkbeiner, N. Padmanabhan, C. M. Rockosi, N. Bond, B. Lee, C. Stoughton, S. Jester, H. Harris, P. Harding, J. Brinkmann, D. P. Schneider, D. York, M. W. Richmond, and D. Vanden Berk. Exploring the Variable Sky with the Sloan Digital Sky Survey. *AJ*, 134(6):2236–2251, Dec 2007. doi: 10.1086/521819.

B. Sesar, Ž. Ivezić, S. H. Grammer, D. P. Morgan, A. C. Becker, M. Jurić, N. De Lee, J. Annis, T. C. Beers, X. Fan, R. H. Lupton, J. E. Gunn, G. R. Knapp, L. Jiang, S. Jester, D. E. Johnston, and H. Lampeitl. Light Curve Templates and Galactic Distribution of RR Lyrae Stars from Sloan Digital Sky Survey Stripe 82. *ApJ*, 708(1):717–741, Jan 2010. doi: 10.1088/0004-637X/708/1/717.

B. Sesar, S. R. Banholzer, J. G. Cohen, N. F. Martin, C. J. Grillmair, D. Levitan, R. R. Laher, E. O. Ofek, J. A. Surace, S. R. Kulkarni, T. A. Prince, and H.-W. Rix. Stacking the Invisibles:

A Guided Search for Low-luminosity Milky Way Satellites. *ApJ*, 793(2):135, Oct 2014. doi: 10.1088/0004-637X/793/2/135.

B. Sesar, N. Hernitschek, S. Mitrović, Ž. Ivezić, H.-W. Rix, J. G. Cohen, E. J. Bernard, E. K. Grebel, N. F. Martin, E. F. Schlafly, W. S. Burgett, P. W. Draper, H. Flewelling, N. Kaiser, R. P. Kudritzki, E. A. Magnier, N. Metcalfe, J. L. Tonry, and C. Waters. Machine-learned Identification of RR Lyrae Stars from Sparse, Multi-band Data: The PS1 Sample. *AJ*, 153(5): 204, May 2017. doi: 10.3847/1538-3881/aa661b.

S. Sharma, K. V. Johnston, S. R. Majewski, R. R. Muñoz, J. K. Carlberg, and J. Bullock. Group Finding in the Stellar Halo Using M-giants in the Two Micron All Sky Survey: An Extended View of the Pisces Overdensity? *ApJ*, 722(1):750–759, Oct 2010. doi: 10.1088/0004-637X/722/1/750.

N. Shipp, A. Drlica-Wagner, E. Balbinot, P. Ferguson, D. Erkal, T. S. Li, K. Bechtol, V. Belokurov, B. Buncher, D. Carollo, M. Carrasco Kind, K. Kuehn, J. L. Marshall, A. B. Pace, E. S. Rykoff, I. Sevilla-Noarbe, E. Sheldon, L. Strigari, A. K. Vivas, B. Yanny, A. Zenteno, T. M. C. Abbott, F. B. Abdalla, S. Allam, S. Avila, E. Bertin, D. Brooks, D. L. Burke, J. Carretero, F. J. Castander, R. Cawthon, M. Crocce, C. E. Cunha, C. B. D'Andrea, L. N. da Costa, C. Davis, J. De Vicente, S. Desai, H. T. Diehl, P. Doel, A. E. Evrard, B. Flaugher, P. Fosalba, J. Frieman, J. García-Bellido, E. Gaztanaga, D. W. Gerdes, D. Gruen, R. A. Gruendl, J. Gschwend, G. Gutierrez, W. Hartley, K. Honscheid, B. Hoyle, D. J. James, M. D. Johnson, E. Krause, N. Kuropatkin, O. Lahav, H. Lin, M. A. G. Maia, M. March, P. Martini, F. Menanteau, C. J. Miller, R. Miquel, R. C. Nichol, A. A. Plazas, A. K. Romer, M. Sako, E. Sanchez, B. Santiago, V. Scarpine, R. Schindler, M. Schubnell, M. Smith, R. C. Smith, F. Sobreira, E. Suchyta, M. E. C. Swanson, G. Tarle, D. Thomas, D. L. Tucker, A. R. Walker, R. H. Wechsler, and DES Collaboration. Stellar Streams Discovered in the Dark Energy Survey. *ApJ*, 862(2):114, Aug 2018. doi: 10.3847/1538-4357/aacdab.

M. H. Siegel, M. D. Shetrone, and M. Irwin. Trimming Down the Willman 1 dSph. *AJ*, 135(6): 2084–2094, Jun 2008. doi: 10.1088/0004-6256/135/6/2084.

T. Simm, R. Saglia, M. Salvato, R. Bender, W. S. Burgett, K. C. Chambers, P. W. Draper, H. Flewelling, N. Kaiser, R. P. Kudritzki, E. A. Magnier, N. Metcalfe, J. L. Tonry, R. J. Wainscoat, and C. Waters. Pan-STARRS1 variability of XMM-COSMOS AGN. I. Impact on photometric redshifts. *A&A*, 584:A106, Dec 2015. doi: 10.1051/0004-6361/201526859.

M. Smith, M. Sullivan, P. Wiseman, R. Kessler, D. Scolnic, D. Brout, C. B. D'Andrea, T. M. Davis, R. J. Foley, C. Frohmaier, L. Galbany, R. R. Gupta, C. P. Gutiérrez, S. R. Hinton, L. Kelsey, C. Lidman, E. Macaulay, A. Möller, R. C. Nichol, P. Nugent, A. Palmese, M. Pursiainen, M. Sako, R. C. Thomas, B. E. Tucker, D. Carollo, G. F. Lewis, N. E. Sommer, T. M. C. Abbott, M. Aguena, S. Allam, S. Avila, E. Bertin, S. Bhargava, D. Brooks, E. Buckley-Geer, D. L. Burke, A. Carnero Rosell, M. Carrasco Kind, M. Costanzi, L. N. da Costa, J. De Vicente, S. Desai, H. T. Diehl, P. Doel, T. F. Eifler, S. Everett, B. Flaugher, P. Fosalba, J. Frieman, J. García-Bellido, E. Gaztanaga, K. Glazebrook, D. Gruen, R. A. Gruendl, J. Gschwend, G. Gutierrez, W. G. Hartley, D. L. Hollowood, K. Honscheid, D. J. James, E. Krause, K. Kuehn, N. Kuropatkin, M. Lima, N. MacCrann, M. A. G. Maia, J. L. Marshall, P. Martini, P. Melchior, F. Menanteau, R. Miquel, F. Paz-Chinchón, A. A. Plazas, A. K. Romer, A. Roodman, E. S. Rykoff, E. Sanchez, V. Scarpine, M. Schubnell, S. Serrano, I. Sevilla-Noarbe, E. Suchyta, M. E. C. Swanson, G. Tarle, D. Thomas, D. L. Tucker, T. N. Varga, A. R. Walker, :, and The Dark Energy Survey Collaboration. First Cosmology Results using Type Ia Supernovae from the Dark Energy Survey: The Effect of Host Galaxy Properties on Supernova Luminosity. *arXiv e-prints*, art. arXiv:2001.11294, Jan 2020.

K. V. Sokolovsky, P. Gavras, A. Karampelas, S. V. Antipin, I. Bellas-Velidis, P. Benni, A. Z. Bonanos, A. Y. Burdanov, S. Derlopa, D. Hatzidimitriou, A. D. Khokhryakova, D. M. Kolesnikova, S. A. Korotkiy, E. G. Lapukhin, M. I. Moretti, A. A. Popov, E. Pouliasis, N. N. Samus, Z. Spetsieri, S. A. Veselkov, K. V. Volkov, M. Yang, and A. M. Zubareva. Comparative performance of selected variability detection techniques in photometric time series data. *MNRAS*, 464(1): 274–292, Jan 2017. doi: 10.1093/mnras/stw2262.

I. Soszyński, A. Udalski, M. K. Szymański, Ł. Wyrzykowski, K. Ulaczyk, R. Poleski, P. Pietrukow-

icz, S. Kozłowski, D. M. Skowron, J. Skowron, P. Mróz, and M. Pawlak. The OGLE Collection of Variable Stars. Over 45 000 RR Lyrae Stars in the Magellanic System. *Acta Astron.*, 66(2): 131–147, Jun 2016.

S. Sra. Directional Statistics in Machine Learning: a Brief Review. *arXiv e-prints*, art. arXiv:1605.00316, May 2016.

P. B. Stetson. On the Automatic Determination of Light-Curve Parameters for Cepheid Variables. *PASP*, 108:851, Oct 1996. doi: 10.1086/133808.

P. B. Stetson, G. Fiorentino, G. Bono, E. J. Bernard, M. Monelli, G. Iannicola, C. Gallart, and I. Ferraro. Homogeneous Photometry VI: Variable Stars in the Leo I Dwarf Spheroidal Galaxy. *PASP*, 126(941):616, Jul 2014. doi: 10.1086/677352.

K. M. Stringer, J. P. Long, L. M. Macri, J. L. Marshall, A. Drlica-Wagner, C. E. Martínez-Vázquez, A. K. Vivas, K. Bechtol, E. Morganson, M. Carrasco Kind, A. B. Pace, A. R. Walker, C. Nielsen, T. S. Li, E. Rykoff, D. Burke, A. Carnero Rosell, E. Neilsen, P. Ferguson, S. A. Cantu, J. L. Myron, L. Strigari, A. Farahi, F. Paz-Chinchón, D. Tucker, Z. Lin, D. Hatt, J. F. Maner, L. Plybon, A. H. Riley, E. O. Nadler, T. M. C. Abbott, S. Allam, J. Annis, E. Bertin, D. Brooks, E. Buckley-Geer, J. Carretero, C. E. Cunha, C. B. D'Andrea, L. N. da Costa, J. De Vicente, S. Desai, P. Doel, T. F. Eifler, B. Flaugher, J. Frieman, J. García-Bellido, E. Gaztanaga, D. Gruen, J. Gschwend, G. Gutierrez, W. G. Hartley, D. L. Hollowood, B. Hoyle, D. J. James, K. Kuehn, N. Kuropatkin, P. Melchior, R. Miquel, R. L. C. Ogando, A. A. Plazas, E. Sanchez, B. Santiago, V. Scarpine, M. Schubnell, S. Serrano, I. Sevilla-Noarbe, M. Smith, R. C. Smith, M. Soares-Santos, F. Sobreira, E. Suchyta, M. E. C. Swanson, G. Tarle, D. Thomas, V. Vikram, B. Yanny, and DES Collaboration. Identification of RR Lyrae Stars in Multiband, Sparsely Sampled Data from the Dark Energy Survey Using Template Fitting and Random Forest Classification. *AJ*, 158(1):16, Jul 2019. doi: 10.3847/1538-3881/ab1f46.

M. Süveges, B. Sesar, M. Váradi, N. Mowlavi, A. C. Becker, Ž. Ivezić, M. Beck, K. Nienartowicz, L. Rimoldini, P. Dubath, P. Bartholdi, and L. Eyer. Search for high-amplitude δ Scuti and RR Lyrae stars in Sloan Digital Sky Survey Stripe 82 using principal component analysis. *MNRAS*,

424(4):2528–2550, Aug 2012. doi: 10.1111/j.1365-2966.2012.21229.x.

R. Szabó, Z. Kolláth, and J. R. Buchler. Automated nonlinear stellar pulsation calculations: Applications to RR Lyrae stars. The slope of the fundamental blue edge and the first RRd model survey. *A&A*, 425:627–639, Oct 2004. doi: 10.1051/0004-6361:20035698.

The Dark Energy Survey Collaboration. The Dark Energy Survey. *arXiv e-prints*, art. astro-ph/0510346, Oct 2005.

J. L. Tonry, L. Denneau, A. N. Heinze, B. Stalder, K. W. Smith, S. J. Smartt, C. W. Stubbs, H. J. Weiland , and A. Rest. ATLAS: A High-cadence All-sky Survey System. *PASP*, 130(988): 064505, Jun 2018. doi: 10.1088/1538-3873/aabadf.

G. Torrealba, M. Catelan, A. J. Drake, S. G. Djorgovski, R. H. McNaught, V. Belokurov, S. Koposov, M. J. Graham, A. Mahabal, S. Larson, and E. Christensen. Discovery of 9000 new RR Lyrae in the southern Catalina surveys. *MNRAS*, 446(3):2251–2266, Jan 2015. doi: 10.1093/mnras/stu2274.

G. Torrealba, S. E. Koposov, V. Belokurov, and M. Irwin. The feeble giant. Discovery of a large and diffuse Milky Way dwarf galaxy in the constellation of Crater. *MNRAS*, 459(3):2370–2378, Jul 2016a. doi: 10.1093/mnras/stw733.

G. Torrealba, S. E. Koposov, V. Belokurov, M. Irwin, M. Collins, M. Spencer, R. Ibata, M. Mateo, A. Bonaca, and P. Jethwa. At the survey limits: discovery of the Aquarius 2 dwarf galaxy in the VST ATLAS and the SDSS data. *MNRAS*, 463(1):712–722, Nov 2016b. doi: 10.1093/mnras/stw2051.

G. Torrealba, V. Belokurov, S. E. Koposov, K. Bechtol, A. Drlica-Wagner, K. A. G. Olsen, A. K. Vivas, B. Yanny, P. Jethwa, A. R. Walker, T. S. Li, S. Allam, B. C. Conn, C. Gallart, R. A. Gruendl, D. J. James, M. D. Johnson, K. Kuehn, N. Kuropatkin, N. F. Martin, D. Martinez-Delgado, D. L. Nidever, N. E. D. Noël, J. D. Simon, G. S. Stringfellow, and D. L. Tucker. Discovery of two neighbouring satellites in the Carina constellation with MagLiteS. *MNRAS*, 475(4):5085–5097, Apr 2018. doi: 10.1093/mnras/sty170.

G. Torrealba, V. Belokurov, S. E. Koposov, T. S. Li, M. G. Walker, J. L. Sanders, A. Geringer-

Sameth, D. B. Zucker, K. Kuehn, N. W. Evans, and W. Dehnen. The hidden giant: discovery of an enormous Galactic dwarf satellite in Gaia DR2. *MNRAS*, 488(2):2743–2766, Sep 2019. doi: 10.1093/mnras/stz1624.

T. S. van Albada and N. Baker. On the Two Oosterhoff Groups of Globular Clusters. *ApJ*, 185: 477–498, Oct 1973. doi: 10.1086/152434.

J. T. VanderPlas. Understanding the Lomb-Scargle Periodogram. *ApJS*, 236(1):16, May 2018. doi: 10.3847/1538-4365/aab766.

J. T. VanderPlas and Ž. Ivezić. Periodograms for Multiband Astronomical Time Series. *ApJ*, 812 (1):18, Oct 2015. doi: 10.1088/0004-637X/812/1/18.

P. Virtanen, R. Gommers, T. E. Oliphant, M. Haberland, T. Reddy, D. Cournapeau, E. Burovski, P. Peterson, W. Weckesser, J. Bright, S. J. van der Walt, M. Brett, J. Wilson, K. Jarrod Millman, N. Mayorov, A. R. J. Nelson, E. Jones, R. Kern, E. Larson, C. Carey, İ. Polat, Y. Feng, E. W. Moore, J. Vand erPlas, D. Laxalde, J. Perktold, R. Cimrman, I. Henriksen, E. A. Quintero, C. R. Harris, A. M. Archibald, A. H. Ribeiro, F. Pedregosa, P. van Mulbregt, and S. . . Contributors. SciPy 1.0–Fundamental Algorithms for Scientific Computing in Python. *arXiv e-prints*, art. arXiv:1907.10121, Jul 2019.

A. K. Vivas and R. Zinn. The QUEST RR Lyrae Survey. II. The Halo Overdensities in the First Catalog. *AJ*, 132(2):714–728, Aug 2006. doi: 10.1086/505200.

A. K. Vivas, R. Zinn, P. Andrews, C. Bailyn, C. Baltay, P. Coppi, N. Ellman, T. Girard, D. Rabinowitz, B. Schaefer, J. Shin, J. Snyder, S. Sofia, W. van Altena, C. Abad, A. Bongiovanni, C. Briceño, G. Bruzual, F. Della Prugna, D. Herrera, G. Magris, J. Mateu, R. Pacheco, G. Sánchez, G. Sánchez, H. Schenner, J. Stock, B. Vicente, K. Vieira, I. Ferrín, J. Hernandez, M. Gebhard, R. Honeycutt, S. Mufson, J. Musser, and A. Rengstorf. The QUEST RR Lyrae Survey: Confirmation of the Clump at 50 Kiloparsecs and Other Overdensities in the Outer Halo. *ApJL*, 554(1):L33–L36, Jun 2001. doi: 10.1086/320915.

A. K. Vivas, R. Zinn, C. Abad, P. Andrews, C. Bailyn, C. Baltay, A. Bongiovanni, C. Briceño, G. Bruzual, P. Coppi, F. Della Prugna, N. Ellman, I. Ferrín, M. Gebhard, T. Girard, J. Hernan-

dez, D. Herrera, R. Honeycutt, G. Magris, S. Mufson, J. Musser, O. Naranjo, D. Rabinowitz, A. Rengstorf, P. Rosenzweig, G. Sánchez, G. Sánchez, B. Schaefer, H. Schenner, J. A. Snyder, S. Sofia, J. Stock, W. van Altena, B. Vicente, and K. Vieira. The QUEST RR Lyrae Survey. I. The First Catalog. *AJ*, 127(2):1158–1175, Feb 2004. doi: 10.1086/380929.

A. K. Vivas, K. Olsen, R. Blum, D. L. Nidever, A. R. Walker, N. F. Martin, G. Besla, C. Gallart, R. P. van der Marel, S. R. Majewski, C. C. Kaleida, R. R. Muñoz, A. Saha, B. C. Conn, and S. Jin. Variable Stars in the Field of the Hydra II Ultra-faint Dwarf Galaxy. *AJ*, 151(5):118, May 2016. doi: 10.3847/0004-6256/151/5/118.

A. K. Vivas, A. Saha, K. Olsen, R. Blum, E. W. Olszewski, J. Claver, F. Valdes, T. Axelrod, C. Kaleida, A. Kunder, G. Narayan, T. Matheson, and A. Walker. Absolute Magnitudes and Colors of RR Lyrae Stars in DECam Passbands from Photometry of the Globular Cluster M5. *AJ*, 154(3):85, Sep 2017. doi: 10.3847/1538-3881/aa7fed.

A. K. Vivas, J. Alonso-García, M. Mateo, A. Walker, and B. Howard. The Population of Pulsating Variable Stars in the Sextans Dwarf Spheroidal Galaxy. *AJ*, 157(1):35, Jan 2019. doi: 10.3847/1538-3881/aaf4f3.

S. M. Walsh, H. Jerjen, and B. Willman. A Pair of Boötes: A New Milky Way Satellite. *ApJL*, 662 (2):L83–L86, Jun 2007. doi: 10.1086/519684.

D. L. Welch and P. B. Stetson. Robust Variable Star Detection Techniques Suitable for Automated searches: New Results for NGC 1866. *AJ*, 105:1813, May 1993. doi: 10.1086/116556.

M. Wenger, F. Ochsenbein, D. Egret, P. Dubois, F. Bonnarel, S. Borde, F. Genova, G. Jasniewicz, S. Laloë, S. Lesteven, and R. Monier. The SIMBAD astronomical database. The CDS reference database for astronomical objects. *A&As*, 143:9–22, Apr 2000. doi: 10.1051/aas:2000332.

B. Willman. In Pursuit of the Least Luminous Galaxies. *Advances in Astronomy*, 2010:285454, Jan 2010. doi: 10.1155/2010/285454.

B. Willman, M. R. Blanton, A. A. West, J. J. Dalcanton, D. W. Hogg, D. P. Schneider, N. Wherry, B. Yanny, and J. Brinkmann. A New Milky Way Companion: Unusual Globular Cluster or Extreme Dwarf Satellite? *AJ*, 129(6):2692–2700, Jun 2005a. doi: 10.1086/430214.

B. Willman, J. J. Dalcanton, D. Martinez-Delgado, A. A. West, M. R. Blanton, D. W. Hogg, J. C. Barentine, H. J. Brewington, M. Harvanek, S. J. Kleinman, J. Krzesinski, D. Long, J. Neilsen, Eric H., A. Nitta, and S. A. Snedden. A New Milky Way Dwarf Galaxy in Ursa Major. *ApJL*, 626(2):L85–L88, Jun 2005b. doi: 10.1086/431760.

D. G. York, J. Adelman, J. Anderson, John E., S. F. Anderson, J. Annis, N. A. Bahcall, J. A. Bakken, R. Barkhouser, S. Bastian, E. Berman, W. N. Boroski, S. Bracker, C. Briegel, J. W. Briggs, J. Brinkmann, R. Brunner, S. Burles, L. Carey, M. A. Carr, F. J. Castander, B. Chen, P. L. Colestock, A. J. Connolly, J. H. Crocker, I. Csabai, P. C. Czarapata, J. E. Davis, M. Doi, T. Dombeck, D. Eisenstein, N. Ellman, B. R. Elms, M. L. Evans, X. Fan, G. R. Federwitz, L. Fiscelli, S. Friedman, J. A. Frieman, M. Fukugita, B. Gillespie, J. E. Gunn, V. K. Gurbani, E. de Haas, M. Haldeman, F. H. Harris, J. Hayes, T. M. Heckman, G. S. Hennessy, R. B. Hindsley, S. Holm, D. J. Holmgren, C.-h. Huang, C. Hull, D. Husby, S.-I. Ichikawa, T. Ichikawa, Ž. Ivezić, S. Kent, R. S. J. Kim, E. Kinney, M. Klaene, A. N. Kleinman, S. Kleinman, G. R. Knapp, J. Korienek, R. G. Kron, P. Z. Kunszt, D. Q. Lamb, B. Lee, R. F. Leger, S. Limmongkol, C. Lindenmeyer, D. C. Long, C. Loomis, J. Loveday, R. Lucinio, R. H. Lupton, B. MacKinnon, E. J. Mannery, P. M. Mantsch, B. Margon, P. McGehee, T. A. McKay, A. Meiksin, A. Merelli, D. G. Monet, J. A. Munn, V. K. Narayanan, T. Nash, E. Neilsen, R. Neswold, H. J. Newberg, R. C. Nichol, T. Nicinski, M. Nonino, N. Okada, S. Okamura, J. P. Ostriker, R. Owen, A. G. Pauls, J. Peoples, R. L. Peterson, D. Petravick, J. R. Pier, A. Pope, R. Pordes, A. Prosapio, R. Rechenmacher, T. R. Quinn, G. T. Richards, M. W. Richmond, C. H. Rivetta, C. M. Rockosi, K. Ruthmansdorfer, D. Sand ford, D. J. Schlegel, D. P. Schneider, M. Sekiguchi, G. Sergey, K. Shimasaku, W. A. Siegmund, S. Smee, J. A. Smith, S. Snedden, R. Stone, C. Stoughton, M. A. Strauss, C. Stubbs, M. SubbaRao, A. S. Szalay, I. Szapudi, G. P. Szokoly, A. R. Thakar, C. Tremonti, D. L. Tucker, A. Uomoto, D. Vanden Berk, M. S. Vogeley, P. Waddell, S.-i. Wang, M. Watanabe, D. H. Weinberg, B. Yanny, N. Yasuda, and SDSS Collaboration. The Sloan Digital Sky Survey: Technical Summary. *AJ*, 120(3):1579–1587, Sep 2000. doi: 10.1086/301513.

W. J. Youden. Index for rating diagnostic tests. *Cancer*, 3(1):32–35, 1950. doi:

10.1002/1097-0142(1950)3:1<32::AID-CNCR2820030106>3.0.CO;2-3. URL https://onlinelibrary.wiley.com/doi/abs/10.1002/1097-0142%281950%293%3A1%3C32%3A%3AAID-CNCR2820030106%3E3.0.CO%3B2-3.

D. B. Zucker, V. Belokurov, N. W. Evans, J. T. Kleyna, M. J. Irwin, M. I. Wilkinson, M. Fellhauer, D. M. Bramich, G. Gilmore, H. J. Newberg, B. Yanny, J. A. Smith, P. C. Hewett, E. F. Bell, H. W. Rix, O. Y. Gnedin, S. Vidrih, R. F. G. Wyse, B. Willman, E. K. Grebel, D. P. Schneider, T. C. Beers, A. Y. Kniazev, J. C. Barentine, H. Brewington, J. Brinkmann, M. Harvanek, S. J. Kleinman, J. Krzesinski, D. Long, A. Nitta, and S. A. Snedden. A Curious Milky Way Satellite in Ursa Major. *ApJL*, 650(1):L41–L44, Oct 2006a. doi: 10.1086/508628.

D. B. Zucker, V. Belokurov, N. W. Evans, M. I. Wilkinson, M. J. Irwin, T. Sivarani, S. Hodgkin, D. M. Bramich, J. M. Irwin, G. Gilmore, B. Willman, S. Vidrih, M. Fellhauer, P. C. Hewett, T. C. Beers, E. F. Bell, E. K. Grebel, D. P. Schneider, H. J. Newberg, R. F. G. Wyse, C. M. Rockosi, B. Yanny, R. Lupton, J. A. Smith, J. C. Barentine, H. Brewington, J. Brinkmann, M. Harvanek, S. J. Kleinman, J. Krzesinski, D. Long, A. Nitta, and S. A. Snedden. A New Milky Way Dwarf Satellite in Canes Venatici. *ApJL*, 643(2):L103–L106, Jun 2006b. doi: 10.1086/505216.

APPENDIX A

REPRESENTATIVE LIST OF DES Y6 RRAB CANDIDATES

ID	α	δ	$\langle g \rangle$	$\langle r \rangle$	$\langle i \rangle$	$\langle z \rangle$	$\langle Y \rangle$	P	A_g	μ
871820547	300.4591	-50.7457	15.352	15.201	15.221	15.225	15.039	0.5441	1.107	14.55
872060389	301.1574	-54.3232	19.217	18.935	18.841	18.647	18.647	0.6158	1.181	18.14
872212127	301.4859	-57.0505	17.941	17.671	17.770	17.715	17.810	0.5638	1.059	17.13
872268895	301.5402	-52.5811	14.797	14.721	—	14.637	14.741	0.5807	0.670	14.17
872444946	300.5736	-56.2696	16.417	16.272	16.270	16.223	16.241	0.6750	0.974	15.68
872520961	300.0244	-55.5218	15.112	—	—	14.780	14.640	0.5067	1.230	14.01
872648764	305.5164	-48.2773	15.392	15.062	14.987	14.984	15.126	0.5545	1.102	14.42
872732644	301.8146	-50.4171	15.952	15.787	15.738	15.867	15.754	0.6256	0.862	15.27
872747429	301.8575	-50.5693	15.127	14.955	14.965	14.854	14.831	0.6773	1.206	14.36
872752068	301.6538	-50.6110	16.995	16.721	16.600	16.692	16.628	0.6270	0.802	16.11
872879293	300.5544	-52.2926	17.406	17.147	17.169	17.209	17.304	0.5715	0.926	16.60
872910436	301.0276	-58.2702	16.614	16.617	16.728	16.775	16.897	0.4757	1.208	16.03
872914927	300.5669	-58.3127	16.846	16.775	16.766	16.781	16.739	0.5560	0.604	16.16

Table A.1: Representative list of RRab candidates found in the DES Y6Q data set described in Section 4. Column descriptions are as follows: DES Y6 ID: DES Y6A1 COADD_OBJECT_ID number. α: Right Ascension. δ: Declination. $\langle grizY \rangle$: Mean extinction-corrected magnitude. P: Best-fit period in days. A_g: Best-fit amplitude in DES g. μ: Best-fit distance modulus.